A Correlated 1-D Monatomic Condensed Matter System:

Experiment and Theory

Nader Zaki

Submitted in partial fulfillment of the

requirements for the degree of

Doctor of Philosophy

in the Graduate School of Arts and Sciences

COLUMBIA UNIVERSITY

2014

ABSTRACT

A Correlated 1-D Monatomic Condensed Matter System: Experiment and Theory

Nader Zaki

A one-dimensional quantum mechanical system is experimentally synthesized and investigated for physical phenomena that it may inherit due to quantum confinement and electron correlations. The experimentally realized system is a self-assembled array of monatomic cobalt wires that are grown under ultra-high vacuum conditions on a vicinal copper (111) substrate using a recipe developed specifically for this work. This work experimentally demonstrates that this 1-D system undergoes a charge density wave instability, which is a first for such a 1-D phenomenon on a metallic substrate. It is determined experimentally that this 1-D system undergoes an electronic phase transition at a temperature of about 85K, in which the higher temperature electronic phase is itinerant rather than localized. Using ab initio density functional theory, the cause of the measured charge density wave instability is assigned to ferromagnetic interactions along the chain. Specifically, it is deduced that the instability is driven by spin-minority spin-exchange interactions predominately in the cobalt dxz/dyz orbitals. Beyond, shedding light on electron correlations in a physically realized quantum mechanical 1-D system, this work demonstrates that this particular system is a new test-case example for advanced theoretical techniques in predicting the correct structural ground phase.

Table of Contents

1. Introduction 1

2. Experimental and Theoretical Techniques 7

2.1. Scanning Tunneling Microscopy 7

2.2. Density Functional Theory 12

2.3. Angle Resolved Photoelectron Emission Spectroscopy 19

2.4. Custom-built Knudsen Cell 21

2.5. Custom instrumentation for sample preparation 22

3. Self-Assembly Growth of Co Atomic Chains 24

3.1. Co Nucleation On Cu(111) Steps: Prior Experimental Work 26

3.2. Experiment 27

3.3. Results and Discussion 28

3.4. Conclusion 40

4. A 1-D Spin-Exchange Induced CDW Instability 41

4.1. Experiment 42

4.2. Results 43

4.3. Analysis 45

4.4. Analysis ramifications and applications 50

4.5. Conclusion 53

4.6. Methods 53

4.7. Supporting Discussion 55

5. A New Deficiency Case for Ab-Initio DFT Methods 70

5.1. Methods 71

5.2. Results and Analysis 74

5.3. Conclusions 80

5.4. Appendix : finite length monatomic wires 82

6. Surface-State Character Transition 83

6.1. Experiment 85

6.2. Observations 86

6.3. Analysis and Discussion 93

6.4. Conclusion 99

6.5. Appendix: Fourier analysis of photoemission intensity 99

7. References 104

Table of Figures

Figure 2.1 Custom-built Knudsen cell for physical vapor deposition of Cobalt. (a) the fully assembled Knudsen cell ready for mounting on a UHV chamber. (b) same as (a) but with external stainless-steel UHV tube removed. (c) top view of deposition source, revealing source aperture. (d) removal of tantalum shield reveals a hand-made ceramic crucible in contact with thermocouple leads. (e) top view of (d) revealing cobalt pellet inside the ceramic crucible. (f) same as (e) but with crucible and isolation posts removed. The ceramic discs (one is cracked), serve to electrically isolate the tantalum shields from the copper power feedthroughs (which deliver power to the ceramic enclosed tungsten filament) 21

Figure 2.2 Custom instrumentation with the ability to provide a controlled constant supply current of ≥6A, measurement of UHV gauges, and remote command of sputter controller, all by way of a serial interface to a computer. The power supply of the instrument is an old ATX computer power supply donated to the lab by the author..... 23

Figure 3.1 STM images of Cu(775) at RT, taken at V_{sample}=0.5V and I=150pA; the images are *dz/dx* (i.e. derivative). (a) 100×87nm^2 scan showing relative uniformity of step spacing. (b) Atomic-resolution scan of steps showing "frizz". Inset, topographical close-up of step terrace clearly revealing the (111) surface..... 28

Figure 3.2 STM derivative images of Cu(775) at RT after deposition of Co. Blue-colored circles denote Co atoms and gold-colored circles denote Cu atoms. The black arrows in the topographical profiles correspond to positions indicated by white arrows in the images. (a) Scan showing one-atom-wide Co wires; frizz is seen on a clean step edge at

the left of the image. The inset is a topographical profile along the direction of the corresponding white line in the image. Coverage is 0.09ML. (b) Scan showing two-atom-wide Co wires, as well as one-atom-wide wires and clean-steps. A plateau, denoted by arrows, is seen for the two-atom wide wire scan; in this image, the plateau is not seen for one-atom-wide wires presumably due to finite tip radius and the narrowness of the wires; however, the lack of frizz is a strong indication of Co at the step edge. Coverage is 0.12ML. (c) Profile for white line in (b). The gray dashed line serves merely as a step guide for the eye and does not denote the exact position of the steps. (d) Scan showing terrace-embedded Co. Coverage is 0.12ML. (e) Embedded Co appears as depressions, as indicated by the arrow, in the step terrace. 30

Figure 3.3 Distribution of 1-atom-wide Co wire lengths. The smooth grey curves denote a fit based on a one-dimensional lattice gas model; see discussion in text. At a coverage of 0.09ML (circles), the average wire length is a ~27 atoms. As the coverage is increased to 0.12ML (squares), the average wire length increases to ~40 atoms, indicating that wire length increases with coverage. This result is in accord with a growth mechanism, in which the Co atoms move facilely along the step edge until encountering a wire end, to which the Co atom attaches. Note that in comparison to the typically reported widths of nanometer-scale islands at step edges (5nm or ~20 atoms), the 1- and 2-atom (not shown above) wires have grown to much longer length scales. 32

Figure 3.4 Different Co growth phases develop with increasing coverage. Top panel (i): A derivative image shows that at 0.12ML, four different "phases" exist: (a) "frizz", (b) one atom-wide wire, (c) two atom-wide wire, (d) terrace embedded Co. See details in Fig. 2(b) for the single-atom-wide wires. Bottom panel (ii): Wire-length-to-step-length ratio

versus coverage. “Ideal” refers to calculated ratio for growth of only 1-atom wide wires on a perfect seven-atom-row stepped surface. The falloff in the 1-atom wire ratio above 0.09 ML is due to 2-atom-wide wire growth, terrace nucleation, and terrace-width variations; without these components, the 1-atom wire step ratio would follow that of ideal wire growth. 35

Figure 3.5 Self-assembly at 0.09ML Co coverage. This STM image (d2z/dx2, i.e. second-derivative), acquired at RT, clearly shows the presence of self-assembled 1-atom-wide Co wires along with bare Cu(111) steps. The 1-atom-wide wires appear as straight sharp double lines at the step edge. Frizz, on the other hand, causes the bare Cu(111) step edge to appear irregular. The positions of the self-assembled wires are relatively random, indicating freedom from any substrate-mediated reconstruction or discommensuration. Note: the appearance of broken/shifted wires is merely due to tip-change. 37

Figure 4.1 Self-Assembled Co atomic chain system. (a) Illustration of dimerized Co atomic chains on vicinal (8.5º miscut) Cu(111). (b)-(d) Illustration of high-spin ferromagnetic, high-spin anti-ferromagnetic, and zero-spin electron configurations. Coupling is strongest for the high spin ferromagnetic phase, weaker for the zero-spin phase, and blocked for the anti-ferromagnetic phase. (e) Perspective view of a STM topography of two self-assembled Co wires at adjacent Cu step edges. The vertical scale has been magnified to accentuate the appearance of the Co wires. The Co atoms constituting these wires have undergone a 1-D structural distortion, leading to the appearance of a single peak near the Cu step edge. However, the underlying Co atoms constituting each single peak are resolved farther away from the Cu step edge due to the decreased

contribution of the Cu local density of states to the tunneling current. Constant current tunneling parameters: V_{bias} = +0.742V at 9.4nA. 44

Figure 4.2 DFT energy-phase diagrams for atomic wires. Points denote actual calculated energies while smooth lines in between are 3rd-order interpolations. Total energies were calculated for a two-atom unit cell using DFT and the GGA functional (Figure 4.8,Figure 4.9). The lack of smoothness in some regions is due to varying degrees of orbital polarization (see supporting discussion). (a) Energy-phase diagram for Co atomic wire. The energies of the Co wires have been offset with respect to the *ferromagnetic* non-distorted case (NNBL=1.0); the horizontal dashed grey line denotes the reference. The nearest neighbor bond length is given as a ratio of the bulk Cu atom spacing (2.5561Å). (b) Energy of Co_2 and Cu_2 isolated wires measured relative to the energy of the undimerized wire and plotted against degree of dimerization (parametrized as ratio of short bond length to average bond length). Different curves indicate different strains (i.e. different unit cell lengths) relative to the unit cell length that minimizes the DFT energy of the wire. The energy of the Co wire has been computed for a ferromagnetic state; the Cu wire was computed for a non-spin polarized state (spin-polarized calculations converged to a zero-spin state). The left hand dashed grey line denotes the optimal bond length of the dimer (measured in units of one half of the mean unit cell length of the strained wires). The right hand grey line indicates the interatomic distance for the optimal non-distorted wire. The red vertical line segments mark the optimal nearest-neighbor bond length for each respective strained wire system. 47

Figure 4.3 Fitting to a cluster expansion model. (a) Cluster expansion model illustration of the Co 2-atom unit cell. J_1 denotes the nearest-neighbor or *intra*-pair

interaction while J_2 denotes the *inter*-pair interaction. The unit cell is delineated by the dashed rectangle outline. (b) Cluster expansion model parameter fits for the Co atom wire for different amounts of distortion. E_0 is the non-magnetic energy contribution. The vertical dashed line denotes the optimal Co wire distortion. Note that J_2 is quite negligible at the optimal distortion length. Energies were computed using spin polarized GGA (Figure 4.11). 51

Figure 4.4 Co atomic chain self-assembly. STM image of self-assembled atomic Co chains (visible as linear arrays of approximately spherical dots) on the 14Å average-width terraces of Cu(775) measured at T = 5K. A derivative ($\partial z/\partial y$) filter was applied to accentuate the appearance of the Co decorated step edges. The Co coverage is ~0.14ML. At 5K, the single-atom wide Co chains along the step edge are found to undergo a dimerization distortion along the chain direction. Hence, the sphere like objects are not single Co atoms but rather pairs of Co atoms with separation 22% smaller than the underlying Cu atom spacing. The different appearance of some of the Co atom pairs is due to adsorption of impurity molecules, presumed to be CO (see supporting discussion, Figure 4.6). Constant current tunneling parameters: V_{bias} = +2.08V at 9.4nA. 59

Figure 4.5 Delineation of Co atoms by subtraction of Cu step. (a) STM image of a Co dimerized chain self-assembled at a Cu step edge. The location of the Co atoms can be inferred from the grid lines superimposed on the topography. (b) The same topography as in (a) but with the ×2 distortion boundary denoted by white lines. Within each boundary are a pair of Co atoms; two of these pairs have been marked as 1 and 2. The profiles defined by the white lines approximate the profile of a clean Cu step edge. One of these lines, as indicated by the red circle, has been used for the subsequent subtraction step, which

produces the topography shown in (c). (c) Subtracting the aforementioned profile line produces a relatively flat plane with protrusions belonging to the Co-*pair* LDOS. This derived topography can then be vertically scaled to more clearly visualize the Co dimerized chain (d)..... 60

Figure 4.6 Interaction of an impurity with a self-assembled Co dimerized chain. Although the identity of the impurity is unknown, it is guessed to be a CO molecule. The topography images shown here were derived by subtracting the Cu step, as per Figure 4.5. (a) An STM topography of a Co dimerized chain, of which 5 Co pairs are visible. In addition, an impurity (labeled M), located in the neighborhood of Co pair 1 and Co pair 2, is also present. The electronic effect of the impurity is to increase the LDOS around Co pairs 1 and 2, as evidenced by the increase in their apparent height. (b) At a higher bias of -0.25V, the tip is able to dislodge the impurity. This is observed in the changing topography, in which scan lines run perpendicular to the chain, from right to left (i.e. from Co-pair 5 to Co-pair 1). After the impurity is dislodged, Co-pair 1 appears with the same contrast as Co pairs 4 and 5. (c) The same chain, after dislodging of the impurity, showing the recovery of the uniform LDOS dimerization for each Co pair. The ability to easily dislodge the impurity using a relatively average tip bias indicates a weakly bound entity to both the Co chain as well as the underlying Cu substrate; in conjunction with the observation of a small apparent volume, these measurements support the identity presupposition of a small molecule such as CO. This observation also shows the relative inactivity (i.e. lack of strong hybridization) of the Co chain with the impurity. 61

Figure 4.7 Measurement and analysis of the Co bond length structural distortion at 5K. Plots are based on STM measurement shown in Figure 4.1e. (a) Height profiles along

the Co wire direction, obtained at a series of equally spaced points away from the step edge. Bars are guides to the eye indicating spacing of Co atoms in a dimer. (b) The peak-to-peak (P-P) spacing varies with vertical distance from the top of the Co wire, as shown for the two Co wires by different color curves. The vertical distance from the top of the wire was normalized to the apparent wire height, which, for this particular example, was approximately equal to the Cu step height of 2.09Å. (c) A profile cut perpendicular to the step edge reveals a smooth outline due to the finite radius of the tip and the relatively narrow terrace width. The blue shaded region is a guide to the eye for the approximate position of the Co wire, while the red shaded rectangle corresponds to the region of constant P-P length, denoted in (b) by a bar. 62

Figure 4.8 Co wire distortion phase energies using different DFT functional (*without orbital polarization*)**.** The top row shows the Co wire energy for different nearest-neighbor distortions; the right vertical axis (2.5561Å) is the case of zero distortion. The energies are referenced to the undistorted ferromagnetic phase. The unit cell size is equal to 2 × Cu atom spacing (2 × 2.5561Å = 5.1122Å). E_0 is the average of the ferromagnetic and anti-ferromagnetic phase energies. The points are the actual computed energies, while the smooth lines are 3rd-order interpolations. The bottom row shows the change in energy for different combinations of E_F, E_{AF}, and E_0; each combination is referenced to its respective value of the undistorted wire case. The optimal nearest neighbor bond length (d_{short}), denoted by the vertical dashed line, is 1.98Å using LDA, and 2.03Å using GGA or PBE. 63

Figure 4.9 LDA (a) and non-orbital polarized GGA (b) DFT functional version of Figure 4.2b**.** 64

Figure 4.10 Electronic structure of isolated Co wires constrained to bulk Cu atom spacing (2.5561Å × 2 unit cell). Plots (a) and (b) correspond to the non-distorted wire while (c) and (d) correspond to the optimally dimerized case. The z-axis is parallel to the wire. (a), (c) Band energy diagram for majority and minority spin. The dxz, dyz orbital derived bands are degenerate, as expected by symmetry. Also, by symmetry, the $dz2$ and s orbital derived bands are hybridized; the amount of hybridization in each band, however, is not always uniform across a band or across spin populations. The dxy, $dx2 - y2$ orbitals are lifted out of degeneracy due to orbital polarization. Note that overall, the dimerized Co wire is not an insulator; an $s/dz2$ orbital derived band crosses the Fermi level for both majority and minority spin. (b), (d) The corresponding density of states. Computed using spin polarized GGA. 65

Figure 4.11 Cluster fit expansion comparison and errors. To quantize how well the cluster expansion fits the DFT calculations, we plot the error between DFT and the cluster expansion for both nearest-neighbor (J_1 and J_2 only) and next-nearest-neighbor (J_1, J_2 and J_3). (a) Illustration of next-nearest-neighbor model. (b) Plot of cluster fit parameters with respect to the short bond length. (c) Energy comparison plot between DFT and nearest-neighbor cluster expansion. The unit cell used for the comparison consisted of 4 atoms, and 4 distinctly different spin configurations were utilized. The error is plotted underneath, with symbol colors corresponding to the respective spin configurations. Note that the error is relatively smaller at the optimal short bond length. (d) Same as (c) but for a next-nearest-neighbor expansion. Energies were computed using spin polarized GGA. 66

Figure 4.12 STM topography of Co wires at 91K. The technique of substrate subtraction, as described in Figure 4.5, was employed in producing these images. This

higher temperature phase shows tip-bias dependency, in contrast with the dimerization instability phase present at lower temperatures. (a) and (b) are front and top views, respectively. Note that the chain modulation is not only parallel to the chain, but can appear perpendicular to it; for instance, at ±500mV, the chain appears to have a zig-zag topography. The discontinuity in the topography at −500mV is due to a tip change..... 67

Figure 4.13 Line profiles along Co chain of Figure 4.12**.** Profile line position was taken at peak maximums; unlike the dimerization instability phase, the individual Co atoms do not coalesce together, but rather are resolved at their local maximum. The profiles for occupied and unoccupied states appear relatively similar at a fixed magnitude of tip bias (e.g. ± 100mV, ± 300mV); this is true for a tip bias magnitude of up to at least 500mV. On the other hand, a comparison of line profiles between different tip biases reveals variation in phase shift and amplitude. The numbered peaks and dashed vertical lines serve as a guide for the eye. The chain terminates on the left (0 Å); a Friedel-like oscillation is observed due to the finite length of the chain, and has a wavelength of ~25Å..... 68

Figure 4.14 Co-existence of two phases of a Co chain at $T \sim T_{Dimerization}$ = 81K**.** STM topography was measured with tip bias of +238mV. Three chains are delineated. A chain with a dimerization instability (labeled "Co_2 phase") exhibits a clear 2× distortion as well as coalescing of the LDOS peaks. A chain without a dimerization instability (labeled "non-Co_2 phase") does not show a 2× distortion; instead, the constituent individual Co atoms are clearly delineable and the nearest neighbor bond length is closer to that of the underlying Cu substrate; the topography is similar to that at $T > T_{Dimerization}$ (see Figure 4.12). The chain labeled "mixed phase" exhibits regions with varying similarity to the dimerization instability phase. In comparison to measurements at this temperature, STM measurements

taken at $T>T_{Dimerization}$ exhibit a uniform phase topography. The inset is a rendering of the topography enclosed in the dashed rectangle after applying the substrate subtraction technique of Figure 4.5. 69

Figure 5.1 Different substrate geometries on which slab calculations for a Co 1-D wire system have been calculated. Cu atoms are colored white while Co atoms are blue. For the Cu(111), Cu(111)-wedged, and the Cu bulk cases, the Co wires make up every 6^{th} row, which gives a wire-to-wire separation of ~13.3Å. For the vicinal substrate case, Cu(332), the step terrace width is ~6 atom rows, and the wire-to-wire distance is ~12.0Å. In this work, these slab geometries are denoted as cases (1)-(4), respectively..... 72

Figure 5.2 An illustration of the cluster expansion model utilized in this work. J_1/J_2 are the nearest neighbor magnetic pair interactions, while J_3 is the next-nearest neighbor magnetic pair interaction. The dashed rectangle denotes one unit cell. 73

Figure 5.3 Energy phase diagram for a Co wire in different slab configurations. The horizontal axis is the ratio of the short bond length of the Co wire with respect to the non-distorted bond length (2.56Å). The relaxed Cu(332) curve corresponds to the case where the Co wire is positioned at the optimally relaxed position with respect to the Cu(332) substrate. The dashed vertical line denotes the experimentally measured short bond length for a Co wire on vicinal Cu(111). 76

Figure 5.4 Cluster expansion parameter fits for different Co wire slab configurations. The horizontal axis is the ratio of the short bond length of the Co wire with respect to the non-distorted bond length (2.56Å). The bottom row of plots correspond to the slope of the magnetic and non-magnetic energy contributions shown in the above row

plots as the blue and red curves, respectively. The dashed vertical line denotes the experimentally measured short bond length for a Co wire on vicinal Cu(111). 77

Figure 5.5 An expanded plot of the cluster expansion parameter fits for different Co wire slab configurations, establishing the trend with increasing coordination. The horizontal axis is the ratio of the short bond length of the Co wire with respect to the non-distorted bond length (2.56Å). The solid colored lines correspond to the total magnetic energy contribution; the dashed colored lines denote the non-magnetic energy contribution. 79

Figure 5.6 Orbital projected Kohn-Sham eigenvalue band diagram for a Co wire in vacuum. The Co atom spacing is $a = 2.56$Å. The top row plot corresponds to the spin polarized GGA DFT calculation while the bottom row corresponds to the DFT+U version with $U = 4eV$ and $J = 1eV$. 81

Figure 6.1. Schematic diagram of Cu(775). The 7-row terrace is terminated by (111)-like edges; the steps are denoted as type-B steps, as is the case for all (n,n,n-2) surfaces; in contrast, (n,n,n+2) vicinal cuts are characterized by (100)-like edges and are denoted as type-A stepped surfaces. Due to the odd number of rows per step terrace, the unit cell is not rectangular, as in the case for even number of rows, but a parallelogram. The corresponding surface Brillouin zone is shown in the top right-hand corner, and its boundary in the direction normal to the step-edge is marked with a dotted line along with its wave-vector magnitude. 83

Figure 6.2. (50nm x 50nm) RT STM image of Cu(775). The inset is a step-width distribution of Cu(775). 85

Figure 6.3 (a) RT ARPES of clean Cu(775) in direction perpendicular to steps (i.e. -kx). (b) 2nd derivative of ARPES data in (a). By varying the photon energy, the step-modulated surface state and its umklapp can be observed. As expected, the surface-state band minimum appears at the zone boundaries, as indicated by the white dashed vertical lines. Note that the faint state, indicated by yellow dots in (b), shifts with photon energy. This state is aligned with the step terrace normal, instead of the macroscopic surface normal, and hence is a terrace-modulated state. Apparently, for Cu(775), there are two competing modulations, step vs. terrace, as evidenced by the above ARPES measurements. (c) Example of a (smoothed) momentum distribution curve (MDC) taken at -0.1eV using ARPES data from 45eV photon energy; the marked peaks correspond to the step-modulated surface state, its Umklapp and the terrace-modulated state. 88

Figure 6.4. (a) Schematic diagram of possible state transitions during angle-resolved photoemission from ideal Cu(775), i.e. perfect step-array of 14.0Å. All energies are referenced to the Fermi level. The initial state band, consisting of the surface state and its Umklapp, i.e. the step-modulated superlattice surface state, is denoted in white, centered at 0.22Å-1 and 0.66Å-1; their dispersion is shown clearly in (c). The final state band, a free-electron band approximation, is denoted in gray, and has a paraboloid shape; a contour plot of this band is shown in (b). Sample transitions for several photon energies are shown in (a) and (b) and some are explicitly marked by arrows in (a). The initial states are marked by thick gray lines on the initial state band in (a) and the final states are marked by thick black lines on the final state band in (a) and (b). Due to the low binding energy of the initial state, it and its corresponding final state appear to follow the lines of constant energy, as shown in (a) and (b). 94

Figure 6.5. Cu Bulk projection of 1st BZ for flat and vicinal Cu(111) surfaces. The *sp* surface state gap is at k||=0 for Cu(111) as expected. Note that the projection is not symmetrical with respect to k||; though the surface BZ of Cu(111) is 6-fold rotationally symmetric, the bulk BZ possesses only 3-fold rotational symmetry along the[111] direction which is reflected in the projection. For these vicinal surfaces, the sp gap shifts in the direction of $\overline{M}'$ (i.e. toward bulk symmetry point X), but does not close or lose noticeable volume with vicinal angle. The vertical red line denotes k||=0 which corresponds to the macroscopic surface normal. The blue vertical lines correspond to ±π/L and ±3π/L. Note that the sp gap minimum is aligned with the first surface BZ boundary,-π/L, as is the case with the step-modulated surface state. Also notice that there is no projected gap for the Umklapp surface state, centered at -3π/L. Furthermore, there is no projected gap for positive values of k||, i.e. k|| ≥ 0..... 97

Figure 6.6. Discrete Fourier transform (DFT) of the forms of the wavefunction for different Cu surfaces. (a) DFT for Cu(111) for waveform at $\overline{\Gamma}$. The form of the waveform is shown in the inset; the change in colors from red to blue symbolize the change from positive to negative. The ellipses mark the positions of strong FT intensities or resonances along the $k_{||}=0$. (b)DFT for Cu(775) for waveform at $(\kappa_x = \pi/L, \kappa_y = 0)$ as well as $(\kappa_x = 3\pi/L, \kappa_y = 0)$. The form of the waveform is shown in the inset; the change in colors from red to blue symbolize the change from positive to negative. The ellipses mark the positions of strong FT intensities along $k_{||} = \pi/L$, $3\pi/L$, and $5\pi/L$. In both (a) and (b), a gray transparent strip is used to enhance the intensities of interest and also denotes the <111> direction. 101

Dedicated to Jesus Christ

and

my parents

1. Introduction

The general goal of this research is to synthesize one-dimensional quantum systems and to study physical phenomena that they may inherit due to the imposed quantum confinement. From a theoretical standpoint, one-dimensional quantum systems are one of the simplest systems to investigate if one excludes many-body effects, i.e. electron-electron interactions. On the other hand, upon introducing electron-electron interactions, a one-dimensional system is non-trivial to solve. In fact, Fermi liquid theory, the theory that allows one to assume free-electron like behavior in a variety of 3-D systems, breaks down for 1-D systems precisely due to the reduction in dimensionality [1]. Instead, one theory that is usually invoked in the study of these systems is Luttinger theory, from which such exotic phenomena as spin and charge separation are predicted. Hence, studying one-dimensional systems in the experimental lab is of general interest in gaining a better understanding of which physical behavior is actually realized in practice and what modifications, if any, need to be made to current theoretical understanding of this subject.

This work is not the first experimental attempt to realize and study a monatomic 1-D system. Some of the earlier reporting of pseudo-atomic 1-D systems with interesting NMR, optical, and photoemission results include the organic charge transfer complex (salt) TTF-TCNQ and the inorganic molybdenum blue bronze $K_{0.3}MoO_3$ [2]. These systems, respectively, are actually long chain complex ligand crystals for the case of TTF-TCNQ, and atomic delineations along particular symmetry directions of anisotropic crystals, as in the case of $K_{0.3}MoO_3$. More recent attempts at measuring signatures of exotic 1-D physics, using transport techniques, have been made on systems approaching the monatomic wire limit;

these include carbon nanotubes and nanometer thin wires [3]. While these studies have observed behavior that appears to agree with some the predictions of Luttinger liquid theory, skeptics point out that similar results have been measured in more bulk-like materials, and that the observed behavior may be due to disorder effects in the resistive leads [3]. The skepticism expressed at these results is, in part, perhaps justified, since a slightly earlier result on a substrate supported monatomic system using angle resolved photoemission spectroscopy (ARPES), had claimed the first direct observation of a Luttinger liquid [4]; however, this claim garnered some controversy and was ultimately disproved a few years later, as the system was instead shown to exhibit a metal-insulator transition [5], which rules out the presence of a Luttinger liquid [6].

As was later discovered, the above mentioned substrate supported monatomic system, consisting of self-assembled gold chains grown on a vicinal silicon substrate, is actually part of a family of such systems that exhibit what has been referred to in the field as a charge density wave (CDW) instability. Generally, a CDW instability refers to a structural or electronic instability that is often "reminiscent of a Peierls instability" [6]. For monatomic wire systems, the ones that up till now have exhibited a CDW instability have been limited to relatively heavy elements such as Au and In, and only on semiconducting substrates such as Si and Ge. While reports of these systems have assigned the cause of the CDW instability to several different physical mechanisms, such as electron-phonon coupling or Fermi surface nesting, a consensus is yet to be reached. Besides the limited number of atomic chain systems with a CDW instability, there are important complications that plague the analysis of some of these particular systems. The accurate determination of the crystallographic structure of an impurity decorated semiconducting surface such as Si

has often been one of trial and error, relying heavily on theoretical calculations, and sometimes leading to more than one viable structure. This problem is due to the inability to directly measure the surface crystal structure with atomic element specificity. For example, low energy electron diffraction (LEED), a surface sensitive probe, can provide some clues to the sometimes reconstructed surface structure, but does not provide an element label for each diffraction spot. Likewise, investigations of these systems using scanning tunneling microscopy (STM), a workhorse for atomic resolution surface characterization, is hindered by the fact that the system topography is voltage bias dependent, rendering the identity of the topographic features ambiguous. Hence, there is a need to experimentally realize other monatomic wire systems that do not suffer from these complications, and yet, lend themselves to the study of CDW instabilities.

Another motivation, beyond merely realizing exotic 1-D phenomena, lies in the fact that many outstanding problems in condensed matter physics, such as high temperature superconductivity and strongly correlated oxide material properties, are complicated in part due to the possible presence of structural changes and strain commensurate with electronic phase transitions. Experimental work in this field has predominately focused on quasi-2-D and 3D materials, such as the dichalcogenides and Mott insulator materials. Elucidating the physics behind the electronic structure and properties of these materials has been difficult, however. In this area of our work, we have taken up the study of an experimentally realized 1-D system, with the goal of not only understanding the physics of 1-D systems, including the uncovering of exotic electronic phases unique to 1-D, but also as a means to contribute to the understanding of higher dimensional systems. This has been both an experimental and theoretical endeavor, utilizing both the experimental tools of

room-temperature and low-temperature scanning tunneling microscopy (STM) and the theoretical methods of density functional theory (DFT) and its higher order derivatives, such as DFT+U.

Our primary experimentally realized system has been the self-assembled array of monatomic Co wires that are grown in-situ under UHV conditions on a vicinal Cu(111) substrate using a recipe that we have developed. We have experimentally demonstrated that this 1-D system undergoes a CDW instability, which is a first for such a 1-D phenomenon on a metallic substrate. We have determined the phase transition temperature below which the Co wires exhibit this CDW instability to be ~85K. Above this temperature, we observe an electronic phase transition in which the electronic structure of the Co wires become itinerant, as evidenced by the emergence of a Friedel oscillation along the wires. We have also experimentally shown that the monatomic Co wires are relatively robust to at least one type of physisorbed impurity; this was demonstrated by STM atom-tip manipulation in which the impurity residing next to the Co wire was physically removed, recovering the local density of states of a pristine Co wire in the CDW instability phase.

On the theoretical front, we have assigned the measured CDW instability to ferromagnetic interactions along the chain. Starting with a simple periodic 1-D Co wire system-in-vacuum model and DFT calculations, we found that the CDW instability is driven by spin-minority spin-exchange interactions in the dxz/dyz orbitals. We concluded that the CDW instability could only occur for ferromagnetic coupling between Co dimers along the wire, since antiferromagnetic coupling would be obstructed by the Pauli exclusion principle. In addition, we also determined that the Cu substrate provides strain that

accentuates the CDW instability. Using these conclusions, we then deduced further structural and magnetic properties of this CDW instability using a cluster expansion model and additional DFT calculations.

The simple model of a Co wire-in-vacuum mentioned above served well in elucidating the physics behind the CDW instability. However, our experiment consisted of the Co wire being supported on a Cu substrate. Naturally, we were interested in determining if any additional insights could be gleaned from a calculation that modeled our experiment conditions more closely. The ab-initio method, density functional theory (DFT), has been immensely successful in its ability to predict physical properties of condensed matter systems. It is at the forefront of ab-initio methods in its quantitative accuracy when compared with experiment, and is generally qualitatively correct for most systems. Here, however, we have found that DFT can fail qualitatively to correctly predict the CDW instability phase for this monatomic Co wire system that resides on a stepped Cu(111) substrate. We have attributed this failure to DFT's over-prediction of hybridization of the Co wire with the underlying Cu substrate. We demonstrated that this over-hybridization leads to weakening of the magnetic coupling along the wire, which is responsible for the CDW instability, while increasing the stiffness of the wire due to strengthening of the non-magnetic elastic term. Additionally, we have shown that accounting for local interactions via DFT+U also fails at predicting the correct structural phase. Hence, we offer that the arrangement of a Co wire on a vicinal Cu(111) substrate is a new "test bed" for more sophisticated theoretical methods that could recover its highly correlated electronic structure, and hence, its CDW instability ground state phase.

While this work has predominately focused on the synthesis, characterization, theoretical understanding of electronically correlated atomic chains, the fact that these chains are fabricated on a vicinal supporting substrate inherently raises the question of the substrate's electronic structure. In particular, the narrow terrace widths (typically <20Å) of the Cu substrate used in this work gives rise to an interesting electronic structure transition, in which the surface electrons are not localized to the step terrace but are rather itinerant across the steps. In this work, we detail the results of angle resolved photoemission spectroscopy mapping of the electronic structure of a vicinal Cu substrate whose vicinal cut angle renders it close to this electronic structure transition.

2. Experimental and Theoretical Techniques

The experimental realization and study of quantum 1-D systems is a challenging endeavor due in part to the inherit atom-sized nature of such systems. Beginning from a pure element, such as Cobalt, which is readily available in bulk polycrystalline form, one must first devise a recipe to synthesize one or more monatomic wide chains that are thermodynamically stable over a reasonable region of temperature. Achieving a thermodynamically stable 1-D system is critical in that it allows for generally slow but precise techniques such as scanning probe microscopy and angle resolved photoemission spectroscopy to be utilized. Measurement of 1-D systems by these tools can yield rich information about their structural and electronic phases; understanding why a particular phase is favored over another, however, usually requires a detailed theoretical approach. The ability to accurately calculate the ground state energy of a system is the most basic and yet most important goal of any general ab-initio condensed matter theoretical technique, of which the most widely used ab-intio technique in the field is that of density functional theory. In this chapter a brief overview of the two most utilized techniques in this body of work, scanning tunneling microscopy (STM) and density functional theory (DFT), is provided. In addition, brief sections on angle resolved photoelectron emission spectroscopy (ARPES) and instrumentation are included.

2.1. Scanning Tunneling Microscopy

The invention of scanning tunneling microscopy in 1981 [7] marked the start of a field of microscopy that can routinely image surface topographies, and often with atomic

resolution. While it was not the first invention to image atoms, for that claim belongs to the field ion microscope (1955) [8], it was the first tool to allow relatively flat surfaces of not only metals but semiconducting substrates to be atomically resolved, extending dramatically the range of systems that can be studied beyond that of a metal tip, as required by field ion microscopy. Furthermore, it's flexibility goes beyond pure crystalline substrates, in that it allows for resolving of a large gamut of inhomogeneities on the substrate, whether unintentionally present defects such as missing sites and steps, to intentionally deposited impurities such as adsorbed molecules.

While the physical principles entailed in scanning tunneling microscopy are sophisticated, the operating mechanism behind obtaining a topographic map of the surface in question is quite simple. An STM instrument typically consists of a sharp metal probe (the "tip") in near proximity of the surface under investigation, and by which tunneling current in the pico- to –nanaoampere range flows between it and the surface. The vertical distance between the tip and the surface is controlled by negative feedback, in which the quantity to be maintained constant is the tunneling current. As the tip-to-surface distances changes, so does the tunneling current, which ideally induces a negatively proportional change in the vertical position of the tip, bringing the tip-surface distance back to its original value. The tip is located on a piezoelectric material which is the means for its vertical as well as lateral movement. Along with the electronics that close the negative feedback circuit, which includes a high gain current amplifier and a proportional-integrator control circuit, and a piezo driver circuit which is simply a high voltage signal amplifier, this comprises the bare minimum requirements for performing a simple scanning tunneling microscopy measurement. A practical STM instrument would include some

additional items, such as vibration isolation mechanisms such as a spring suspended magnetically damped stage, a computer controlled tip and acquisition interface, and a means for controlling the temperature of the sample (and ideally the tip as well!).

Two basic physical principles are at the heart of scanning tunneling microscopy: the quantum mechanical phenomenon of tunneling and the atomic structure phenomenon of piezoelectric displacement. Separately, each of these phenomenon had been well known for decades prior to the invention of the STM, and for at least the case of quantum tunneling, had been already been put to use in spectroscopic transport research in condensed matter physics. It is their synergy, however, that has made scanning tunneling microscopes a workhorse of surface science. The physical theory behind each of these phenomena will now be discussed, with a disproportionate emphasis placed on quantum tunneling.

The phenomenon of quantum particle tunneling was realized in the 1920's by experiments on field emission from metals [7], and later explained as a direct consequence of the newly postulated quantum mechanics. One of the main postulates of quantum mechanics states that quantum particles obey a differential equation, the Schrödinger wave equation. A ramification of this is that solutions of this equation will necessarily obey boundary conditions, specifically continuity up to at least 1st order. It is precisely this requirement of boundary conditions that leads to the non-classical result that particles with energies less than that of a potential barrier (an energy potential obstruction) can never the less penetrate into this classically forbidden region. While a quantum particle can non-classically penetrate into a potential barrier, the probability of existing in the potential barrier region decreases exponentially with distance away from the barrier boundary. Hence, a potential barrier of finite length that separates two lower energy regions would

need to be relatively thin in order for a quantum particle to have a significant chance of existing on either side of the barrier within a reasonable amount of time. When this length requirement is met, the system is defined to be in a tunneling regime.

The relevant experimental realization of the above model is two metals separated by a vacuum gap. The two metals hold bound electrons, that is, electrons that lie lower in energy compared to free electrons that would exist in vacuum. The classically forbidden region is the vacuum between the two metals, in which electron transport would classically not be expected. The energy barrier posed by the vacuum relative to the bound electron states in the metal is defined as the work function: it is the minimum energy required to excite the highest occupied bound electronic state in the metal to the lowest free electron state. The work function barrier associated with the metal-vacuum interface is not spatially sharp, as in the above model case, but rather follows a 1/r proportionality relationship, where r is the distance from the metal surface. If the two metals are brought sufficiently close, the potential barrier in the vacuum is decreased due to the proximity of the metal ion sites, or put another way, the potential barrier no longer reaches its full height due to the slow 1/r potential energy relationship and the small relative gap between the two metals. The decrease in the potential barrier, along with the decreases in the vacuum region length, allows for the onset of the tunneling regime, which for practical purposes refers to currents $\geq$ 1pA.

Up till this point, we have discussed a model and a practical realization of this model that is in equilibrium, i.e. there is no net charge transport or net flow of electrons across the vacuum region. Applying a voltage bias across the two metals, however, brings the system out of equilibrium, by oppositely shifting the relative energy positions of the electronic

states of the two metals, which then drives a net tunneling current across the energy barrier. The direction of electron flow is from the higher energy biased metal to the lower energy biased metal. The magnitude of the tunneling current is proportional to the applied bias and the integrated density of states of the two metals. This is described in the following relationship, derived elsewhere [7]:

$$I(r) \propto \int_0^{eU} n_t(\pm eU \pm \mathcal{E}) n_s(\mathcal{E}, r) d\mathcal{E}$$

where n_t and n_s are the density of states of the tip and surface, respectively, e is the electron charge, and U is the applied tip bias. Hence, in the case of scanning tunneling microscopy, the topography that is measured at constant tip bias and constant current (and constant tip shape!) is approximately proportional to the integrated local density of states of the surface.

The angstrom scanning capability of a tunneling microscope (and almost all atomic resolution scanning probes) is typically provided by means of a ferroelectric crystal, such as $PbZrO_3$ [9]. A ferroelectric crystal is defined as a crystal with a structural phase transition that is commensurate with the onset of a permanent dielectric polarization [10]. Applying an electric field opposite to the direction of the dielectric polarization induces strain on the crystal (this is referred to as the piezoelectric effect), which gives rise to a spatial displacement of objects attached to the crystal, which in the current context is the tunneling probe or tip. By using an assembly of three ferroelectric crystals, in which their respective directions of dielectric polarization are perpendicular to each other, allows for translational displacement of the STM tip in 3-d space. Typical modern day STM instruments, however, make use of a tube-shaped piezoelectric ceramic, along with

compensating electronics and/or compensating electrode configurations to provide orthogonal x,y,z positioning [9].

It should be noted that the above description of piezoelectric materials is quite simplified. Details omitted from this discussion include the fact that piezoelectric scanners do not typically use single-crystal ferroelectrics but rather a ceramic isotropic bi-composition of ferroelectrics ($PbZrO_3/PbTiO_3$), that are poled for an extended period of time, subsequent to being shaped to the desired form, to induce an anisotropic electric polarization [9]. To avoid confusion, it should also be noted that that though all ferroelectric crystals are piezoelectric [10], not all materials exhibiting a piezoelectric effect are ferroelectric; an example of this is quartz (single crystal SiO_2). One reason that quartz is not utilized in piezoelectric scanners is its relatively low piezo constant of -2.25pm/V which is two orders of magnitude lower than that of ferroelectric lead zirconate titanate ceramics, commonly known as PZTs [9].

2.2. Density Functional Theory

Prior to the derivation of density functional theory formalism by Hohenberg, Kohn and Sham in 1964-1965 [11, 12], accurate ground state energy calculations of condensed matter systems required computing for the full quantum mechanics multi-electron antisymmetric wavefunction. This meant working with a computationally demanding Slater determinant by way of the Hartree-Fock method. Hohenberg, Kohn and Sham recognized that arriving to the ground state energy did not necessarily require determination of the full wavefunction, Ψ_{Slater}, of the system, but simply the charge density of the system, i.e.

$$\rho(r) = \int\int \cdots \int \Psi_{\text{Slater}}(r_1, r_2, \dots, r_i = r, \dots, r_n)\ \Psi_{\text{Slater}}(r_1, r_2, \dots, r_i = r, \dots, r_n)^* dr_1 dr_2, \dots, dr_{i-1} dr_{i+1}, \dots, dr_n$$

Without going through a full derivation, this important simplification can been seen by starting out with the nonrelativistic wave equation for a quantum system, i.e. the Schrödinger equation:

$$H\Psi = \left(\frac{1}{2}\sum_{i=1}^{N} \nabla_i^2 \Psi\right) + v(r)\Psi(r_1, r_2, \dots, r_i = r, \dots, r_n)$$

$$+ \frac{1}{2}\int\int \cdots \int \frac{1}{|r - r'|}\Psi(r_1', r_2', \dots, r_i'$$

$$= r', \dots, r_n')\ \Psi(r_1', r_2', \dots, r_i' = r', \dots, r_n')^* \Psi(r_1, r_2, \dots, r_i = r, \dots, r_n) dr_1' dr_2', \dots, dr_n'$$

$$= E\Psi$$

where the "Slater" subscript has been dropped and atomic units are utilized. The three terms of the Hamiltonian are the kinetic energy, the external potential energy, and the coulomb interaction energy, respectively. The energy is then $E = \int\int \cdots \int \Psi^* H \Psi\, dr_1 dr_2, \dots, dr_n$. Note that the external potential energy contribution is found to be: $\int v(r)\, \rho(r) dr.$, i.e. a functional of the density. Furthermore, the rest of the energy term contributions, i.e. kinetic and coulomb, are generic in form; in other words, they are the same irrespective of the system, which is characterized by the external potential $v(r)$. In fact, Hohenberg and Kohn [11] showed that the density $\rho(r)$ is uniquely determined by $v(r)$. In addition, they showed that the density corresponding to the minimal energy of the system is indeed the ground state density. Hence, if the form of the system energy can be written as a functional of the density, i.e. $E = F[\rho(r)]$, one can obtain the ground state energy by minimizing the functional.

Up till this point in this discussion, the form of the functional $F[\rho(r)]$ which Hohenberg and Kohn arrive at is: $E = F[\rho(r)] = \frac{1}{2}\int v(r)\rho(r)dr + G[\rho(r)]$, where $G[\rho(r)]$ is a to-be-determined functional that accounts for the kinetic and coulomb energy contributions. Hohenberg and Kohn rewrote this functional as:

$$E = F[\rho(r)] = \int v(r)\rho(r)dr + \frac{1}{2}\int \frac{\rho(r)\rho(r')}{|r-r'|}drdr' + H[\rho(r)]$$

where $H[\rho(r)]$ is new functional that is simply:

$$H[\rho(r)] = G[\rho(r)] - \frac{1}{2}\int \frac{\rho(r)\rho(r')}{|r-r'|}drdr' = G[\rho(r)] - U_C[\rho(r)]$$

where $U_C[\rho(r)]$ is the classical coulomb energy explicitly written in functional form. Note this remains an exact formulation; the addition of the classical coulomb energy term is balanced by the addition of a new functional $H[\rho(r)]$ as defined above. Though the exact form of the H (or G) functional have yet to be determined, Kohn and Sham, in a subsequent publication [12], proceeded at extruding one more term, one akin to the kinetic energy, from the energy functional $G[\rho(r)]$, on their way to deriving a practical form of minimizing the total energy E. To do this, the density, $\rho(r)$, is expressed as the sum of one-electron wavefunction densities:

$$\rho(r) = \sum_{i=1}^{N} \psi_i^*(\mathrm{r})\psi_i(\mathrm{r})$$

where the one-electron wavefunctions $\psi_i(r)$are to be determined. The form of the Kohn-Sham total energy functional is then the following:

$$E = F[\rho(r)] = \left(\frac{1}{2}\sum_{i=1}^{N}\int \psi_i^*(\mathrm{r})\nabla^2\psi_i(\mathrm{r})\,dr\right) + \int v(r)\rho(r)dr + \frac{1}{2}\int \frac{\rho(r)\rho(r')}{|r-r'|}drdr' + E_{xc}[\rho(r)]$$

where $E_{xc}[\rho(r)]$ is a new functional that is simply:

$$E_{xc}[\rho(r)] = H[\rho(r)] - \left(\frac{1}{2}\sum_{i=1}^{N}\int \psi_i^*(\mathrm{r})\nabla^2\psi_i(\mathrm{r})\,dr\right) = H[\rho(r)] - T_s[\rho(r)]$$

where $T_s[\rho(r)]$ is the kinetic energy of a many-body non-interacting system. Since a stationary total energy is sought (i.e. the minimum energy), one performs a variation of $E[\rho(r)]$, which is equivalent to a variation of E over ψ_i. The explicit variation is detailed here since it is somewhat glossed over in the original Kohn-Sham publication [12].

The goal here is to obtain an expression for the following variation:

$$\lim_{\varepsilon\to 0}\frac{E[\rho(r)+\varepsilon\delta(r)]-E[\rho(r)]}{\varepsilon}$$

$$=\lim_{\varepsilon\to 0}\frac{E[\psi_1(r)+\varepsilon\delta_1(r),\psi_2(r)+\varepsilon\delta_2(r),\dots,\psi_N(r)+\varepsilon\delta_N(r)]-E[\psi_1(r),\psi_2(r),\dots,\psi_N(r)]}{\varepsilon}$$

where $\delta(r)$ and $\delta_i(r)$ are arbitrary functions under the constraint:

$$\int \rho(r)+\varepsilon\delta(r)dr$$

$$=\int\sum_{i=1}^{N}\big(\psi_i(r)+\varepsilon\delta_i(r)\big)^*\big(\psi_i(r)+\varepsilon\delta_i(r)\big)\,dr$$

$$=\int\sum_{i=1}^{N}\psi_i(r)^*\psi_i(r)\,dr=\int\rho(r)dr=N$$

where N is the number of electrons in the system. The Kohn-Sham functional expression for E (as found above) has four terms:

1. $T_s[\rho(r)] = T_s[\psi_1(\mathrm{r}),\psi_2(\mathrm{r}),\dots,\psi_N(\mathrm{r})] = \frac{1}{2}\sum_{i=1}^{N}\int \psi_i^*(r)\nabla^2\psi_i(r)\,dr$

2. $V[\rho(r)] = V[\psi_1(\mathrm{r}),\psi_2(\mathrm{r}),\dots,\psi_N(\mathrm{r})] = \sum_{i=1}^{N}\int v(r)\psi_i^*(r)\psi_i(r)\,dr$

3. $U_C[\rho(r)] = U_C[\psi_1(\mathrm{r}),\psi_2(\mathrm{r}),\dots,\psi_N(\mathrm{r})] = \frac{1}{2}\sum_{i,j=1}^{N,N}\int \frac{\psi_i^*(r)\psi_i(r)\psi_j^*(r')\psi_j(r')}{|r-r'|}drdr'$

4. $E_{xc}[\rho(r)] = E_{xc}[\psi_1(\mathrm{r}), \psi_2(\mathrm{r}), \dots, \psi_N(\mathrm{r})] = \mathrm{T.B.D.}$

In addition, we include the above the constraint in E as follows:

$$E = T_s[\rho(r)] + V[\rho(r)] + U_C[\rho(r)] + E_{xc}[\rho(r)] - \lambda\left(\int \rho(r)dr - N\right)$$

where the last term is simply zero, and λ is a Lagrange multiplier constant to be utilized in performing the variation of E. We now perform the variation of E term by term:

1.

$$T_s[\rho(r) + \varepsilon\delta(r)] = \frac{1}{2}\sum_{i=1}^{N}\int \left(\psi_i(r) + \varepsilon\delta_i(r)\right)^*\nabla^2\left(\psi_i(r) + \varepsilon\delta_i(r)\right)dr$$

$$= \frac{1}{2}\sum_{i=1}^{N}\int \psi_i^*(r)\nabla^2\psi_i(r)\,dr + \frac{1}{2}\sum_{i=1}^{N}\int \varepsilon\delta_i^*(r)\nabla^2\psi_i(r)\,dr$$

$$+ \frac{1}{2}\sum_{i=1}^{N}\int \varepsilon\psi_i^*(r)\nabla^2\delta_i(r)\,dr + \mathrm{H.O.T.}$$

The last term can be integrated-by-parts twice (recognizing that $\lim_{r\to\infty}\psi_i(\mathrm{r}) = \lim_{r\to\infty}\nabla\psi_i(\mathrm{r}) = 0$), thus yielding the complex conjugate (C.C.) of the above second term. Hence, $\lim_{\varepsilon\to 0}\frac{T_s[\rho(r)+\varepsilon\delta(r)] - T_s[\rho(r)]]}{\varepsilon} = \frac{1}{2}\sum_{i=1}^{N}\int(\delta_i^*(r)\nabla^2\psi_i(\mathrm{r}) + \ \mathrm{C.C.})\,dr$.

2.

$$V[\rho(r) + \varepsilon\delta(r)] = \sum_{i=1}^{N}\int v(r)\left(\psi_i(r) + \varepsilon\delta_i(r)\right)^*\left(\psi_i(r) + \varepsilon\delta_i(r)\right)dr$$

$$= \sum_{i=1}^{N}\int v(r)\psi_i^*(r)\psi_i(r)\,dr + \sum_{i=1}^{N}\int \varepsilon v(r)(\delta_i^*(r)\psi_i(r) + \ \mathrm{C.C.})\,dr + \mathrm{H.O.T.}$$

Thus, $\lim_{\varepsilon\to 0}\frac{V[\rho(r)+\varepsilon\delta(r)] - V[\rho(r)]]}{\varepsilon} = \sum_{i=1}^{N}\int v(r)(\delta_i^*(r)\psi_i(r) + \ \mathrm{C.C.})\,dr$.

3.

$$U_C[\rho(r)+\varepsilon\delta(r)]$$

$$=\frac{1}{2}\sum_{i,j=1}^{N,N}\int\frac{\left(\psi_i(r)+\varepsilon\delta_i(r)\right)^*\left(\psi_i(r)+\varepsilon\delta_i(r)\right)\left(\psi_j(r')+\varepsilon\delta_j(r')\right)^*\left(\psi_j(r')+\varepsilon\delta_j(r')\right)}{|r-r'|}drdr'$$

$$=\frac{1}{2}\sum_{i,j=1}^{N,N}\int\frac{\psi_i^*(r)\psi_i(r)\psi_j^*(r')\psi_j(r')}{|r-r'|}drdr'$$

$$+\frac{1}{2}\varepsilon\sum_{i,j=1}^{N,N}\int\frac{\left(\delta_i^*(r)\psi_i(r)\psi_j^*(r')\psi_j(r')+\delta_j^*(r')\psi_j(r')\psi_i^*(r)\psi_i(r)\right)+\text{C. C.}}{|r-r'|}drdr'+\text{H. O. T.}$$

Note that the two terms in parentheses, as found in the second integrand, are equivalent upon integration. Hence,

$$U_C[\rho(r)+\varepsilon\delta(r)]$$

$$=\frac{1}{2}\int\frac{\rho(r)\rho(r')}{|r-r'|}drdr'+\varepsilon\sum_{i=1}^{N}\int\frac{\rho(r')(\delta_i^*(r)\psi_i(r)+\text{ C. C. })}{|r-r'|}drdr'+\text{H. O. T.}$$

Thus, $\lim_{\varepsilon\to0}\frac{U_C[\rho(r)+\varepsilon\delta(r)]-U_C[\rho(r)]]}{\varepsilon}=\sum_{i=1}^{N}\int\frac{\rho(r')(\delta_i^*(r)\psi_i(r)+\text{C.C.})}{|r-r'|}drdr'$.

4. Since $E_{xc}[\rho(r)]$ is yet to be determined at this point, we assume (this is not a trivial assumption … in fact, it may not be true!) that its variation can be written as: $\lim_{\varepsilon\to0}\frac{E_{xc}[\rho(r)+\varepsilon\delta(r)]-E_{xc}[\rho(r)]]}{\varepsilon}=\sum_{i=1}^{N}\int\mathbb{E}_{xc}(r)(\delta_i^*(r)\psi_i(r)+\text{ C. C. })\,dr$.

Finally, the variation of the Lagrangian multiplier constraint term, which can alternatively be written as

$L[\rho(r)]=\lambda(\int\rho(r)dr-N)=\sum_{i=1}^{N}\lambda_i(\int\psi_i^*(r)\psi_i(r)\,dr-1)$,

is: $\lim_{\varepsilon\to0}\frac{L[\rho(r)+\varepsilon\delta(r)]-L[\rho(r)]]}{\varepsilon}=\sum_{i=1}^{N}\int\lambda_i(\delta_i^*(r)\psi_i(r)+\text{ C. C. })\,dr$.

Summing up all the above variation terms, one arrives at the variation of the total energy:

$$\lim_{\varepsilon \to 0} \frac{E[\rho(r) + \varepsilon\delta(r)] - E[\rho(r)]]}{\varepsilon}$$

$$= \sum_{i=1}^{N} \frac{1}{2} \int \left(\delta_i^*(r) \left(\nabla^2 + v(r) + \int \frac{\rho(r')}{|r - r'|} dr' + \mathbb{E}_{xc}(r) + \lambda_i \right) \psi_i(\mathrm{r}) \right) + \mathrm{C.C.}\, dr$$

$$= 0$$

where we assume $v(r)$ and $\mathbb{E}_{xc}(r)$ are Hermetian, and λ_i are real. In order for this expression to be zero for arbitrary $\delta_i(r)$, the above integrand term must have the form:

$$\left(\nabla^2 + v(r) + \int \frac{\rho(r')}{|r - r'|} dr' + \mathbb{E}_{xc}(r) \right) \psi_i(\mathrm{r}) = \lambda_i \psi_i(\mathrm{r})$$

for $i = 1 \ldots N$. (Note that since we assume $v(r)$ and $\mathbb{E}_{xc}(r)$ are Hermetian, the expression in parentheses is Hermetian, and hence λ_i are real.) These set of equations are called the Kohn-Sham eigenvalue equations, and are at the heart of any DFT solver implementation. Determining the ground state density is simply a matter of solving for the Kohn-Sham eigenvalues $\lambda_i$and Kohn-Sham eigenvectors ψ_i, which is usually accomplished using a self-consistent method.

One crucial outstanding matter remains, however: an explicit expression for $\mathbb{E}_{xc}(r)$. At the time of this writing, this remains an open question for no exact form for $\mathbb{E}_{xc}(r)$ is yet known. Instead, different approximations (functionals) have been proposed, which include the local-density-approximation (LDA) and the generalized-gradient-approximation (GGA), which are used in this work.

2.3. Angle Resolved Photoelectron Emission Spectroscopy

The history of photoemission spectroscopy dates back to the early investigations of light behaving more like a particle rather than a wave, as deduced during the early 1900's. The famous photoelectric effect experiments of Hertz and others showed that for wavelengths below a material specific threshold (i.e. frequencies above a certain threshold), electrons would be emitted from a material at a kinetic energy that was inversely proportional to the wavelength of the incident light. This helped lead to the deduction that light behaves like a particle with an amount of energy that is directly proportional to its frequency. Further investigations revealed that the photoemission intensity varied with angle [13] which were followed up by theoretical treatments starting in 1945 [14]. In 1964, Kane [15] reported on the implications of momentum conservation to electronic structure determination and predicted it "would be reasonable to expect that momentum-conserving emission from perfect surface states will also be observable". This indeed proved to be the case as evidenced beginning in the 1970's of synchrotron-based photoemission measurement spectra revealing both bulk and surface state bands [13].

The physics of angle resolved photoemission can be accounted for using several models of increasing sophistication and accuracy, beginning with the so-called "three-step model", moving up to the "one-step model" and finally a quantum field theoretic description. A detailed analysis of these models may be found in texts and review articles devoted to photoemission spectroscopy, see for example [13, 16]. Here, we give a very brief overview of the simplest theory and discuss its application to mapping the electronic structure of crystalline material systems. Photoemission can be modeled using semi-classical time-dependent perturbation theory, from which Fermi's "Golden rule" is derived:

$$PE\ intensity\ \propto \left|\langle\psi_f|H_p|\psi_i\rangle\right|^2 \rho_{DOS}$$

The expression for the photoemission operator, i.e. the perturbing hamiltonian H_p, is $\hat{\hat{p}} \cdot \boldsymbol{A} + \boldsymbol{A} \cdot \hat{p}$. For many photoemission work, a dipole component approximation, using a Taylor expansion of the electromagnetic vector potential $\boldsymbol{A}$, is usually invoked, since that is the predominant contribution from the photon excitation; for the work presented here, this is not necessary. Using the Coulomb gauge ($\nabla \cdot \boldsymbol{A} = 0$) and stipulating a periodic potential, the photoemission intensity is found to be proportional to:

$$PE\ intensity\ \propto \left|\langle\psi_f|\boldsymbol{A} \cdot \hat{p}|\psi_i\rangle\right|^2 \rho_{DOS} \propto \left|\sum_{G_i,\, G_f} a_{G_i}\, b_{G_f}\, \boldsymbol{A} \cdot (k_i + G_i) \int e^{-i\,(\boldsymbol{k_f} - \boldsymbol{k_i}) \cdot \boldsymbol{x}}\, d\boldsymbol{x}\right|^2 \rho_{DOS}$$

Note that in order for the integrand in the above rightmost expression to be nonzero, the crystal momentum of the initial and final state need to be the same. Thus, this selection rule leads to conservation of parallel crystal momentum in the case of surface photoemission, where the periodicity is in the plane of the surface. This crystal momentum can be deduced from the photoemitted "free" electron based on its angle of emission, θ, and its energy, E_f, using the following simple relation:

$$k_{||} = \sqrt{\frac{2\,m\,E_f}{\hbar^2}} \sin\theta$$

The energy of the initial state is arrived at by conservation of energy:

$$E_i = E_f - hv$$

Often, however, energies are referenced with respect to the Fermi level instead of the vacuum level.

2.4. Custom-built Knudsen Cell

During the early development of a recipe for Co wire synthesis, it became abundantly clear that controlled deposition by way of simple Co wire wound around a tungsten filament would not be tenable, as it was neither reproducible in deposition rate

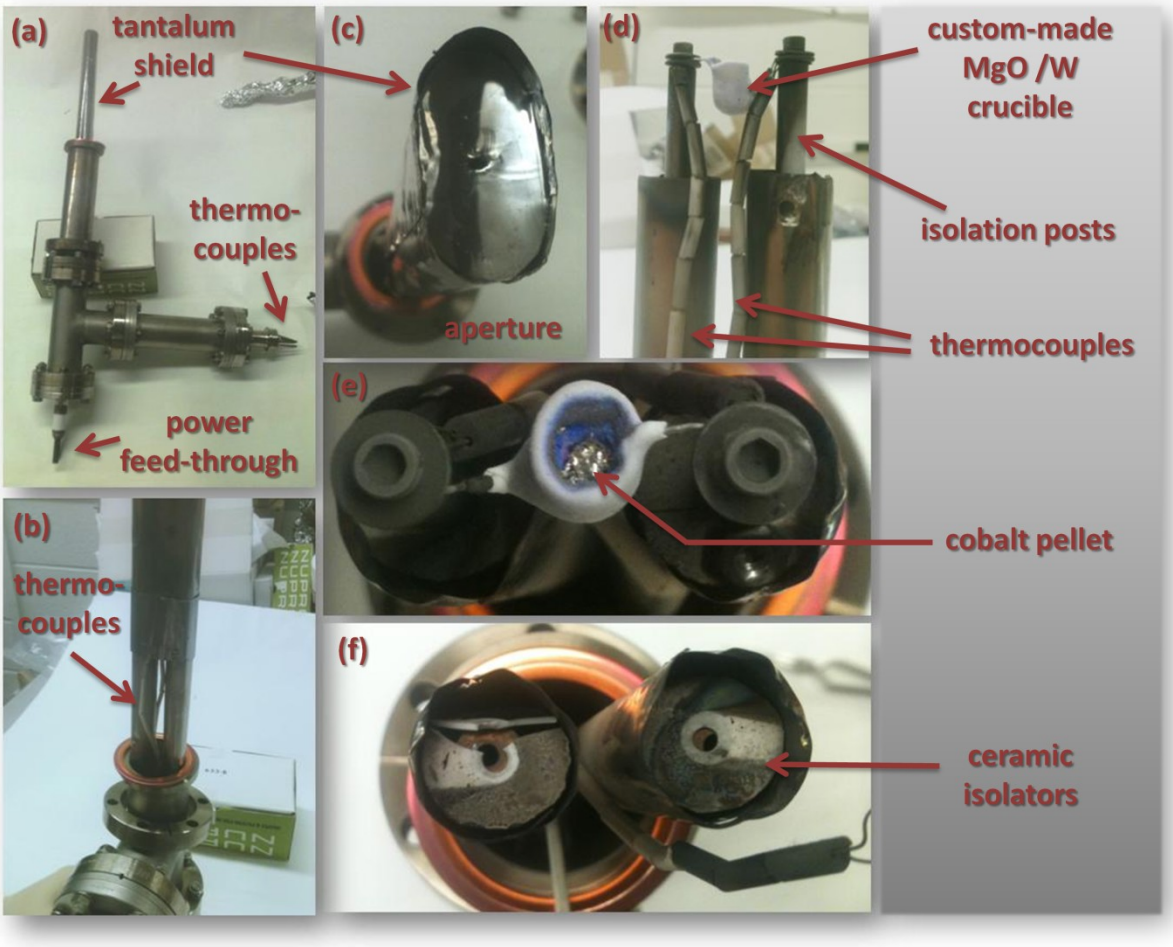

Figure 2.1 Custom-built Knudsen cell for physical vapor deposition of Cobalt. (a) the fully assembled Knudsen cell ready for mounting on a UHV chamber. (b) same as (a) but with external stainless-steel UHV tube removed. (c) top view of deposition source, revealing source aperture. (d) removal of tantalum shield reveals a hand-made ceramic crucible in contact with thermocouple leads. (e) top view of (d) revealing cobalt pellet inside the ceramic crucible. (f) same as (e) but with crucible and isolation posts removed. The ceramic discs (one is cracked), serve to electrically isolate the tantalum shields from the copper power feedthroughs (which deliver power to the ceramic enclosed tungsten filament)

nor physically stable in filament lifetime, due in part to alloying of cobalt with tungsten. Thus, a custom-designed UHV capable Knudsen cell was fabricated by the author using the available Columbia machine shop facilities. The basic building blocks of the Knudsen cell, shown in Figure 2.1, consisted of (i) a power feedthrough with 1/4" diameter copper posts, capable of supplying ample current to the heating source, (ii) a custom made crucible made by hand using a MgO chemical epoxy (Aremco 571) that covers a 0.375mm diameter tungsten filament, wound in the shape of a basket, (iii) a tantalum shield with aperture that inhibits contamination of the UHV chamber and restricts deposition flow to within a small divergence angle, all while not substantially degassing (for tantalum is a refractory metal with a very high melting temperature of 2996°C, while cobalt melts at 1495°C), and (iv) electrically isolated thermocouples that allow for consistent negative feedback control of the deposition source. The fabricated Knudsen cell provided a repeatable source of cobalt for physical vapor deposition, and performed at near UHV conditions of $\sim 5 \times 10^{-10}$ Torr.

2.5. Custom instrumentation for sample preparation

Sometimes, a lab group finds itself in need of an automation solution, but does not have the financial resources to afford "off-the-shelf" pre-built instrumentation. In these cases, a "build-it-yourself" solution is required. Specifically, the desired features consisted of the ability to: (i) provide a power load output at constant current $\geq$ 6A, (ii) measure the ultra high vacuum pressure reading from a gauge and convert to an ASCII readable form, (iii) interface with a sputter controller and allow for remote control, (iv) communicate to and accept commands from a user by way of a serial link to a computer. These requirements are met in the custom instrumentation tool shown in Figure 2.2, which has

been in use in the lab for 7+ years. Notable features of this instrument include the use of a readily available and quite affordable (i.e. cheap!) computer power supply to provide not only power for the digital and analog electronic circuitry, but also to provide the load power for the ≥ 6A constant current source.

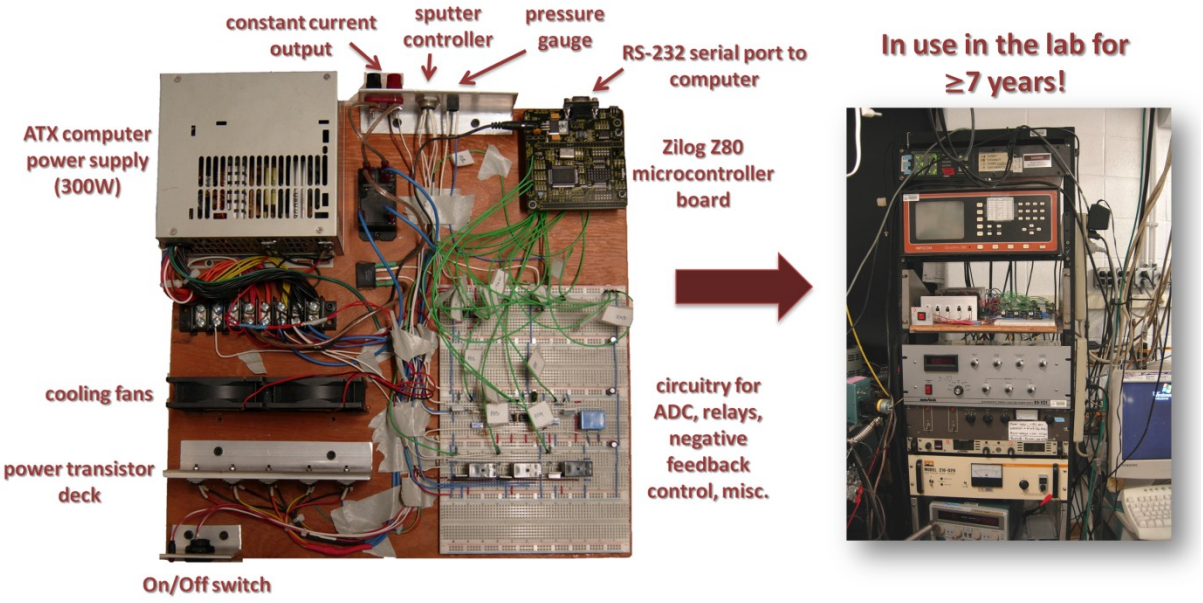

Figure 2.2 Custom instrumentation with the ability to provide a controlled constant supply current of ≥6A, measurement of UHV gauges, and remote command of sputter controller, all by way of a serial interface to a computer. The power supply of the instrument is an old ATX computer power supply donated to the lab by the author.

3. Self-Assembly Growth of Co Atomic Chains

One-dimensional nanoscale systems, including atomic chains or wires, have been predicted to display a wide range of unusual physical properties [17]. The compelling physics of low-dimensional phenomena has led to the exploration of atomic-wire preparation techniques. One approach has been the use of stepped surfaces to form regular arrays via self-assembly [18]. These large-area step arrays are suitable for photoemission studies of the electronic structure [19, 20]; furthermore, this approach allows the degree of coupling between wires to be changed controllably through choice of vicinal cut. However, in step-edge growth, more complex processes may occur, including growth of islands or interdiffusion into the underlying substrate. These processes lead to important unresolved questions regarding step-mediated self-assembly of bimetallic-wire arrays, including an understanding of the basic physical parameters, which can, in turn, guide the choice of a particular materials system and lead to growth methods that ameliorate chemical mixing.

Due to the interest in spin-valves, the bimetallic system Co/Cu(111) has been studied extensively [21-25]. Several experiments employed non-vicinal, i.e. with terrace widths ≥100Å, Cu(111) surfaces for spin-polarized investigations of Co nanostructures, most notably of 2ML high triangular islands [25]. However, the exact atomic make-up of these nanostructures remains in question. For example, it has been argued that the islands form on a buried layer of Co and that Cu migrates to the outer perimeter of the islands [23]. In one instance, room-temperature (RT) scanning tunneling microscopy (STM) has been used to examine the self-assembly of Co island chains, ~50Å in width, along the edges of isolated Cu steps [22]. These chains appeared as 4Å-high protrusions at the step edge and

thus were neither single-atom in width or height. Finally, Monte Carlo simulations [26] and density functional theory (DFT) calculations [27] have been used to investigate the self-assembly mechanism of Co wires at a Cu(111) step. Though there are differences in the details of their predictions of an atomic-wire surface phase, both suggested that laterally encapsulated Co wires are formed during self-assembly.

In general, these earlier large-terrace studies show clearly that Co accumulates at the Cu(111) step edges during growth. However several compelling and important questions remain about surface self-assembly on narrow-terrace width vicinal Cu(111): first, can uniform Co wires of atomic width form at straight step edges; second, will such Co wires be laterally encapsulated by Cu at the step edge, as predicted theoretically; and finally, do other more complex Co atomic structures exist at RT if the terraces approach atomic dimensions.

In this chapter, we answer these questions by using in situ STM as a probe of Co self-assembly on a Cu(775) step template. This substrate represents an $8.5°$ miscut of a Cu(111) surface, resulting in a terrace width of only 14.3Å or approximately seven atomic rows, separated by B-type steps. The crystallographic direction along the step edge is $[1\,\bar{1}\,0]$ while that perpendicular to the step edge is $[1\,1\bar{2}]$. Our study concentrates on low-coverage regimes in order to observe and clearly identify the initial Co step-edge nucleation structure. As will be shown, our experimental findings clearly show a new phase at which low-coverage growth leads to self-assembly of long straight atomic wires.

3.1. Co Nucleation On Cu(111) Steps: Prior Experimental Work

As mentioned in the introduction, there have been several experimental studies of Co deposited on Cu(111). One of the earliest studies, by Figuera et al. [28], looked at RT deposition of Co. In addition to bilayer triangular islands on terraces as well as 1ML terrace vacancies, they observed island nucleation at both the top and bottom of the step edge. This group pointed out subsequently [29] that the islands are comprised of a mixed phase of Co and Cu. Note that this morphology was observed at coverages as low as 0.1ML [29]. Finally note that a recent Co/Cu(111) study by Chang et al. [24] reported 2nm wide islands on the upper step edge at a coverage of 0.09ML.

Based on the above mentioned step nucleation morphology that is present for RT deposition, Figuera et al. [21] subsequently reported growth of chains of Co islands on Cu(111) step bunches. For a coverage of 0.2ML and an average step width of 10nm, the average island width was 5nm. Note that vacancy islands had also formed as a result of the step-island nucleation.

In addition to Co growth at RT, other groups have examined low-temperature deposition on Cu(111). For example, Pedersen et al. [23] observed “ramified islands”, i.e. bilayer islands connected by monolayer islands, for Co deposited at 150K and imaged at 170K (i.e. not annealed to RT). The bilayer islands were found both at the bottom and top of the step edges, as well as on the terraces. This group also suggested that the bilayer islands sat, in fact, on an embedded layer of Co and that the islands were terminated on their perimeter by Cu atoms. Furthermore, this work showed that, if annealed to RT, interdiffusion of this Cu brim occurred. In a second low-temperature-deposition experiment, Speller et al. [30] deposited Co at 140K and then slowly elevated the sample to

RT for imaging. At a coverage of ~0.12ML and a step density of 1/200 to 1/1000Å, they observed step island growth only at the top of the steps; however, step-island nucleation at the bottom of the steps commenced at about 0.4ML for their conditions. In their experiment, the islands were found to be a mixed surface phase of Co and Cu with an average width of 5nm. The intermixed nature of the islands was supported by the concomitant formation of vacancy islands.

In summary, despite extensive prior work in the Co/Cu materials systems, no atomic wires of Co on Cu(111) surfaces were observed experimentally, although the existence of Co wires at Cu step edges was predicted theoretically[26, 27]. Note, however, that there are several reports of the direct observation of atomic wires in different bi-metallic systems, e.g. Fe/Cu(111) [31].

3.2. Experiment

Cu(775) was prepared using repeated sputter/anneal cycles in an UHV chamber with a base pressure less than 1×10−10 Torr. Auger measurements showed no detectable contamination and surface electron diffraction showed the split spots characteristic of a stepped surface. Co was deposited from a heated ceramic crucible with the Cu sample cooled to ~165K. The cooling was a precaution against interdiffusion during sample preparation. Co coverage was measured using STM scans and assumptions of Co locations, which gave an estimated error of ~0.02ML. Using the aforementioned coverage estimation, the calculated average deposition rate for this work was 0.01ML/min. After deposition, the sample was brought to RT for the STM studies. All the scans were performed using a

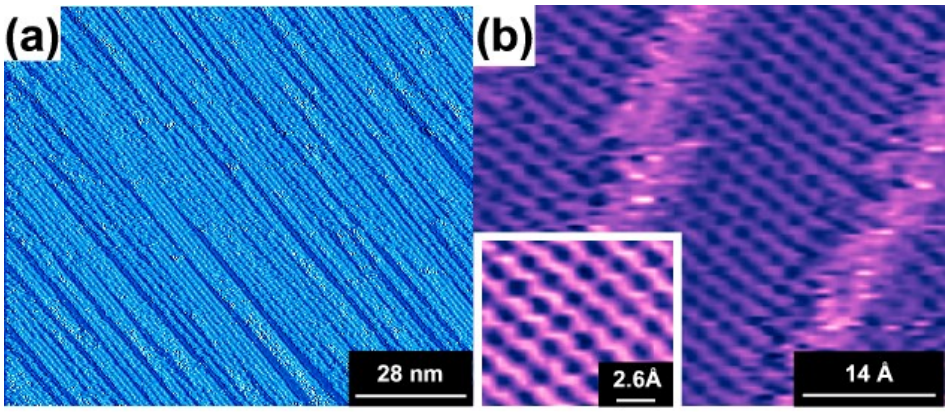

Figure 3.1 STM images of Cu(775) at RT, taken at V_{sample}=0.5V and I=150pA; the images are *dz/dx* (i.e. derivative). (a) 100×87nm^2 scan showing relative uniformity of step spacing. (b) Atomic-resolution scan of steps showing "frizz". Inset, topographical close-up of step terrace clearly revealing the (111) surface.

tungsten tip, the sample biased at +0.5V with respect to the tip, and a feedback tunneling current of 150pA.

3.3. Results and Discussion

An STM image of the clean Cu(775) surface is shown in Fig. 3.1. At room temperature, this surface exhibits unstable step edges or "frizz" [32] as shown in the atomic resolution image (Fig. 3.1(b)). This step instability has been attributed to kink motion at the step-edge or to step-tip interaction [33]. The steps in Fig. 3.1 have an average height of 2.1Å and the step edges appear rounded in both plan view and in profile due to tip-step convolution. As will be shown below, the lack of frizz denotes the presence of Co, which pins step-edge motion.

Figure 3.2(a) displays a derivative image taken at a Co coverage of ~0.09ML. Compared with the frizz at a clean Cu step, visible on the left, the figure shows that one-atom-wide wires have formed, distinguishable by their straight edges and uniform widths.

The sharp or straight-edge appearance of the step-edge-assembled wires is attributed to the pinning of substrate step atoms by Co atoms. The measured "cross-section" over two steps indicated in the figure and shown in the inset suggests that the wires are approximately 3.0Å wide, which is comparable to the Cu row-row spacing of 2.2Å. Again, due to tip-step convolution, the step profile appears rounded resulting in a larger apparent wire width. Tunneling into the Co wires at a bias of +0.5eV above the Fermi level at constant current requires the tip to remain closer to the surface than for tunneling into the Cu substrate. Chemical contrast by STM is a well-known phenomena; see for example the related case of Co/Pt(111) [34, 35], which reports similar results to ours for both Co in the Pt terrace and at the step edge. However, though there have been several previous STM studies of the Co/Cu(111) system, this particular example of chemical contrast on this specific system, which allows the differentiation of Co step-edge wires from the Cu atoms on a Cu(111) terrace, has apparently not been commented on before. We note that a similar, though smaller effect, was observed for 2-3ML high Co islands surrounded by rims of several Cu atoms [23]. For one-atom wires this effect produces a small but clearly observable inflection in the step edge located approximately $1/2$ to $3/4$ up the step height of Cu. Note that this uniform inflection along the step edge is not seen at Cu steps where the step edge exhibits frizz; hence, this inflection is not likely due to a double-tip.

As shown in Fig. 3.2(b), two-atom-wide wires were observed at a slightly higher Co coverage of about 0.12ML. These ~5.4Å-wide wires possess an average height of 1.5Å, less than that of a pure Cu step height, as seen for frizzy steps. This result further supports the discussion regarding the inflection measured in the profile of the one-atom-wide wires. We note that the local density of states may be affected by quantum-size effects due to the

atomic scale of the wires, as seen, for example, in the case of atomically fabricated chains of Cu on Cu(111) [36].

The growth physics of these Co wires can also be examined via wire-length distributions measured from the STM images. Thus, in Fig. 3.3, one-atom wire histograms are given for the two different coverages mentioned above, namely 0.09ML and 0.12ML. The histograms clearly reveal an increase in the length of the wires as coverage is increased. Specifically, the average wire length at 0.09ML is found to be ~27 atoms with a

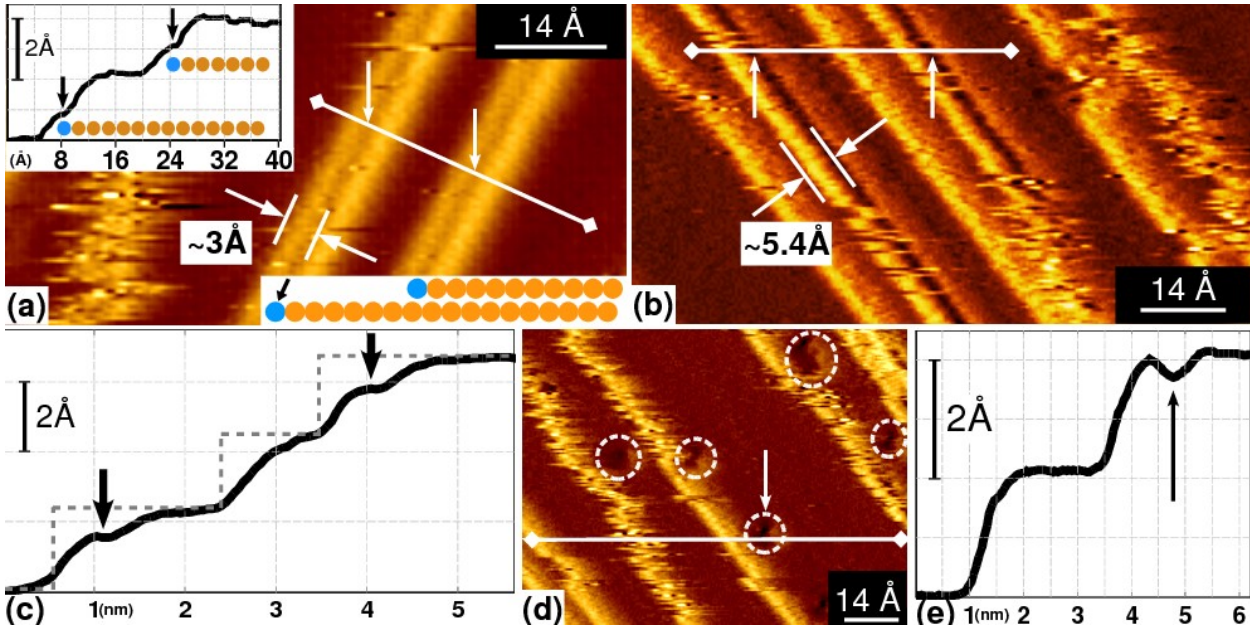

Figure 3.2 STM derivative images of Cu(775) at RT after deposition of Co. Blue-colored circles denote Co atoms and gold-colored circles denote Cu atoms. The black arrows in the topographical profiles correspond to positions indicated by white arrows in the images. (a) Scan showing one-atom-wide Co wires; frizz is seen on a clean step edge at the left of the image. The inset is a topographical profile along the direction of the corresponding white line in the image. Coverage is 0.09ML. (b) Scan showing two-atom-wide Co wires, as well as one-atom-wide wires and clean-steps. A plateau, denoted by arrows, is seen for the two-atom wide wire scan; in this image, the plateau is not seen for one-atom-wide wires presumably due to finite tip radius and the narrowness of the wires; however, the lack of frizz is a strong indication of Co at the step edge. Coverage is 0.12ML. (c) Profile for white line in (b). The gray dashed line serves merely as a step guide for the eye and does not denote the exact position of the steps. (d) Scan showing terrace-embedded Co. Coverage is 0.12ML. (e) Embedded Co appears as depressions, as indicated by the arrow, in the step terrace.

standard deviation of 22 atoms and a maximum observed length of 105 atoms; at the higher coverage of 0.12ML, the average length had increased to ~40 atoms with a corresponding increased standard deviation of 37 atoms and a maximum observed length of 141 atoms. Note that the measurements are for one-atom wires only and do not include the wire-length distribution for 2-atom wide wires nor the terrace-site-exchange (see below), which are also observed at the higher 0.12ML coverage; hence, the one-atom wide wires increase in length despite the fact that these other atomic morphologies are starting to form. This observation of increasing wire-length with coverage provides insight into the wire self-assembly mechanism, as will be discussed below.

In addition to Co wires at the step edges, depressions are seen in step terraces, such as those in the regions marked by circles in Fig. 3.2(d). Several observations are consistent with these depressions reflecting Co atoms locally embedded in the terrace. First, the maximum apparent depth of these depressions is ~0.5Å which is consistent with the observed height difference between the wires and adjacent terraces. Second, this depth agrees well with similar 0.6Å deep depressions observed on the Co/Cu(001) system [37]. Third, if the apparent depressions happened instead to be terrace vacancies, i.e. 2Å deep, tip-convolution effects would likely not account for the measured shallow depth, since smaller features (2-atom wide wires) were also resolved along the same scan line of the depressions. Co-induced atom vacancies (etch pits) have been previously reported for Co/Cu(111) systems [21]. However, the pits, which were observed at a comparable Co coverage of 0.1ML, were much larger, ~2Å deep and 80Å in diameter, than found in the present study. Furthermore, the etch pits observed in the earlier study were commensurate with adatom-island formation, which is not seen at the same coverage in

this study. Thus, as in the case for the wires, we attribute the depressions to a change in the local density of states (LDOS) due to Co–Cu substitution rather than a vacancy formation. We also note that this observation supports the long-held hypothesis [23] that Co/Cu(111) islands, seen by us at higher coverage, do indeed bind to a terrace-embedded Co layer. Given the narrow step width, the displaced Cu atoms most likely attach to the step edges and become part of a mobile step kink, appearing as frizz. For completeness, we note that Co is also known to adsorb on Cu(111) terraces as demonstrated by several low-temperature STM studies [38-40]; our observations show, however, that the temperature range we are operating in is energetic enough to allow for terrace-site exchange in addition to terrace diffusion.

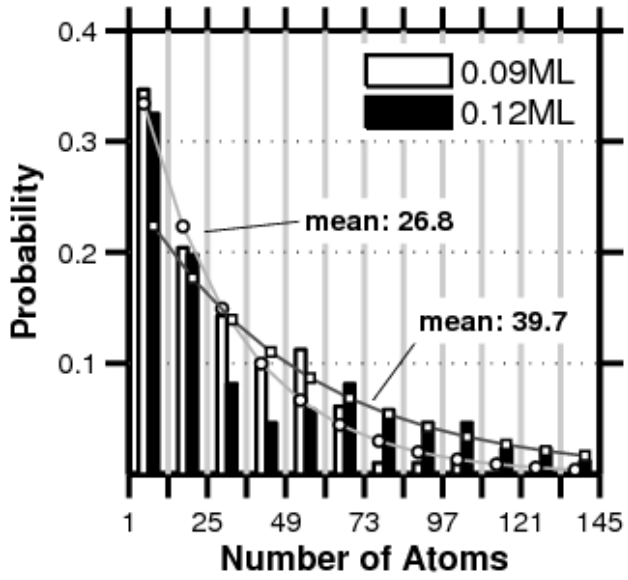

Figure 3.3 Distribution of 1-atom-wide Co wire lengths. The smooth grey curves denote a fit based on a one-dimensional lattice gas model; see discussion in text. At a coverage of 0.09ML (circles), the average wire length is a ~27 atoms. As the coverage is increased to 0.12ML (squares), the average wire length increases to ~40 atoms, indicating that wire length increases with coverage. This result is in accord with a growth mechanism, in which the Co atoms move facilely along the step edge until encountering a wire end, to which the Co atom attaches. Note that in comparison to the typically reported widths of nanometer-scale islands at step edges (5nm or ~20 atoms), the 1- and 2-atom (not shown above) wires have grown to much longer length scales.

The occurrence of embedded atoms raises important questions, including the kinetic pathway leading to their formation. As mentioned in the introduction, there have been theoretical studies of Co atomic-wire formation at Cu(111) steps which can serve as useful points of comparison. One particularly detailed investigation, by Mo

et al. [27], used DFT to study one- and two-atom wide wire phases of Fe, Co and W. In fact, the predictions of this study have been recently experimentally verified for the related case of Fe-wire growth, which was explicitly examined in [31]. For the case of Co wire formation, the theoretical study by Mo et al. determined a mechanism consisting of three steps: 1) formation of a single-atom-wide Co wire located one row behind the Cu step edge, 2) formation of a subsequent Co row behind the first, and 3) formation of a Co wire on top of these two rows. Despite being validated for the related case of Fe-wire growth, the predicted surface phase determined by this DFT-based calculation appears different from the phase present in our experimental results; specifically, non-encapsulated one and two-atom-wide wires are observed as opposed to the encapsulated wires predicted by calculation. Note however there are some differences between this theoretical study and the present study. For example, the calculations were performed for an A-type step, as opposed to a B-type step used experimentally. In addition, the calculations considered only a single Co atom at the step edge; higher coverages, i.e. a Co wire, might exhibit different energies. We note that the formation of the structures seen here at RT may be kinetically limited. For example, we observe a decrease in the Co Auger signal as the surface is raised above room temperature. We attribute this to either Co encapsulation by Cu or Co dissolution into the bulk. Thus higher temperatures may be required to reach the kinetic pathways leading to the final state of the DFT prediction, i.e. lateral step encapsulation. For the different scenario of deposition at a higher substrate temperature (instead of raising the substrate temperature post deposition), overall interdiffusion would probably dominate, as already evidenced by the presence of embedded terrace nucleation (Fig.

3.2(d)), rather than simply forming uniform laterally encapsulated wires. Finally, an additional comment on the lack of laterally encapsulated Co wires is discussed below.

An earlier theoretical study by Gomez et al. [26] using Monte Carlo and static relaxation provides a second interesting comparison of Co growth on Cu(111). In part, this study looked at preferential nucleation sites of Co at Cu steps and drew the following conclusions: (1) Co atoms will form "two nearly straight rows", one in front of the Cu step edge and the other behind the first row of Cu at the step edge (the latter was predicted later again by Mo et al.), (2) Co atoms were not likely to site exchange with Cu atoms on the terraces. While our work finds agreement with wire formation in front of the Cu step edge, there is no evidence of laterally encapsulated wire formation, as discussed above. Instead, the simultaneous presence of embedded-terrace nucleation suggests, paradoxically (see below), a lower energy of formation for this morphology than that of encapsulation. It should also be noted that the work of Gomez et al. did not stipulate the step type on which the simulation was performed.

In light of the two theoretical studies discussed above, our observation of terrace-site exchange without the presence of step-edge lateral encapsulation will be commented on briefly. One obvious consideration is that inclusion of additional physics appears to be important as is mentioned above. For example, the presence of significant "frizz" at the step edges indicates that Cu-atom diffusion and kink motion are present on theses edges. The presence of these surface defects and dynamics would seem to make calculation of the actual surface more complex than in the ideal theoretical models considered thus far.

In general, our observations indicate a degree of lack of uniformity in wire formation across the full surface at higher coverage. For example, as shown in Fig. 3.4(i), at

0.12ML, terrace nucleation, bi-atomic wires and bare steps can all be observed in adjacent regions of the STM image. In Fig. 3.4(ii) we show the change in the ratio of wire length to total step-edge length with coverage. These measurements show that while one-atom-wire growth dominates for 0-0.09ML and follows an ideal wire-growth pattern, the onset of two-atom-wire growth and terrace nucleation causes a reduction in the slope of one-atom wire concentration versus coverage. This change suggests that it is more energetically favorable for Co atoms to be attracted to other Co step-edge atoms, than to Cu step-edge atoms.

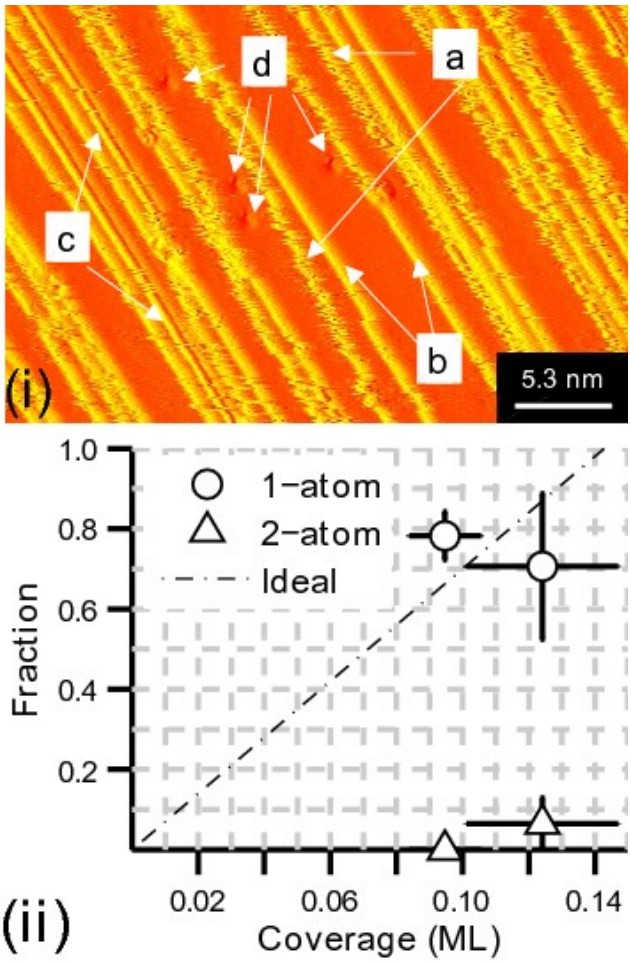

Figure 3.4 Different Co growth phases develop with increasing coverage. Top panel (i): A derivative image shows that at 0.12ML, four different "phases" exist: (a) "frizz", (b) one atom-wide wire, (c) two atom-wide wire, (d) terrace embedded Co. See details in Fig. 2(b) for the single-atom-wide wires. Bottom panel (ii): Wire-length-to-step-length ratio versus coverage. "Ideal" refers to calculated ratio for growth of only 1-atom wide wires on a perfect seven-atom-row stepped surface. The falloff in the 1-atom wire ratio above 0.09 ML is due to 2-atom-wide wire growth, terrace nucleation, and terrace-width variations; without these components, the 1-atom wire step ratio would follow that of ideal wire growth.

The observed distribution of Co atoms along the Cu steps, i.e. extended Co wires coexisting with equally extended bare Cu steps, as shown in Fig. 3.5, allows us to speculate about the relative energetics of Co atoms on vicinal Cu surfaces. Judging from our measurement of the lengths of bare Cu steps at 0.09ML, Co

atoms are sufficiently mobile on Cu (111) terraces even at 160 K, and the attractive potential of these atoms to the step edges is sufficiently shallow, that Co atoms may thermally migrate along the step edges at least 3.4 nm (our typical measured length of a clean Cu step edge at 0.09ML) before nucleating into an atomic wire. This is also evidenced by the random positions of the self-assembled wires along the step edge; in the case of Co on vicinal Au[41], on the other hand, Co atoms were found to nucleate at discommensuration lines that ran perpendicular to the steps, forming an ordered arrangement of quantum dots rather than extended atomic-wide wires. Once a wire nucleation on a Cu step edge has occurred, the ends of the wire serve as traps for otherwise mobile Co atoms. This attractiveness of the Co/Cu kinks at the ends of the wires is consistent with the growth of the extended uninterrupted Co wires.

The one-atom-wide wire-length distribution, as shown in Fig. 3.3, may be used to estimate the Co-Co interaction energy ε. We have used a one-dimensional lattice gas model [42] to fit the measured wire-length distribution, as shown by the gray curves in Fig. 3.3. The fit of the model to our wire-length distribution is particularly satisfactory, especially for the case of 0.09ML, at which coverage only 1-atom-wide wires are present. For the case of 0.12ML, 2-atom-wide wires also exist. This additional feature is not part of the model and thus the fit in that case is not as close.

In this lattice gas model, Yilmaz et al. derive an expression for the number of wires with length l, q_l, as

$$q_l = \frac{q^2}{n_1}\left(1-\frac{q}{n_1}\right)^{l-1} \qquad (1)$$

where q is the number of wires and n_1 is the number of occupied sites along the step edge. By data fitting, we find q, and by the thermal equilibrium expression for q (equation 5 in [42]), it is easily found that the interaction energy ε can be written as

$$\varepsilon = k_B T \ln\left(\frac{(n-n_1)n_1 - nq + q^2}{q^2}\right) \quad (2)$$

where n is the number of lattice sites along the step edge. Using the above formulation along with our measurements, we find an attractive Co-Co interaction energy of +5.1(±0.3) $k_B T$, or 0.13(±0.01) eV at RT. This energy is considerably lower than the bond energy expected for an isolated Co dimer[43]. This difference in bond energy between metal-substrate-supported wires and isolated wires is typical for wires on other surfaces. Thus, in the case of Ag on Pt(111), the Ag dimer bond energy has been experimentally found to be 0.150(±0.020) eV [44]. In addition, a comparable value of 0.166eV has been derived from STM measurements of 1-atom wide Ag wires on Pt(997)[45]. By contrast, the experimentally determined

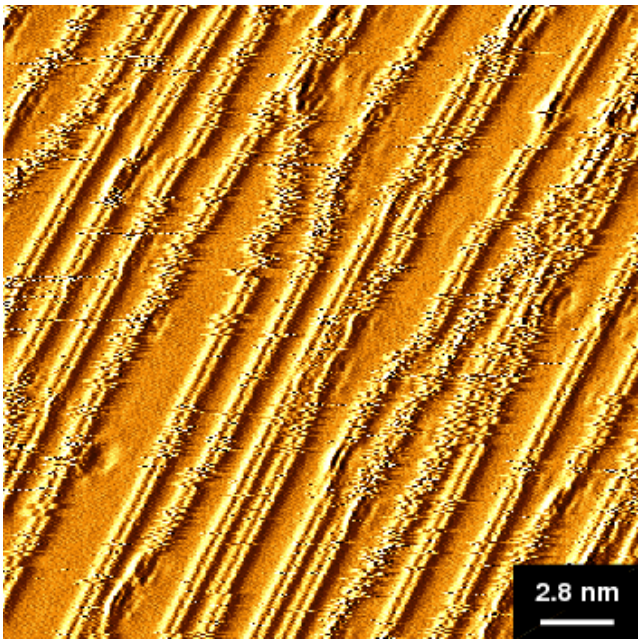

Figure 3.5 Self-assembly at 0.09ML Co coverage. This STM image (d2z/dx2, i.e. second-derivative), acquired at RT, clearly shows the presence of self-assembled 1-atom-wide Co wires along with bare Cu(111) steps. The 1-atom-wide wires appear as straight sharp double lines at the step edge. Frizz, on the other hand, causes the bare Cu(111) step edge to appear irregular. The positions of the self-assembled wires are relatively random, indicating freedom from any substrate-mediated reconstruction or discommensuration. Note: the appearance of broken/shifted wires is merely due to tip-change.

bond energy for isolated Ag2 has been found to be 1.65(±0.03) eV [43]. In summary, the energy value extracted from the lattice gas fitting seems reasonable based on the observations of other atomic-wire systems.

Note that second-row Co nucleation is not observed before the Co coverage reaches ~0.12ML (see Fig. 3.4(ii)), i.e. before a significant fraction of the Cu steps are decorated by single-atom-wide Co wires. This observation suggests that Co atoms are sufficiently mobile also along the chains of Co atoms under experimental conditions. The latter property of the system is also important for the atomic wire growth as it prevents Co island formation at low Co coverages. Finally, it would be interesting to study the influence of the Co wires on the step fluctuations of bare Cu steps, i.e. "frizz"; such a study would provide additional insight into any change in step-edge transport, see for example Tao et al.[46].

More generally, the behavior of Co atoms on the vicinal Cu surface is strongly dependent on the temperature of the system. At temperatures higher than 160K the in-terrace diffusion of Co atoms becomes possible, as has been observed in our experiments at room temperature deposition (not shown in this work). At low temperatures, shorter wires and/or island growth would be expected, as in the case of Co on vicinal Pt[18], due to decreased mobility of Co atoms. On the other hand, the wire nucleation probability strongly depends on the concentration of mobile Co atoms on the surface. This concentration was controlled by the Co deposition rates in our experiments. The higher deposition rates would lead to higher nucleation probability and, therefore, shorter wire lengths. Thus, our work offers the empirically found set of conditions (160K, 0.01ML/min), suitable for growth of extended Co wires on a Cu(775) surface. We also speculate that the coverage-

limit of 0.09ML for the self-assembly of uniform one-atom wide Co wires may be increased under more controlled growth conditions.

Straight sharp-edge wires are only seen at very low coverages, i.e. <0.2ML. If the coverage is increased above this value, a phase change is observed in the system, such that step bunching occurs and step edges appear irregular. This more complex growth morphology causes some terraces to become wider than others and as the coverage increases further, typically >0.3ML, island formation begins to occur. Similar higher-coverage effects have been reported by Gambardella et al. [18] for Co/Pt(997). A study of this higher coverage regime is currently being carried out.

The formation of one and two-atom wide Co wires, as well as terrace nucleation, is expected to modify the surface electronic structure of bare Cu(775). A recent photoemission investigation studied the modification of the Cu(775) surface state as a function of Co coverage [19]. The study clearly showed that the parallel momentum corresponding to the band minimum of the Cu surface state shifts in position at 0.03ML coverage indicating a change from a surface modulated state to a terrace modulated state at coverages corresponding to the onset of one-atom-wide wire growth. Such a shift can be expected as the randomly distributed Co wires disturb the coherence across the step superlattice and thereby preventing a coherent surface state formation extending over several terraces. The state can however still exist within the confines of an individual terrace.

3.4. Conclusion

In conclusion, we have used STM to study the formation of a new phase of one and two-atom-wide Co wires on vicinal Cu(111). These two types of wires form sequentially with increasing coverage. For this new phase, Co wires assemble only at the bottom or lower terrace of a step edge; this result contrasts with top-only or top-bottom step edge Co island growth, as seen in past experimental observations of low-coverage Co deposition on Cu(111). Interestingly, we find no evidence for lateral Cu encapsulation of the Co wires in the terrace at RT; this is in comparison to the different atomic-wire phases reported in recent theoretical works. Single-atom-wide wires are seen for coverages less than 0.09ML, but at higher coverage two-atom wide wires form; in addition terrace substitution is found to co-exist. An examination of the length distribution for low and high coverage is consistent with growth kinetics which allow high mobility of Co atoms along the step edges and attachment at wire ends. These results, obtained on a vicinal surface with terraces of 14Å average width, add new insight to the already rich set of self-assembly physics of the Co/Cu(111) bimetallic system; further theoretical study of energetics and kinetics would provide additional insight.

4. A 1-D Spin-Exchange Induced CDW Instability

As has been shown with 0-D quantum dots and 2-D single-layer atomic sheets, 1-D atomic systems are expected to exhibit novel quantum mechanical phenomena due to angstrom-scale confinement[3, 6]. The realization of true self-assembled monatomic 1-D systems which exhibit rich phenomena beyond quantum-well-like behavior[47], however, has been rare[48, 49]. Most attempts have consisted of wire growth on semiconducting surfaces[50-55], in order to reduce substrate interaction; these experiments have typically observed a charge-density-wave (CDW) instability[6] commensurate with a metal-to-insulator transition. However, these 1D systems have suffered from an inability to directly determine the crystallographic structure and element constituency of the wires and the modified substrate surface[6, 55]. Furthermore, there remains disagreement on the physical cause of the distortion, whether it be Peierls, Fermi nesting, or phonon interaction[6].

Most, if not all, existing reports[6] of monatomic-wire CDW instabilities involve systems composed of heavy metal elements such as Au and In with completely filled *d*-shells and partially filled *s*- and *p*-orbitals. These limited examples raise a pressing question as to whether density-wave instabilities can occur in other generic material systems, particularly for light elements with partially filled *d*-orbitals, and if they can occur on substrates besides semiconducting surfaces.

Here we present low temperature scanning tunneling microscopy (LT-STM) observations of a dimerization (bond-centered density wave with a wavevector of $k = \frac{\pi}{a}$) instability of a Co atomic-wire system self-assembled on a vicinal Cu(111) substrate. Our

earlier studies[56] have shown that these monoatomic wires, formed at 300K, are precisely aligned along the Cu step edges; our STM measurements enable measurement of the chain geometry and atomic positions. Using *ab-initio* theoretical calculations we show that the partially filled *d*-shells, in fact, drive the instability. Further, in contrast to systems in previous 1-D experiments, the instability in Co atomic wires is found to be a consequence of strong local correlations on the 1-D-aligned Co atoms. The strong local correlations result in the *d*-shell of each Co ion being in a high-spin configuration; the combination of locally maximal spin and partial orbital filling leads to ferromagnetic correlations, which enhance the dimerization instability.

4.1. Experiment

The experiments reported here are based on our self-assembly-based growth procedure, described elsewhere[56, 57]. This procedure maximizes Co-wire nucleation at the Cu step edges, while minimizing Cu-terrace substitution by Co atoms, as well as any Co island formation; this result is evidenced by the sparse presence of Co atoms in/on the step terrace (Figure 4.4-Figure 4.6). Unlike the case of self-assembled chains on semiconducting substrates[6, 55], the location of the atomic chains in this bi-metallic system is unambiguous; as shown in the Supporting Discussion section, we are able to measure the position of the Co atoms precisely due in part to the contrast in density of states of the two metals. We refer the reader to the latter part of this chapter for an extensive amount of experimental measurements.

4.2. Results

An example of our LT-STM measurement of the self-assembled Co chains is shown in Figure 4.1e. This LT-STM instrument is designed for high-resolution microscopy, spectroscopy, and precise atom manipulation and shows very high stability and extremely low drift when operated at 5K. An instrument of the same type has recently been used for imaging organic molecules by non-contact atomic force microscopy in unprecedented detail[58]. Here, this stability was essential for making the precise lateral atom position measurements that are fully described in the Supplemental Material. The measurement shows two Cu step edges, visible as a corrugation of the background topography, along which Co atoms (visible as features above the background level) have arranged themselves to form a 1-D chain. At 5K, these chains do not consist of equally spaced Co atoms. A lateral distortion is clearly evident, indicating that the chain is dimerized. The typical measured 1-D unit cell width of 5.1Å matches well with twice the Cu-Cu atom spacing of the ideal Cu(111) substrate (2×2.56Å).

The measured Co-Co bond length of 2.0(±0.1)Å (see Supporting Discussion section, Figure 4.7) is noticeably shorter than the Cu-Cu atom spacing of 2.56Å, based on our STM measurements over a set of Co chains at 5K. By comparison, the Co-Co atom distance in self-assembled Co triangle islands on Cu(111) ranges from 2.50Å to 2.56Å[59], which is comparable to that found in bulk Co. It is surprising that the Co chain would exhibit a structural distortion; given that the atom spacing of bulk Co is similar to bulk Cu (a difference of only ~2%), an ideal uniform Co atom spacing would be expected. It therefore appears that the bond-length distortion in this case is due to the one-dimensional geometry along the Cu step edge with its anisotropic environment. Our observation of a dimerized Co

chain is also unexpected since monatomic Cu chains on Cu(111), which are fabricated using atom-tip manipulation, do not exhibit such a distortion[36]; these experimental results used STM measurements at 7K. Hence, the fact that we are using Co rather than Cu is important for the onset of this distortion.

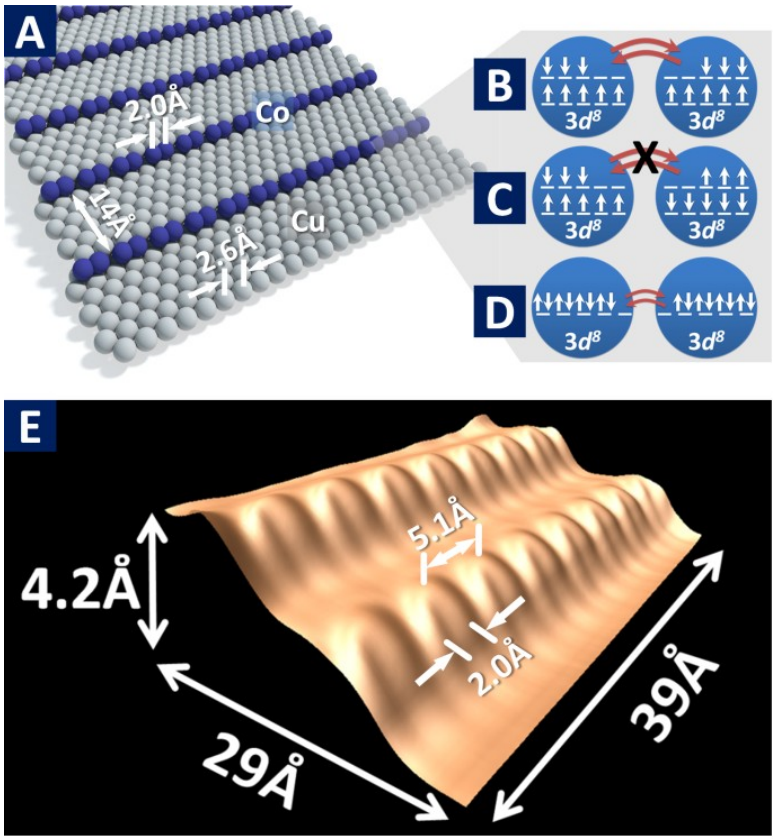

Figure 4.1 Self-Assembled Co atomic chain system. (a) Illustration of dimerized Co atomic chains on vicinal (8.5º miscut) Cu(111). (b)-(d) Illustration of high-spin ferromagnetic, high-spin anti-ferromagnetic, and zero-spin electron configurations. Coupling is strongest for the high spin ferromagnetic phase, weaker for the zero-spin phase, and blocked for the anti-ferromagnetic phase. (e) Perspective view of a STM topography of two self-assembled Co wires at adjacent Cu step edges. The vertical scale has been magnified to accentuate the appearance of the Co wires. The Co atoms constituting these wires have undergone a 1-D structural distortion, leading to the appearance of a single peak near the Cu step edge. However, the underlying Co atoms constituting each single peak are resolved farther away from the Cu step edge due to the decreased contribution of the Cu local density of states to the tunneling current. Constant current tunneling parameters: V_{bias} = +0.742V at 9.4nA.

One expects that the lattice distortion is a low-temperature phenomenon, occurring only below a critical temperature, as observed for wires on semiconducting surfaces. The bi-metallic Co/Cu(775) system investigated here undergoes a phase transition at relatively elevated temperatures. At a temperature of 91K, the Co distortion is non-uniform along a chain, varying from 0.6Å to 0.0Å. The Co chains also show a tip-bias dependency; at low tip bias, single Co atoms are easily resolved, while at higher tip bias, a ×2 periodicity is more prevalent (Figure 4.12, Figure 4.13). At a slightly lower temperature of 81(±4) K, however, some chains appear exactly like those measured at 5K, i.e. possess a dimerization instability that is independent of tip-bias (Figure 4.14). These observations indicate a coexistence of two different phases, lending to the tentative assignment of this system change as a 1st-order phase transition with a critical temperature in the vicinity of 100K.

4.3. Analysis

To understand the physics of the dimerization as observed in our experimental measurements, we examine theoretically how and why an isolated Co chain restricted to distortions in one spatial dimension dimerizes. The effect of the step may be subsequently deduced. *Ab initio* and density functional theory (DFT) calculations have previously been performed for free[60] and surface supported finite[61] and infinite atomic chains[62] with results ranging from non-dimerized to zig-zag to anisotropically strained. However, no clear physical mechanism has been deduced or put forward. Here we present DFT calculations, based on several different functionals (Figure 4.8, Figure 4.9)[57], which shed light on the physics underlying our experimental observations. Specifically, the energy of an infinite length 1-D periodic system consisting of two Co atoms per unit cell was studied

under the constraint that the period of the system matched twice the Cu atom-atom spacing (2 × 2.56Å) and that the Co atoms are allowed to move only along the wire direction. With regard to the latter constraint, note that our earlier *experimental* observations have shown the chain is in fact linear. In addition, our calculations used energy minimization to identify the final atom configuration. Finally, notice that in our experiment, the vicinal Cu(111) substrate template serves to align the atoms in the chain in a *linear* 1-D array.

In our theoretical model there are two Co-Co bond lengths. Figure 4.2a shows the dependence of the energy on the length of the shorter, i.e. nearest-neighbor, Co-Co bond (measured relative to the mean Co-Co distance). A clear energy minimum is visible at $\mathrm{d}_{short} = 0.794\ \mathrm{d}_{avg} = 2.03$Å (implying $\mathrm{d}_{long} = 3.08$Å). A key result of the DFT calculation is that the Co *d*-shell on each site is essentially fully spin polarized, having maximal spin polarization for given *d* occupancy. Different orientations of the Co spin were investigated (Figure 4.2a shows as an example the energy of the two sublattice antiferromagnet); the ground state was found to be in the *ferromagnetic* phase. Furthermore, the ferromagnetic phase favors a structural distortion while the antiferromagnetic phase does not. These finding suggest that the dimerization instability is driven by the energetics of electron transfer between *d*-orbitals subject to a ground state of maximal spin. Because the *d*-orbitals are partially occupied, transfer is optimized in a ferromagnetic state, while the high-spin state means that electron transfer is essentially forbidden in the antiferromagnetic state. These considerations suggest that the spin polarized *d*-orbitals play a key role in the dimerization phenomenon and thus spin (magnetic) interactions are key to our observations.

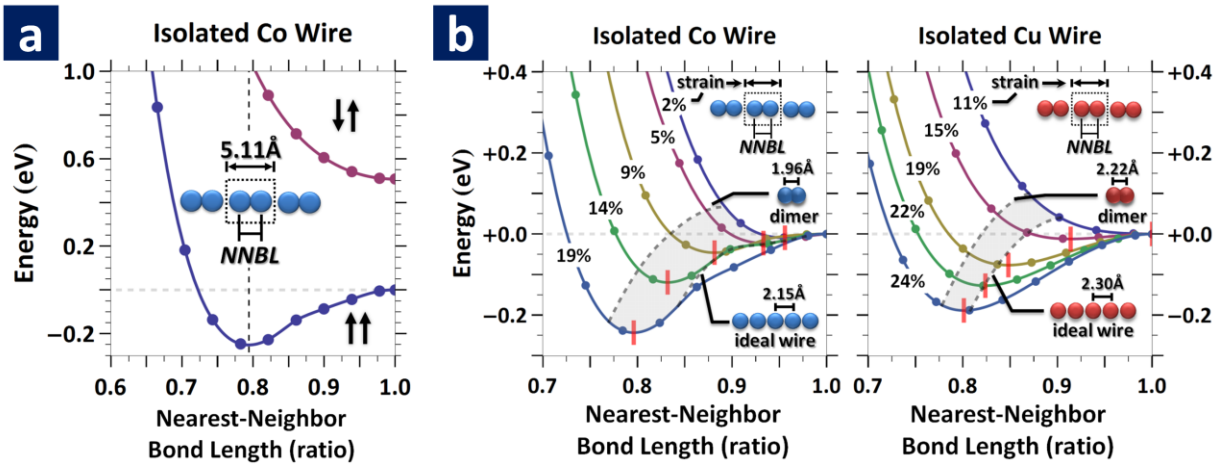

Figure 4.2 DFT energy-phase diagrams for atomic wires. Points denote actual calculated energies while smooth lines in between are 3rd-order interpolations. Total energies were calculated for a two-atom unit cell using DFT and the GGA functional (Figure 4.8,Figure 4.9). The lack of smoothness in some regions is due to varying degrees of orbital polarization (see supporting discussion). (a) Energy-phase diagram for Co atomic wire. The energies of the Co wires have been offset with respect to the *ferromagnetic* non-distorted case (NNBL=1.0); the horizontal dashed grey line denotes the reference. The nearest neighbor bond length is given as a ratio of the bulk Cu atom spacing (2.5561Å). (b) Energy of Co_2 and Cu_2 isolated wires measured relative to the energy of the undimerized wire and plotted against degree of dimerization (parametrized as ratio of short bond length to average bond length). Different curves indicate different strains (i.e. different unit cell lengths) relative to the unit cell length that minimizes the DFT energy of the wire. The energy of the Co wire has been computed for a ferromagnetic state; the Cu wire was computed for a non-spin polarized state (spin-polarized calculations converged to a zero-spin state). The left hand dashed grey line denotes the optimal bond length of the dimer (measured in units of one half of the mean unit cell length of the strained wires). The right hand grey line indicates the interatomic distance for the optimal non-distorted wire. The red vertical line segments mark the optimal nearest-neighbor bond length for each respective strained wire system.

To further investigate the relevance of the *d*- orbitals to the dimerization we compare in Figure 4.2b the dimerization energetics of stretched wires of Co (partially filled *d* shell; DFT predicts ferromagnetic ground state) and Cu (fully filled *d* shell; DFT predicts paramagnetic ground state) wires. On general grounds, we expect that a physical 1-D system that is stretched to have a mean bond length sufficiently far from its ideal bond-length spacing will undergo a distortion. However, both the extent of the strain required for

dimerization and the amplitude of the distortion will depend on the physics responsible for the instability. In the two panels of Figure 4.2b we plot the energy (relative the energy of the undimerized state) vs degree of dimerization, for different amounts of strain relative to the bond length which minimizes the DFT energy for the undimerized wire. We see that in the Co system the dimerization becomes favored at a much lower strain than in the Cu system, and the energy gain from dimerization is much greater for equal amounts of strain. We also compare the optimal length of the short bond (indicated by red vertical line) to the optimal spacing of the transition metal dimer (leftmost grey dashed line) and to the optimal atom-atom distance in the unstrained wire (rightmost grey dashed line). For a strained Co wire, the nearest-neighbor bond length generally lies between the optimal dimer bond length and the optimal non-distorted wire bond length, indicating that dimerization is truly favored. By contrast, in the case of a strained Cu wire, the nearest-neighbor bond length is generally greater than, but close to, the optimal non-distorted wire bond length (at least for strains up to ~22%).

This comparison of Co and Cu atom wires highlights the difference in tendency to dimerization in a partially filled *d*-orbital derived band 1-D system vs a partially filled *sp*-orbital derived band 1-D system. To further probe the physics of the dimerization, we note that the absence of the dimerization in the antiferromagnetic state indicates that the dimerization is connected to hopping of *d*-electrons (suppressed in the AF state by the condition that each Co ion is in a high-spin configuration). The total *d* occupancy is approximately d^8. Choosing an angular-momentum quantization axis (z-direction) parallel to the chain direction we note that the $3d_{xy}$ and $3d_{x^2-y^2}$ orbital do not hybridize much along the chain and instead act as local moments (Figure 4.10). The physics is driven by the

$3d_{xz}$, $3d_{yz}$ and $3d_{z^2}$ orbitals. In the spin-polarized state, the majority orbitals are filled while the minority orbitals are nearly ½ filled. In this circumstance, a dimerization instability leads to a large energy gain, which arises because in each orbital there is one minority spin electron per pair of atoms; this electron forms a strong bond in the dimerized state, with the antibonding orbital completely empty. This result can be viewed as a Peierls distortion. Note that if the ground state was not high spin, the band energetics would be less favorable to dimerization because one would have partially, not fully occupied bonds. The dimerization instability is also favored by the relatively localized nature of the *d*-electrons which, in contrast to the more spatially extended *s*-*p* electrons, have predominately a nearest neighbor hopping, and which moreover rises rapidly as the inter-atom distance is decreased.

The above physical explanation is only reasonable if the hybridization of the Co *d*-states to the electrons in the vicinal Cu substrate is relatively weak. This hypothesis is consistent with the observation of weak indirect spin exchange interaction for Co dimers on Au(111) and Cu(100) substrates[63, 64]. These studies found that although there exists a strong indirect exchange for a Co monomer by way of the Kondo effect (indicating the presence of a moment, i.e. a locally high spin configuration, on the Co site), a Kondo signal was lacking for a Co dimer that was fabricated by STM atom-tip manipulation. The lack of a Kondo signal for the dimer is naturally understood in terms of the non-negligible *d*-*d* electron transfer suggested here. Note however that the substrate is important in our 1D system, in that, as mentioned above, it provides strain and linearly aligns the Co atoms; both of these effects are seen in our STM data.

In order to further elucidate the substrate/Co chain interactions, we have also performed LDA and GGA calculations for a Co chain *on a Cu step*. We find that, within DFT, bonding of the chain to the stepped substrate eliminates the dimerization. Note that our DFT procedure was first tested on a standard Cu(111) substrate and found to yield the expected Cu electronic structure. We attribute the lack of Co dimerization to the fact that DFT is unable to accurately capture the detailed physics. It is likely that this failure occurs because DFT overestimates the hybridization between the chain and the substrate; we are currently working to understand the DFT failure more clearly. We note that our result does not affect the mechanism we introduce to understand the dimerization, which, as discussed above, is consistent with other spin/substrate interactions.

4.4. Analysis ramifications and applications

One important feature of our experimental chains is best seen in the spin behavior within our chains; thus we first examine the spin properties and then explore the consequences of this behavior for a magnetic memory. An important consequence of the bond-length distortion is a strongly decreased electron transfer between neighboring 2-Co-atom unit cells, implying also that the coupling of spin between dimers becomes negligible. In order to quantify this, we perform a cluster expansion of the total energy in terms of the spin cluster functions. Given a lattice model with a binary-site variable (i.e. up/down spin), one can perform a power-series expansion of any average lattice observable in terms of the correlation functions of the site variables. In spin systems, one can often obtain a highly accurate expansion using only pair terms over a short range. We find that one can

accurately represent the energetics using only neighbor-pair terms, as defined in the following equation:

$$H = E_0 + \sum_i J_1 s_i \cdot s_{i+1} + J_2 s_{i+1} \cdot s_{i+2}$$

where E_0 is the non-magnetic energy contribution, s is ±1, and J_1/J_2 are the neighbor magnetic pair interactions (Figure 4.3a, Figure 4.11a)[57]. The goal of using this basic model is to show the change in these parameters as a function of distortion. In Figure 4.3b, a plot of the parameters is shown (Figure 4.11). Note that in the undistorted wire the

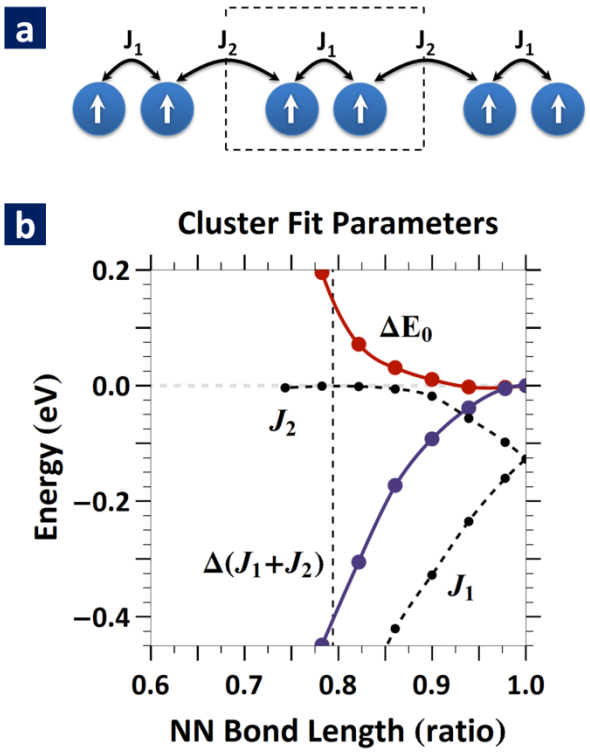

Figure 4.3 Fitting to a cluster expansion model. (a) Cluster expansion model illustration of the Co 2-atom unit cell. J_1 denotes the nearest-neighbor or *intra*-pair interaction while J_2 denotes the *inter*-pair interaction. The unit cell is delineated by the dashed rectangle outline. (b) Cluster expansion model parameter fits for the Co atom wire for different amounts of distortion. E_0 is the non-magnetic energy contribution. The vertical dashed line denotes the optimal Co wire distortion. Note that J_2 is quite negligible at the optimal distortion length. Energies were computed using spin polarized GGA (Figure 4.11).

magnetic interaction constants are equal by symmetry, with the negative sign arising because DFT favors a ferromagnetic state. As the system is distorted, J_1 increases rapidly in magnitude whereas J_2 goes quickly to zero. We also present the sum of the magnetic-interaction parameters (J_1+J_2), which gives the total magnetic contribution to the energy. The monotonic decrease of the sum (J_1+J_2) as distortion is increased also shows that the ferromagnetic state strongly favors the distortion, as expected if the driving force is electron transfer between high-spin configuration *d* states. Note that E_0 is monotonically increasing; this illustrates that non-magnetic terms do not play a role in the dimerization.

The striking difference in the variation of the magnetic-interaction parameters, J_1 and J_2, under dimerization suggests that the spin chain may provide an interesting realization of a memory device. In the dimerized state, J_2 is negligible compared to the quite large magnetic coupling, J_1, between nearest-neighbors. A consequence of this result is that while each dimer is itself in a high spin state, the spins of neighboring dimers may take arbitrary orientations with negligible energy penalty. Hence, a dimerized Co spin-chain can potentially behave as a linear array of spin memory bits. Binary memory requires a bistability, in other words an easy axis for the magnetization of a dimer. We expect that this is provided by the Cu step edge, as was shown for a Co/Pt(997) system[65]. A somewhat similar system, but based on antiferromagnetic switching, has been recently realized using Fe on Cu_2N[66]. Finally, we note that even though the Co chain unit cells may be "spin-isolated", they are not electronically disjoint; an energy band diagram of the Co chain reveals band crossings (predominately of d_{z^2} and *s* character) at the Fermi energy (Figure 4.10), suggesting a possibility for manipulating the spin states via appropriately applied currents[67].

Our experimental results and the CDW phenomena seen here also have implication to the field of suspended atomic chains formed by break-junctions[68]. While it has been found that suspended non-magnetic wires can be formed by this method, forming suspended magnetic wires has not yet been successful[69]. The reasoning for this was reported to be softening of the binding energy of the atomic chain due to magnetism[69]. While the process of forming a suspended chain is complicated[70], the results reported here suggest that forming a suspended Co atomic chain is difficult, in part, due to the tendency for the chain to dimerize. The long bond would be weakened due to the extent of the dimerization occurring during stretching of the chain (Figure 4.2b).

4.5. Conclusion

Thus both our experimental and theoretical results show a Co-atomic wire on stepped Cu(111) behaves as a 1-D atomic system with a low-temperature spin-exchange-induced dimerization instability. This work raises the question as to whether other light partially filled *d*-orbital 1-D systems will exhibit a similar instability once realized in experiment, and their possible technological applications.

4.6. Methods

Self-assembly of Co chains on Cu(775) was carried out in a UHV preparation chamber with a base pressure in the low 10^{-10} Torr range. Subsequent to cleaning the vicinal substrate by several sputter-D_2-anneal cycles, deposition of Co atoms by e-beam heating of a Co rod was performed at 130K using a slow deposition rate of 0.01ML/min. The deposition was followed by a brief increase in the sample temperature to ~RT to allow

the Co atoms to migrate to the step edges and anneal any defects. Subsequently the sample was *in-situ* transferred to the STM mounting and then cooled to the experimental temperature (typically 5K). The tunneling microscopy measurements used a chemically etched tungsten tip. All measurements were performed at the Center for Functional Nanomaterials (CFN) LT-STM facility at Brookhaven National Lab. STM topography data was smoothed using a Gaussian filter in order to remove noise derived artifacts. Some of the 3-D topography images were generated using WSXM[71].

It is possible to resolve the Co chains more clearly from the STM topographical measurements by use of a technique akin to background subtraction. In this case, the component subtracted away from the STM measurement is the vicinal Cu topography. The technique is illustrated in Figure 4.5.

Density functional theory (DFT) calculations were performed both at Columbia University and on the computational cluster of the CFN, using the Vienna *Ab-Initio* Simulation Package (VASP) with a plane-wave basis and the projector augmented wave (PAW) method[72, 73]. Different functionals, the local spin density approximation (LSDA) functional, and two types of spin polarized generalized gradient approximation (GGA) functionals, Perdew-Wang (PW91)[74] and Perdew-Burke-Ernzerhof (PBE)[75], were utilized to asses commonality between their respective results. Calculations typically used 30 or more *k*-points, and periodic slabs were at least 10Å in width and height.

The electronic structure for a system calculated under density functional theory may be deduced if one assumes equivalence with the calculated Kohn-Sham eigenvalues. The band energy diagram and density of states for a ferromagnetic spin phase, computed using a GGA functional, is shown in Figure 4.10. Cluster expansion fit parameters were

computed using 4 distinct spin configurations of a 4-atom unit cell and fit by a least squares method (Figure 4.11).

4.7. Supporting Discussion

Determining and quantifying the dimerization of the Co chains

Because STM topography measurements have been shown to sometimes be bias dependent, due to tunneling into energy-dependent local density of states (LDOS)[6], the excitation of charge-density modulations[76], or inelastic electron tunneling[77], STM measurements on these chains were repeated at different tip biases ranging broadly from -2V to +2V. These measurements did not show a change in the dimerized appearance of the chains. Another possible source for the non-ideal appearance of the chains is the condition of the tip itself. To rule this out, controlled tip crashes were performed, followed by re-imaging of the chains. Again, no change in the distorted appearance of the chains was found, though a change in the apparent height of the Co atoms was observed. Hence, we conclude that the dimerization instability of the Co chains on the Cu(775) substrate at 5K to be a true structural distortion rather than a bias- or tip-induced electronic effect.

We used STM-derived topography measurements of Co chains to determine the bond-length variation along the chain. The magnitude of the distortion gives insight into the extent and strength of the structural instability and allows for direct comparison to *ab-initio* calculations. An example is shown in **Figure 4.7**. Ideally, the bond-length of two Co atoms constituting the doubled unit cell would be determined by the distance between the local maxima present in the topographical profile irrespective of the profile-line location. However, as can be seen from **Figure 4.1**e, the topography profile of the dimerized Co chain

depends on the distance from the step edge. For example, we observe blurring (i.e. coalescing of the Co atom peaks) at the Cu step edge. Similarly, for the case of a single isolated Co dimer, the blurring of the LDOS in a STM topography measurement prevented differentiating the Co atoms that make up the dimer[78]. We therefore employ a more systematic procedure. We present in **Figure 4.7**a line profiles along the wire direction, equidistant from each other and in which the planar cuts are perpendicular to the step terrace, i.e. the (111) plane. The line profiles show a double peak structure that is resolved slightly away from the Cu step edge, as denoted by the length bars. To arrive at the distortion in the Co-Co bond length, the average peak-to-peak (P-P) spacing per profile line was determined and plotted with respect to the average vertical distance of the peaks from the top of the Co wire (the distance from the top of the Co wire was normalized to the apparent Co wire height, which, for this particular example, was approximately equal to the Cu step height of 2.09Å); see **Figure 4.7**b. Note that the distance from the top of the wire is proportional to the distance away from the Cu step edge. Hence, the P-P spacing depends on distance from the step edge. The P-P plot **Figure 4.7**b shows that there is a significant height interval over which a near constant separation between Co atoms within each unit cell is observed. We determine the Co-Co bond length from the spacing in this interval. This means that the bond-length determination is made away from the *Cu* step edge, since in this region the Co atom STM resolution is obscured by coalescing of the Co atom peaks, but not too far from the step edge (where the amplitude of the variation becomes small and the measurement is complicated by other effects), as indicated in Fig **Figure 4.7**c. Our measurement shows that the shorter of the two Co-Co bond lengths (i.e. the nearest-neighbor bond length) is 2.0Å (0.1).

Interaction of Co chain with a weakly bound impurity

The interaction of the Co chain with an unidentified impurity was captured by LT-STM, as shown in Figure 4.6. H_2 and CO are the most common background gases under UHV[79]. Furthermore, it is known that CO preferentially binds to Co but not to Cu[23]. Therefore, we presume the identity of the impurity to be CO.

Co wire STM tip-bias dependent topography present above $T_{Dimerization}$

Besides a lack of uniform nearest-neighbor bond-length, the Co wire phase for $T>T_{Dimerization}$ is distinctly different from that of the dimerization instability phase in that the topography is tip-bias dependent (Figure 4.12), indicative of a change in electronic structure. The Co wire nearest-neighbor bond-length modulation is also not necessarily 1-D; at a tip bias of ±500mV, a Co chain exhibits a zig-zag topography. To further compare the modulations of a chain under different tip biases, plots of the profile cut along the chain in Figure 4.12 are shown in Figure 4.13. Profile line position was taken at peak maximums; unlike the dimerization instability phase, the individual Co atoms do not coalesce together, but rather are resolved at their local maximum. The profiles for occupied and unoccupied states appear relatively similar at a fixed magnitude of tip bias (e.g. ± 100mV, ± 300mV); this is true for a tip bias magnitude of up to at least 500mV. On the other hand, a comparison of line profiles between different tip biases reveals variation in phase shift and amplitude. Due to the finite length of the chain, a Freidel-like oscillation is observed, and has a wavelength of ~25Å. Although $T>T_{Dimerization}$, the chain profile also shows evidence of 2× modulation, particularly at high tip bias and for atoms in the vicinity of the chain's termination.

Orbital polarization of a Co wire in DFT and GGA

We found that DFT using the GGA functional predicts orbital polarization of the $3d_{xy}$ and $3d_{x^2-y^2}$ orbitals (Figure 4.10a) as the lowest ground state of the undistorted Co wire. The degree of orbital polarization decreases with increasing distortion (decreasing nearest-neighbor bond length, Figure 4.10c). The presence of orbital polarization is the reason for the non-smooth energy phase plots for a Co wire. For completeness, non-orbital polarized energy phase plots are made available in Figure 4.8 and Figure 4.9.

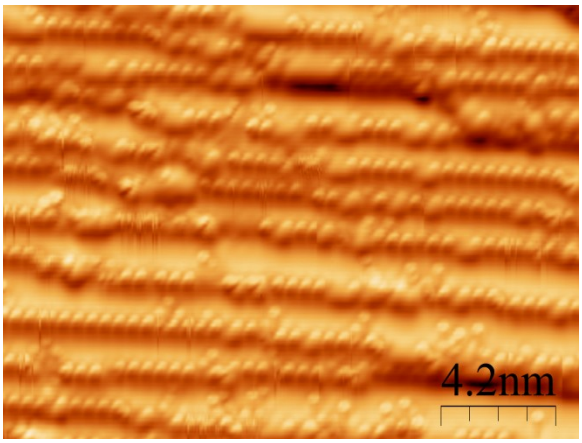

Figure 4.4 Co atomic chain self-assembly. STM image of self-assembled atomic Co chains (visible as linear arrays of approximately spherical dots) on the 14Å average-width terraces of Cu(775) measured at T = 5K. A derivative ($\partial z/\partial y$) filter was applied to accentuate the appearance of the Co decorated step edges. The Co coverage is ~0.14ML. At 5K, the single-atom wide Co chains along the step edge are found to undergo a dimerization distortion along the chain direction. Hence, the sphere like objects are not single Co atoms but rather pairs of Co atoms with separation 22% smaller than the underlying Cu atom spacing. The different appearance of some of the Co atom pairs is due to adsorption of impurity molecules, presumed to be CO (see supporting discussion, Figure 4.6). Constant current tunneling parameters: V_{bias} = +2.08V at 9.4nA.

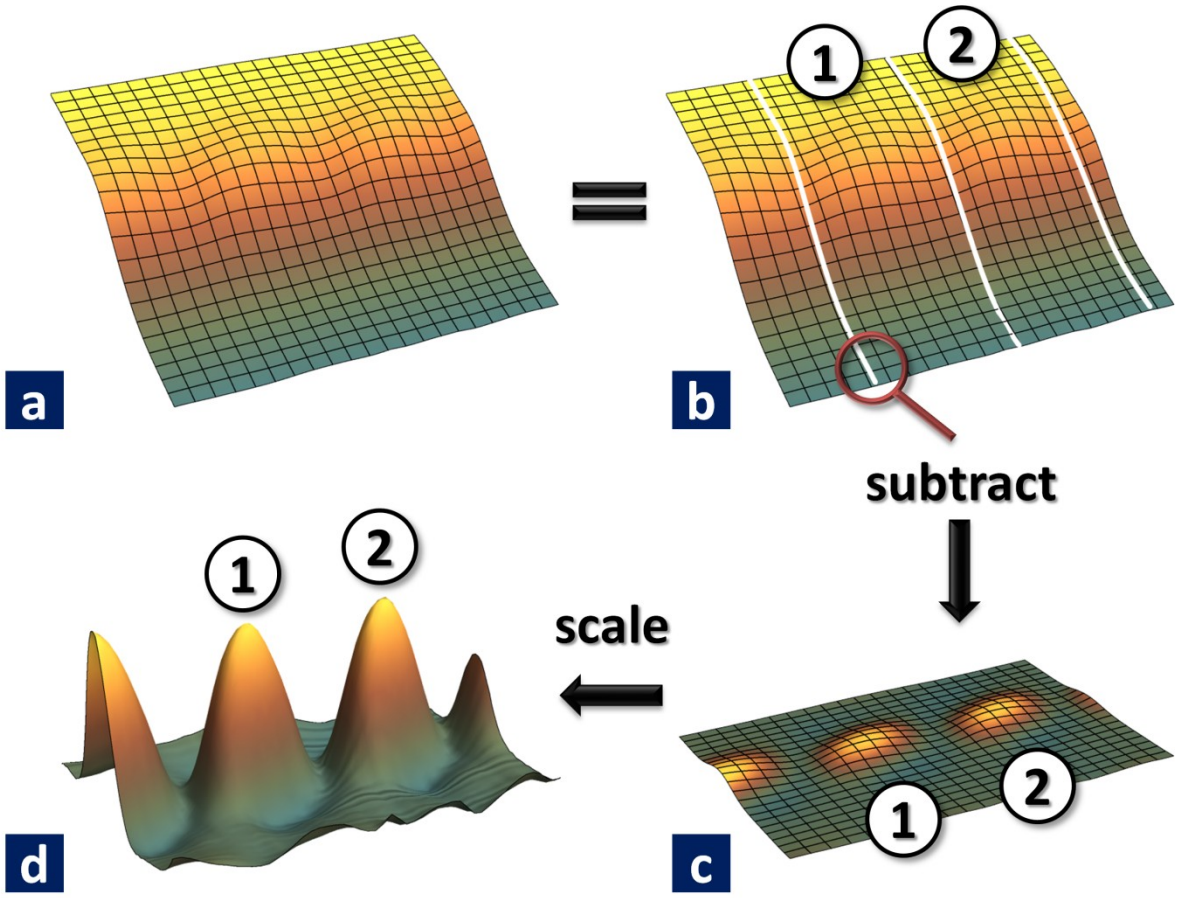

Figure 4.5 Delineation of Co atoms by subtraction of Cu step. (a) STM image of a Co dimerized chain self-assembled at a Cu step edge. The location of the Co atoms can be inferred from the grid lines superimposed on the topography. (b) The same topography as in (a) but with the ×2 distortion boundary denoted by white lines. Within each boundary are a pair of Co atoms; two of these pairs have been marked as 1 and 2. The profiles defined by the white lines approximate the profile of a clean Cu step edge. One of these lines, as indicated by the red circle, has been used for the subsequent subtraction step, which produces the topography shown in (c). (c) Subtracting the aforementioned profile line produces a relatively flat plane with protrusions belonging to the Co-*pair* LDOS. This derived topography can then be vertically scaled to more clearly visualize the Co dimerized chain (d).

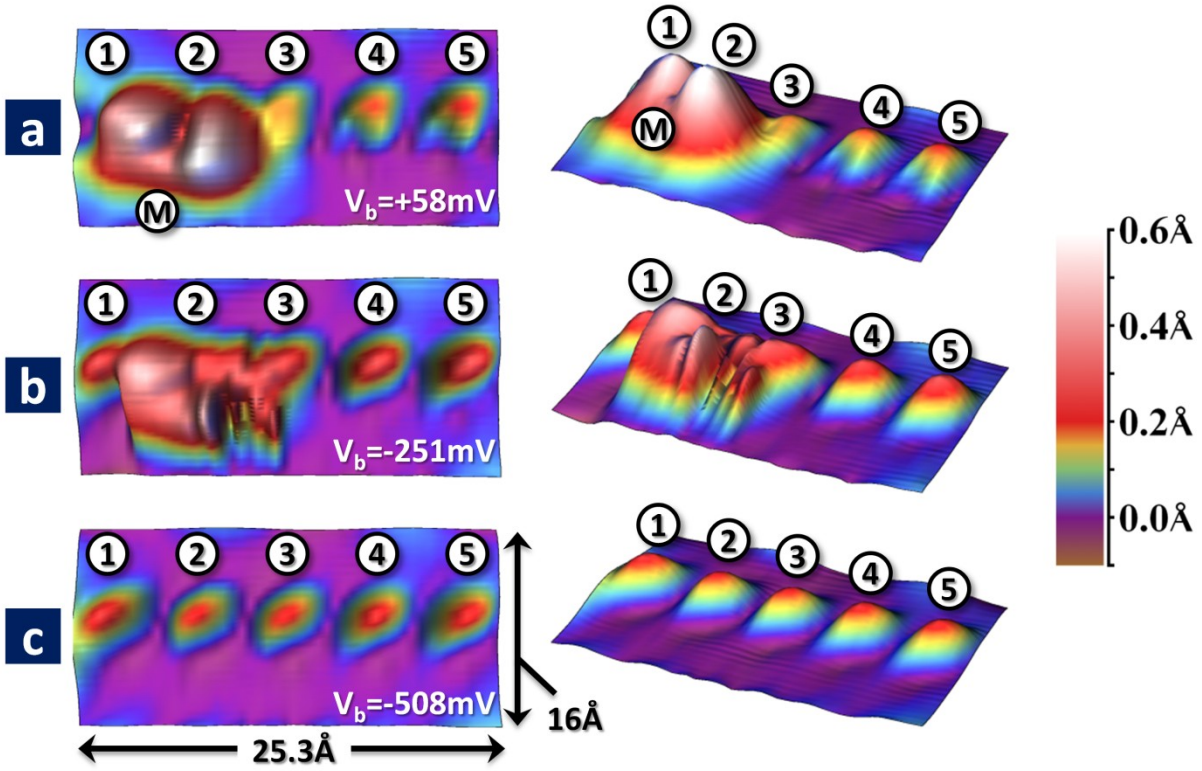

Figure 4.6 Interaction of an impurity with a self-assembled Co dimerized chain. Although the identity of the impurity is unknown, it is guessed to be a CO molecule. The topography images shown here were derived by subtracting the Cu step, as per Figure 4.5. (a) An STM topography of a Co dimerized chain, of which 5 Co pairs are visible. In addition, an impurity (labeled M), located in the neighborhood of Co pair 1 and Co pair 2, is also present. The electronic effect of the impurity is to increase the LDOS around Co pairs 1 and 2, as evidenced by the increase in their apparent height. (b) At a higher bias of -0.25V, the tip is able to dislodge the impurity. This is observed in the changing topography, in which scan lines run perpendicular to the chain, from right to left (i.e. from Co-pair 5 to Co-pair 1). After the impurity is dislodged, Co-pair 1 appears with the same contrast as Co pairs 4 and 5. (c) The same chain, after dislodging of the impurity, showing the recovery of the uniform LDOS dimerization for each Co pair. The ability to easily dislodge the impurity using a relatively average tip bias indicates a weakly bound entity to both the Co chain as well as the underlying Cu substrate; in conjunction with the observation of a small apparent volume, these measurements support the identity presupposition of a small molecule such as CO. This observation also shows the relative inactivity (i.e. lack of strong hybridization) of the Co chain with the impurity.

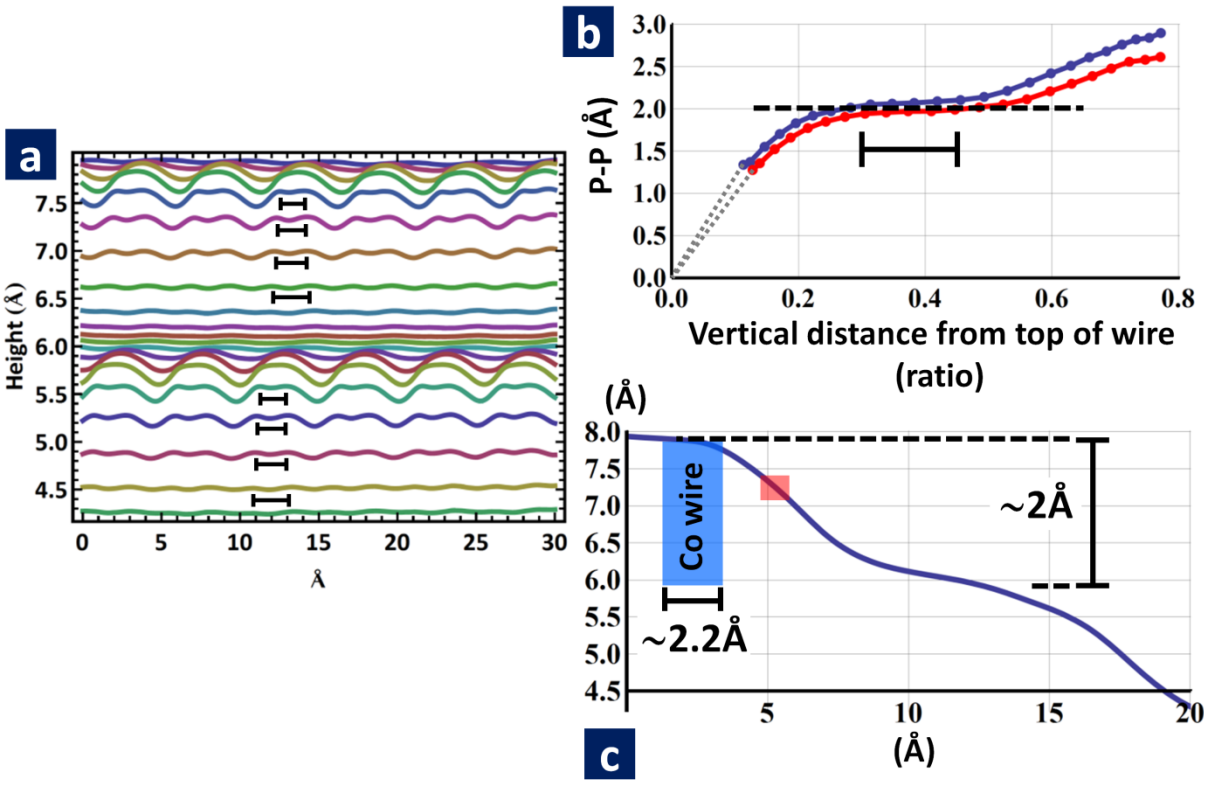

Figure 4.7 Measurement and analysis of the Co bond length structural distortion at 5K. Plots are based on STM measurement shown in Figure 4.1e. (a) Height profiles along the Co wire direction, obtained at a series of equally spaced points away from the step edge. Bars are guides to the eye indicating spacing of Co atoms in a dimer. (b) The peak-to-peak (P-P) spacing varies with vertical distance from the top of the Co wire, as shown for the two Co wires by different color curves. The vertical distance from the top of the wire was normalized to the apparent wire height, which, for this particular example, was approximately equal to the Cu step height of 2.09Å. (c) A profile cut perpendicular to the step edge reveals a smooth outline due to the finite radius of the tip and the relatively narrow terrace width. The blue shaded region is a guide to the eye for the approximate position of the Co wire, while the red shaded rectangle corresponds to the region of constant P-P length, denoted in (b) by a bar.

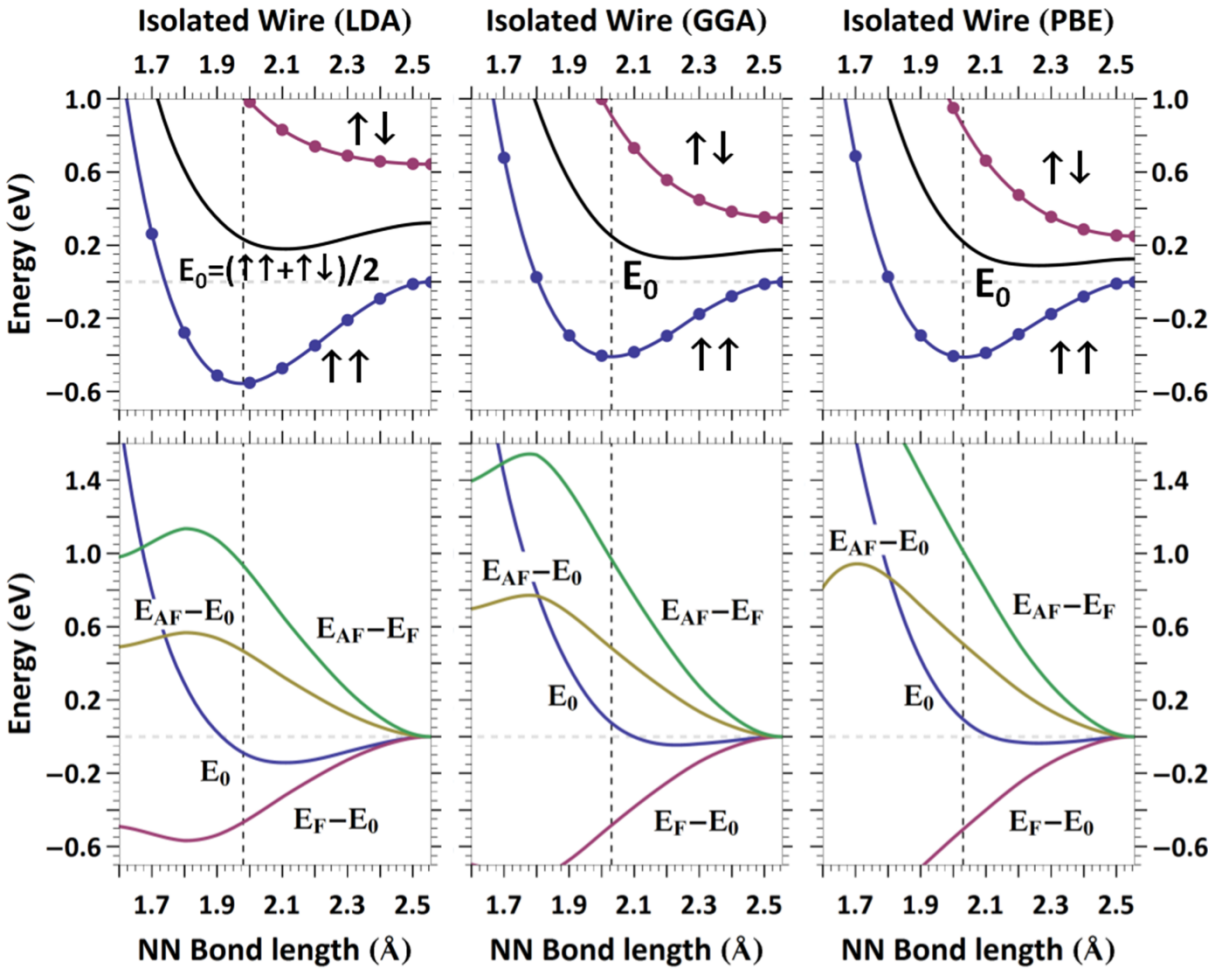

Figure 4.8 Co wire distortion phase energies using different DFT functional (*without orbital polarization*)**.** The top row shows the Co wire energy for different nearest-neighbor distortions; the right vertical axis (2.5561Å) is the case of zero distortion. The energies are referenced to the undistorted ferromagnetic phase. The unit cell size is equal to 2 × Cu atom spacing (2 × 2.5561Å = 5.1122Å). E_0 is the average of the ferromagnetic and anti-ferromagnetic phase energies. The points are the actual computed energies, while the smooth lines are 3rd-order interpolations. The bottom row shows the change in energy for different combinations of E_F, E_{AF}, and E_0; each combination is referenced to its respective value of the undistorted wire case. The optimal nearest neighbor bond length (d_{short}), denoted by the vertical dashed line, is 1.98Å using LDA, and 2.03Å using GGA or PBE.

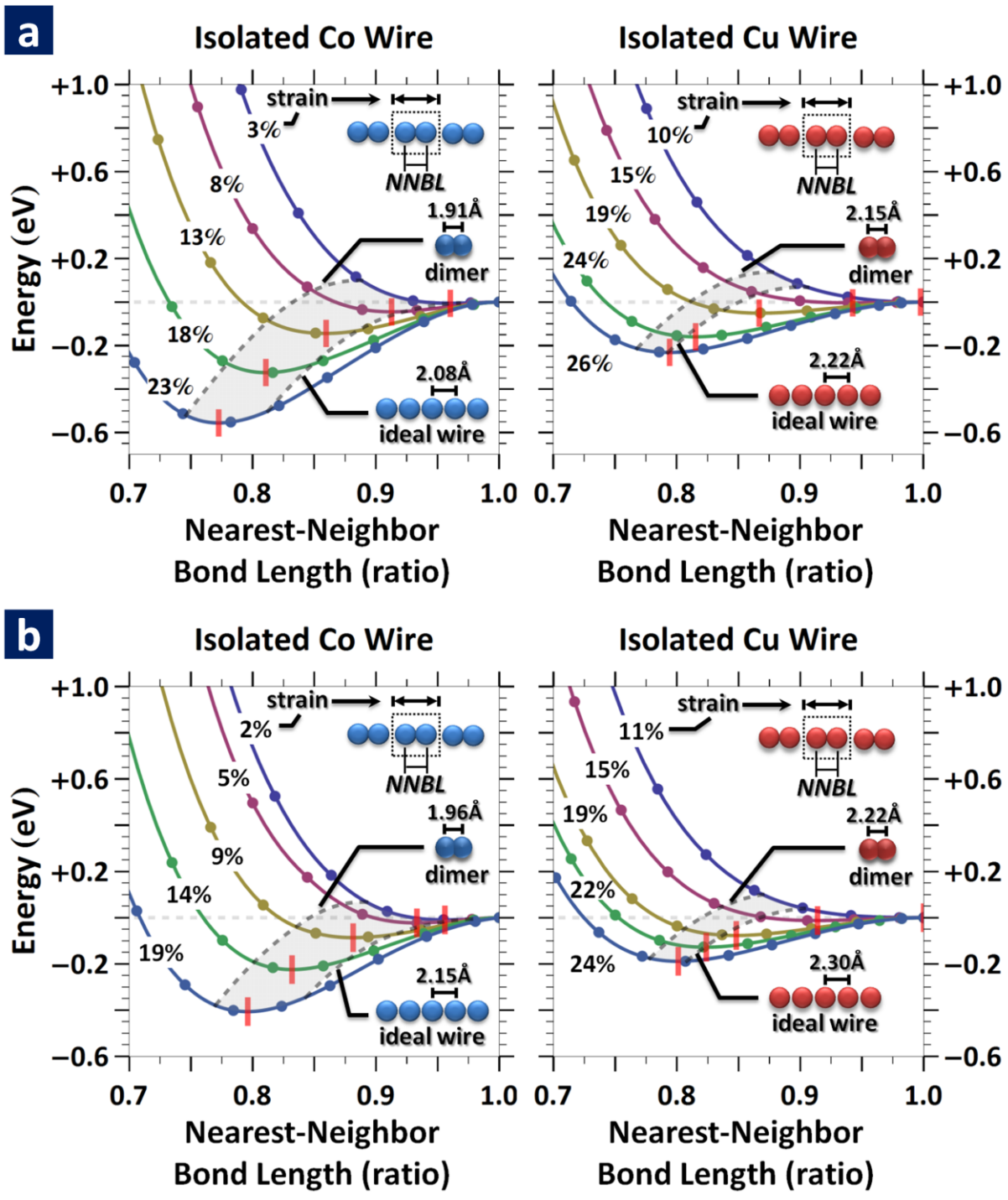

Figure 4.9 LDA (a) and non-orbital polarized GGA (b) DFT functional version of Figure 4.2b.

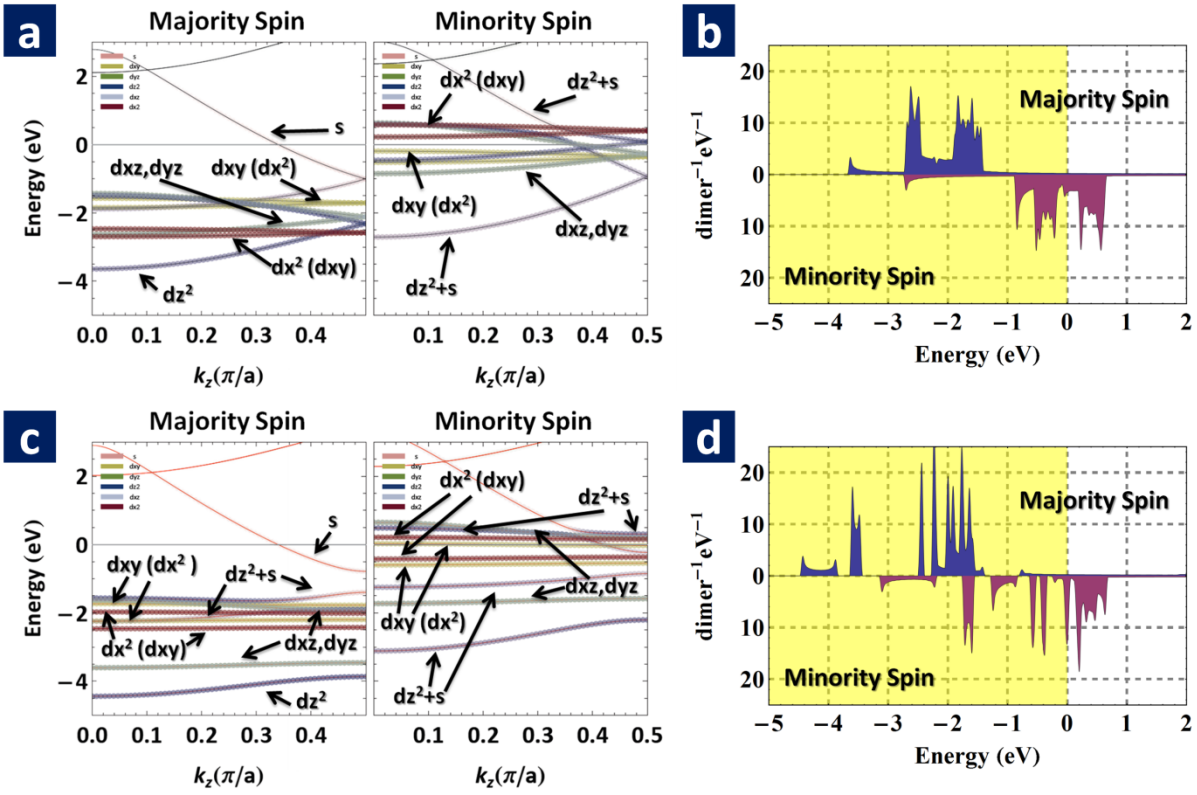

Figure 4.10 Electronic structure of isolated Co wires constrained to bulk Cu atom spacing (2.5561Å × 2 unit cell). Plots (a) and (b) correspond to the non-distorted wire while (c) and (d) correspond to the optimally dimerized case. The z-axis is parallel to the wire. (a), (c) Band energy diagram for majority and minority spin. The d_{xz}, d_{yz} orbital derived bands are degenerate, as expected by symmetry. Also, by symmetry, the d_{z^2} and s orbital derived bands are hybridized; the amount of hybridization in each band, however, is not always uniform across a band or across spin populations. The d_{xy}, $d_{x^2-y^2}$ orbitals are lifted out of degeneracy due to orbital polarization. Note that overall, the dimerized Co wire is not an insulator; an s/d_{z^2} orbital derived band crosses the Fermi level for both majority and minority spin. (b), (d) The corresponding density of states. Computed using spin polarized GGA.

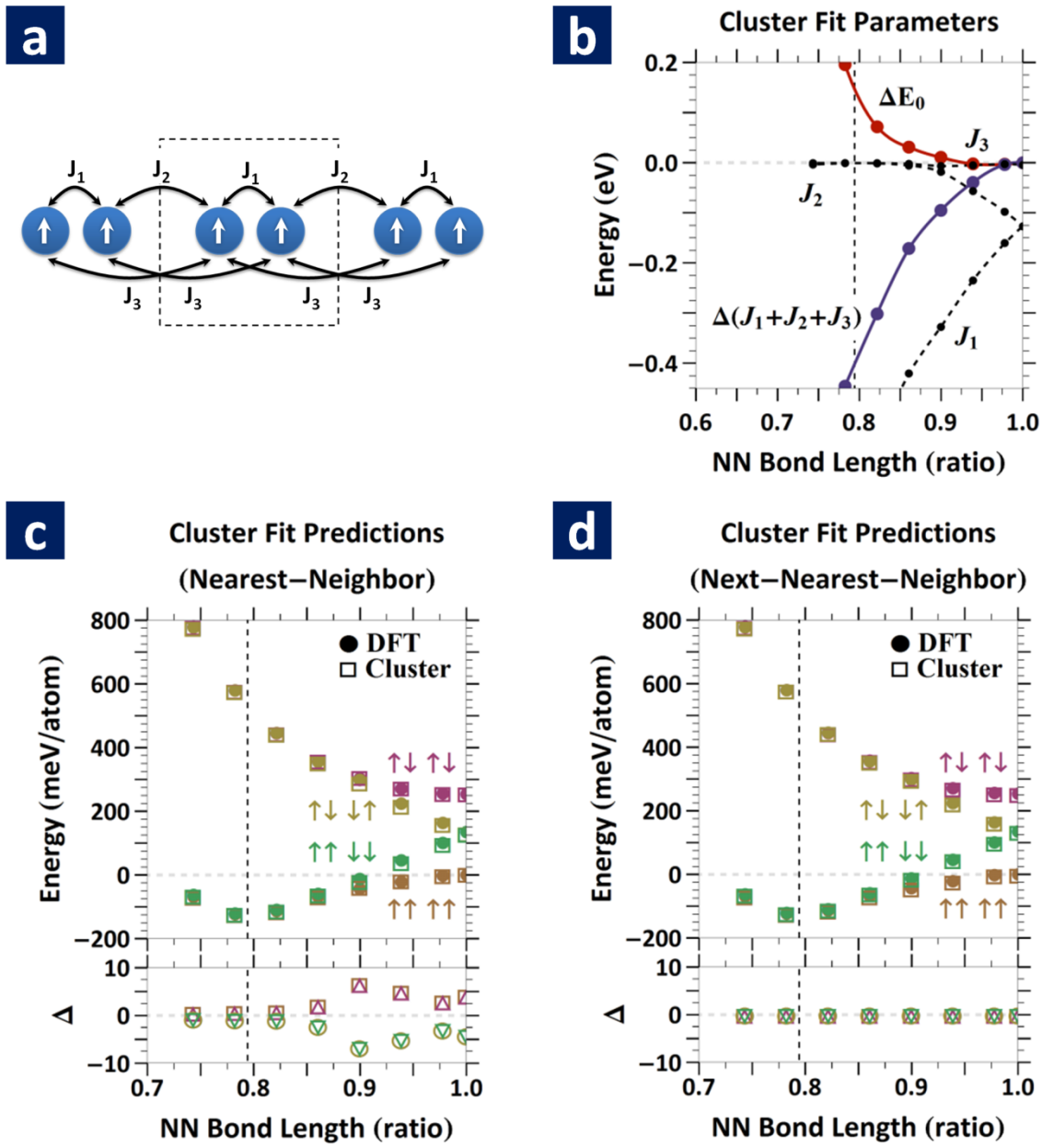

Figure 4.11 Cluster fit expansion comparison and errors. To quantize how well the cluster expansion fits the DFT calculations, we plot the error between DFT and the cluster expansion for both nearest-neighbor (J_1 and J_2 only) and next-nearest-neighbor (J_1, J_2 and J_3). (a) Illustration of next-nearest-neighbor model. (b) Plot of cluster fit parameters with respect to the short bond length. (c) Energy comparison plot between DFT and nearest-neighbor cluster expansion. The unit cell used for the comparison consisted of 4 atoms, and 4 distinctly different spin configurations were utilized. The error is plotted underneath, with symbol colors corresponding to the respective spin configurations. Note that the error is relatively smaller at the optimal short bond length. (d) Same as (c) but for a next-nearest-neighbor expansion. Energies were computed using spin polarized GGA.

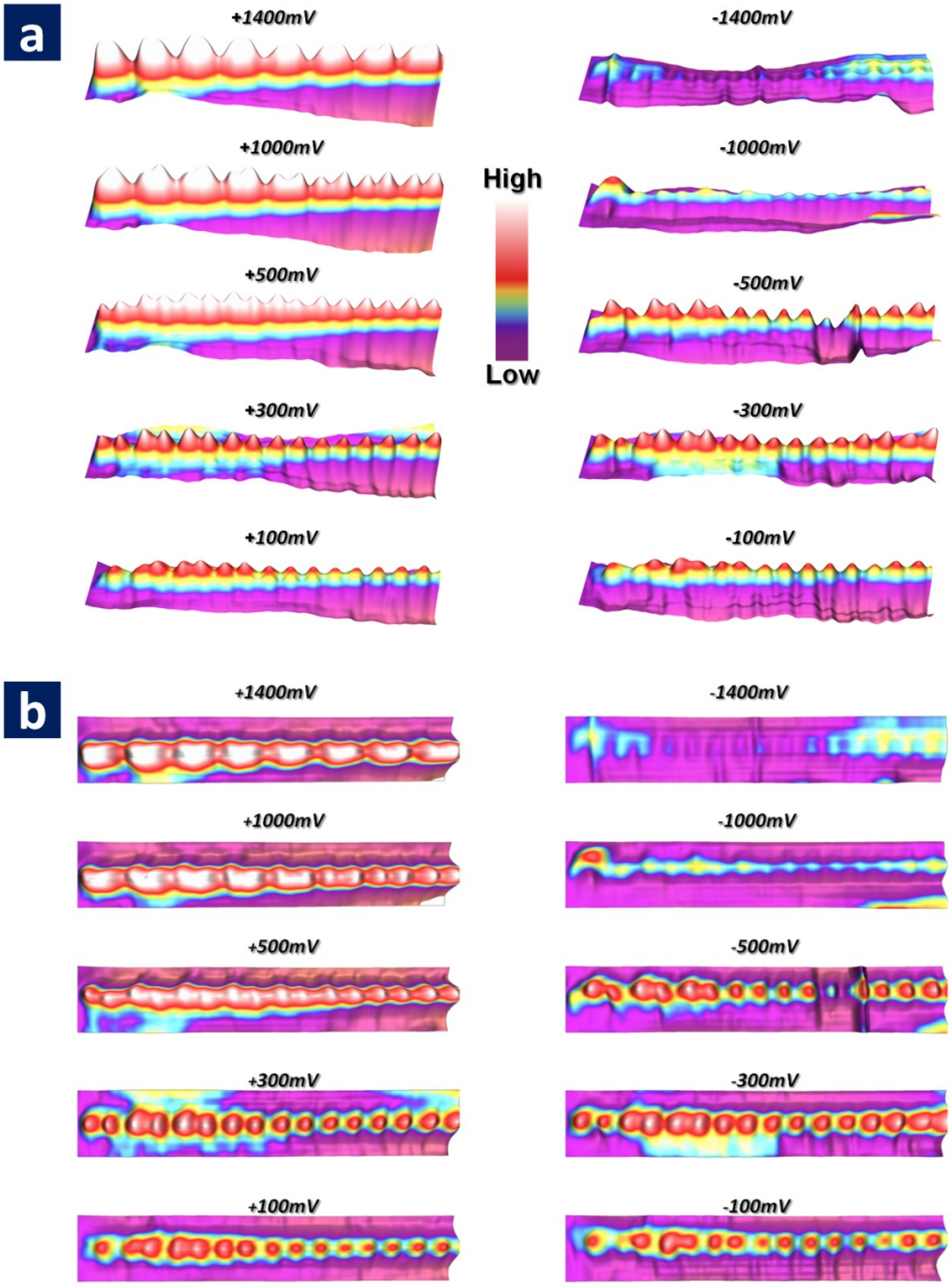

Figure 4.12 STM topography of Co wires at 91K. The technique of substrate subtraction, as described in Figure 4.5, was employed in producing these images. This higher temperature phase shows tip-bias dependency, in contrast with the dimerization instability phase present at lower temperatures. (a) and (b) are front and top views, respectively. Note that the chain modulation is not only parallel to the chain, but can appear perpendicular to it; for instance, at ±500mV, the chain appears to have a zig-zag topography. The discontinuity in the topography at −500mV is due to a tip change.

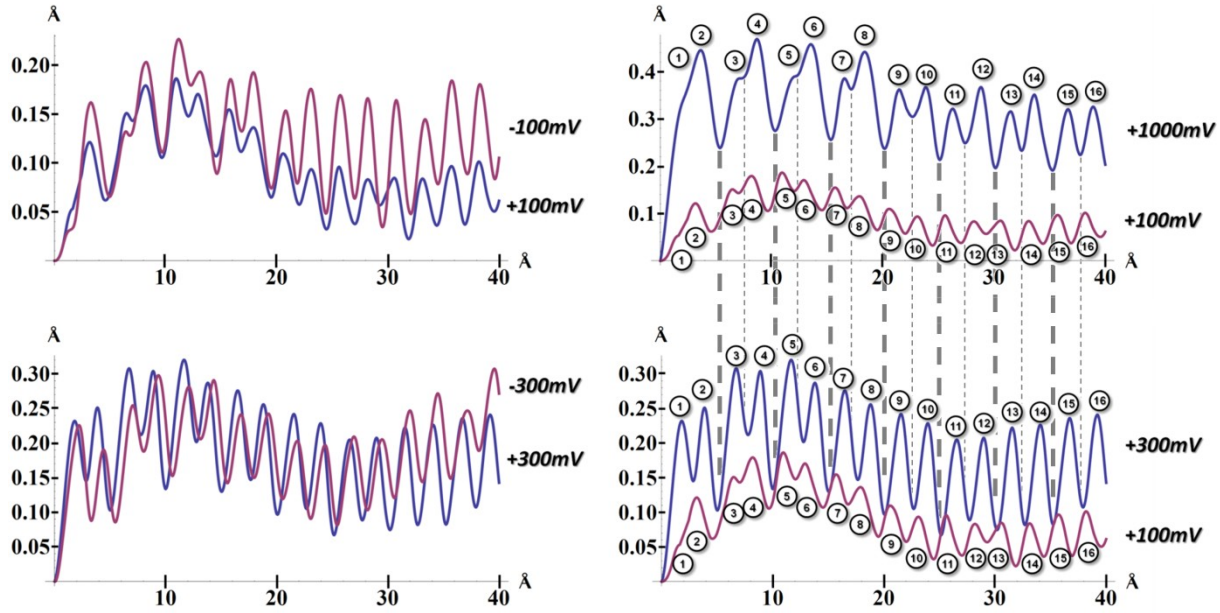

Figure 4.13 Line profiles along Co chain of Figure 4.12**.** Profile line position was taken at peak maximums; unlike the dimerization instability phase, the individual Co atoms do not coalesce together, but rather are resolved at their local maximum. The profiles for occupied and unoccupied states appear relatively similar at a fixed magnitude of tip bias (e.g. ± 100mV, ± 300mV); this is true for a tip bias magnitude of up to at least 500mV. On the other hand, a comparison of line profiles between different tip biases reveals variation in phase shift and amplitude. The numbered peaks and dashed vertical lines serve as a guide for the eye. The chain terminates on the left (0 Å); a Friedel-like oscillation is observed due to the finite length of the chain, and has a wavelength of ~25Å.

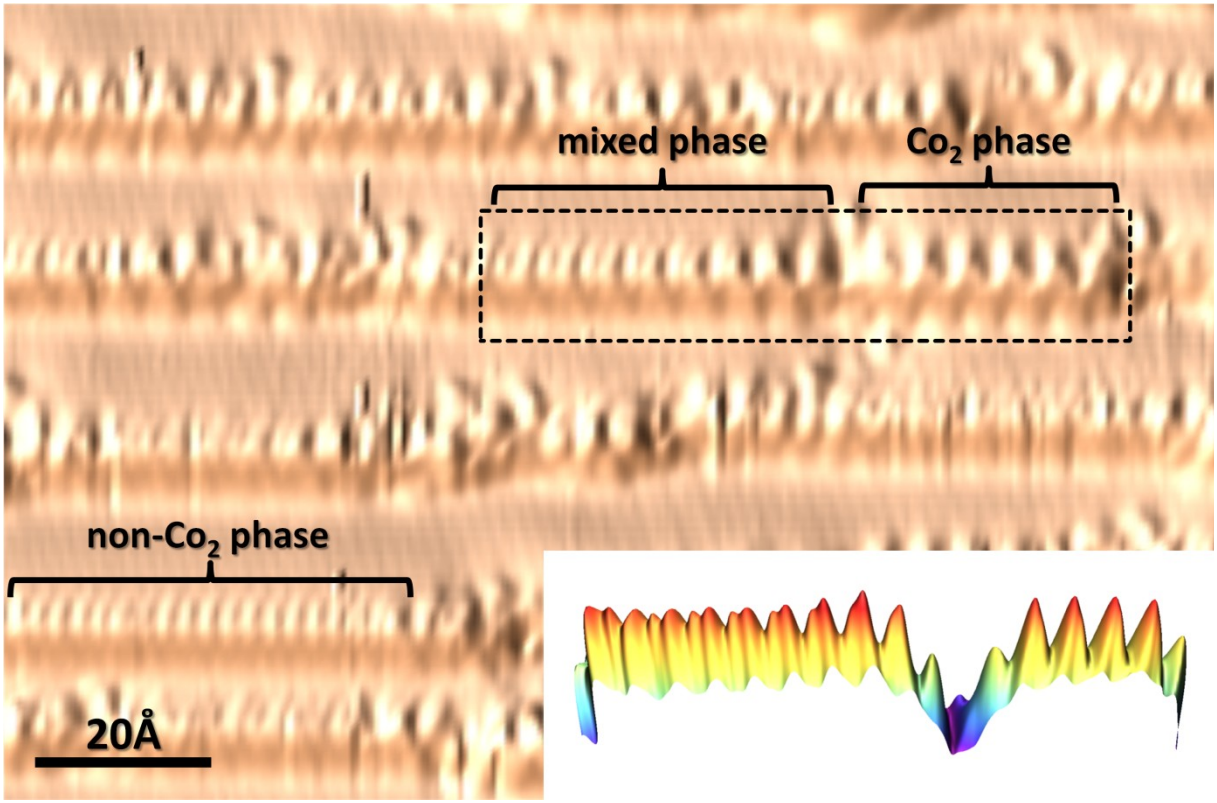

Figure 4.14 Co-existence of two phases of a Co chain at $T \sim T_{Dimerization}$ = 81K**.** STM topography was measured with tip bias of +238mV. Three chains are delineated. A chain with a dimerization instability (labeled "Co_2 phase") exhibits a clear 2× distortion as well as coalescing of the LDOS peaks. A chain without a dimerization instability (labeled "non-Co_2 phase") does not show a 2× distortion; instead, the constituent individual Co atoms are clearly delineable and the nearest neighbor bond length is closer to that of the underlying Cu substrate; the topography is similar to that at $T > T_{Dimerization}$ (see Figure 4.12). The chain labeled "mixed phase" exhibits regions with varying similarity to the dimerization instability phase. In comparison to measurements at this temperature, STM measurements taken at $T > T_{Dimerization}$ exhibit a uniform phase topography. The inset is a rendering of the topography enclosed in the dashed rectangle after applying the substrate subtraction technique of Figure 4.5.

5. A New Deficiency Case for Ab-Initio DFT Methods

Density functional theory (DFT) computations have been immensely successful in predicting physical properties of condensed matter systems throughout the periodic table. However, DFT computations in all known implementations are found to qualitatively break down in certain strongly correlated electron systems [80], sometimes predicting a metal when the system is experimentally observed to be an insulator. Nonetheless, even in these rare scenarios when DFT computations qualitatively fail to describe the electronic ground state, the crystal structure is often still quantitatively accurate. A recent example of a qualitative failure to predict structure was in the rare earth nickelates, where DFT fails to predict the experimentally observed bond disproportionation whereby one Ni-O octahedron expands and another shrinks below some critical temperature [81]. However, even a crude correction of the local interactions as realized in DFT+*U* was able to recover this structural distortion. Here we present a more flagrant failure, whereby the experimental observation of a dimerized Co chain on a Cu surface [82] eludes both DFT and DFT+*U* computations. Using our previous understanding of the mechanism of dimerization [82], we explain how and why both DFT and DFT+*U* fail. This physical example will serve as a testbed for future beyond-DFT total energy methods. In particular, it is possible that DFT+cluster-DMFT (dynamic mean field theory) could be needed to properly capture the structural distortion.

5.1. Methods

Density functional theory (DFT) calculations were performed using the Vienna Ab-Initio Simulation Package (VASP) with a plane-wave basis and the projector augmented wave (PAW) method [72, 73]. Details of the calculations for the Co wire in vacuum case are detailed elsewhere [82]. For all calculations, the spin polarized generalized gradient approximation (GGA) functional was utilized. Since dimerization is driven by Kohn-Sham eigenvalues that lie close to the Fermi level, the accurate (but more expensive) tetrahedron smearing method with Blöchl corrections was chosen. Calculations were performed for different substrate geometries as shown in Figure 5.1; this included Co wire on Cu(111), Co wire on Cu(332), Co wire embedded in Cu(111), and Co wire embedded in Cu bulk. For the surface slab calculations, a vacuum spacer of at least 10Å was afforded. We have compared our results of a 2-layer Co wire/Cu(332) – i.e. 6 step rows – calculation with that of a 8-layer Co wire/Cu(332) calculation, and a 2-layer Co wire/Cu(775) – i.e. 7 step rows – calculation, and observe similar energy phase behavior. Hence, we are confident that the 2-layer Cu surface substrate results presented here will not differ qualitatively from that utilizing more substrate layers or even/odd number of step rows. For the surface slab calculations, at least 3×1×12 *k*-points were used to sample the surface Brillouin zone, where the *z*-direction was *parallel* to the Co wire, the *x*-direction was *perpendicular* to the Co wire and the surface normal, and the *y*-direction was along the surface normal. We found that increasing the number of *k*-points beyond this configuration yielded a negligible energy difference of about 20meV/slab (~0.8 meV/atom) or less. A generous plane-wave energy cutoff of 400eV was used for all surface slab calculations.

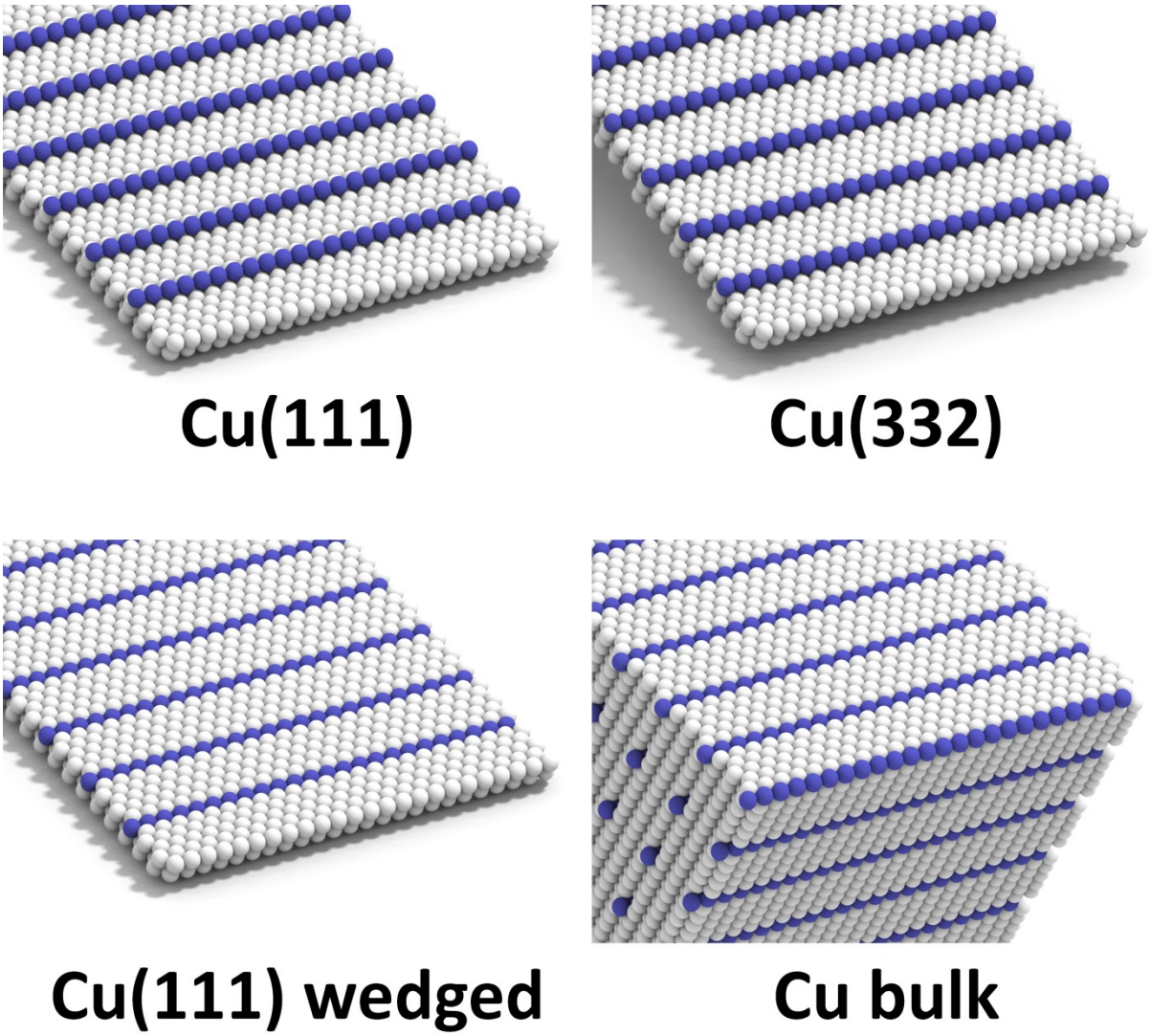

Figure 5.1 Different substrate geometries on which slab calculations for a Co 1-D wire system have been calculated. Cu atoms are colored white while Co atoms are blue. For the Cu(111), Cu(111)-wedged, and the Cu bulk cases, the Co wires make up every 6th row, which gives a wire-to-wire separation of ~13.3Å. For the vicinal substrate case, Cu(332), the step terrace width is ~6 atom rows, and the wire-to-wire distance is ~12.0Å. In this work, these slab geometries are denoted as cases (1)-(4), respectively.

We have found that modeling the wire system using a cluster expansion of the total energy in terms of the spin cluster functions to be illuminating in our understanding of the role of the magnetic contribution as well as the non-magnetic elastic term to dimerization. A binary site variable (such as up/down spin) in a lattice can be modeled using a power

series expansion of any average lattice observable in terms of the correlation functions of the site variables. A highly accurate expansion can usually be obtained for spin systems using only pair terms over a short range. We have found that the energetics can be accurately represented using neighbor and next-nearest neighbor pair terms, as defined in the following equation:

$$H = E_0 + \sum_i J_1 s_{2i} \cdot s_{2i+1} + J_2 s_{2i+1} \cdot s_{2i+2} + J_3 (s_{2i} \cdot s_{2i+2} + s_{2i+1} \cdot s_{2i+3})$$

where E_0 is the non-magnetic energy contribution, s is ±1, and J_1/J_2 are the nearest neighbor magnetic pair interactions, while J_3 is the next-nearest neighbor magnetic pair interaction. An illustration of this model is shown in Figure 5.2. For the Co/Cu system, DFT results show the spin moments reside on the Co sites, and hence this model works equally well for a Co wire on substrate as it does in vacuum. This is evidenced by the small fit errors of less than 1meV/atom for all substrate cases investigated here.

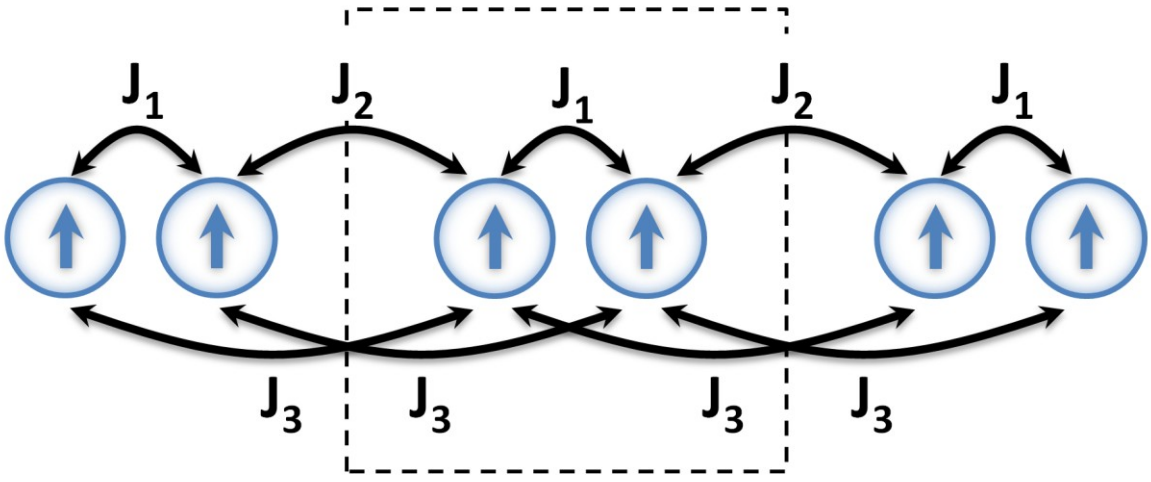

Figure 5.2 An illustration of the cluster expansion model utilized in this work. J_1/J_2 are the nearest neighbor magnetic pair interactions, while J_3 is the next-nearest neighbor magnetic pair interaction. The dashed rectangle denotes one unit cell.

5.2. Results and Analysis

We start with the DFT predicted optimal Co wire position, which is obtained using a full relaxation of the Co atoms while holding the Cu substrate atoms fixed. This calculation was performed for an 8 layer Cu(332) slab as well as a 2 layer Cu(332) slab, (step width of ~12Å), where upon identical results for the Co site positions were obtained, lending further support for using a 2 layer substrate for most of the other surface slab calculations. For the 8-layer case, an additional calculation was performed in which the top 6 Cu atom layers were allowed to also fully relax, while the bottom 2 layers were fixed. For the fixed substrate case, the relaxation results show the Co wire sinking vertically into the Cu terrace by ~0.12Å and horizontally into the step edge by ~0.05Å. For the relaxed substrate case, the relaxation results show the Co wire sinking horizontally into the step edge by ~0.08Å; the vertical sink was a negligible 0.02Å. In all cases, however, the results do not show a structural distortion of the Co wire (the substrate relaxed case showed a relatively trivial distortion of 0.03Å which differed from the non-distorted case by a mere 0.3meV). Instead, the Co atoms are equally spaced and assume the spacing of the underlying ideal Cu atom spacing of 2.56Å. Thus, DFT fails to predict the dimerization of a Co wire, consisting of a short bond length of 2.0Å, that is observed in experiment.

The failure of DFT for this system is peculiar in that DFT does provide an accurate quantitative description of the structural distortion for the *unrealistic* case of a Co wire in vacuum [82]. The availability of an accurate prediction for a model system by way of the *same* ab-initio method provides us with a means of studying why the method fails for a more realistic slab calculation. Understanding the reason for the difference in predictions

between these two cases provides a starting point for improving the method and/or deducing whether a different method may be better suited in obtaining an accurate result.

In a previous work [82], we have determined that the driving mechanism for dimerization in a Co chain is of a magnetic nature. An in-depth analysis reveals strong hopping for the minority spin d_{xz}, d_{yz} orbitals, and to a lesser extent the minority spin d_{z^2} orbital. However, we have also shown that an analysis using a cluster expansion is useful in deducing properties of the chain and the general role of magnetism in favoring the dimerization [82]. Here, we have used the cluster expansion to determine the roles of the magnetic term and the non-magnetic term (also called the elastic term) to dimerization for different wire/slab configurations. Specifically, we have modeled Co wire systems for varying degrees of coordination with the supporting substrate; these configurations in order of increasing coordination number were (1) a Co wire on top of a Cu(111) slab, (2) a Co wire at the step edge of a Cu(332) slab (i.e. a stepped slab), (3) a terrace embedded slab, wherein the Co wire makes up one of the rows in a Cu(111) slab, and (4) an embedded matrix of Co wires in bulk Cu, where each Co wire makes up the 6th row of the slab. Since these calculations are periodic in the plane of the slab, we note that for cases (1) , (3) and (4), the Co wires are ~13.3Å apart, while for case (2), they are ~12.0Å apart. A diagram of the slabs for these different configurations is shown in Figure 5.1. Unless otherwise noted, the Co atoms are located in the ideal site positions of the corresponding substrate Cu atoms. We pursue this treatment here for the purpose of establishing a trend accentuating the cause of the incorrect prediction in DFT.

We computed the energy phase diagram of the aforementioned Co wire slab configurations as a function of the short bond length in a dimerized wire; this is shown in

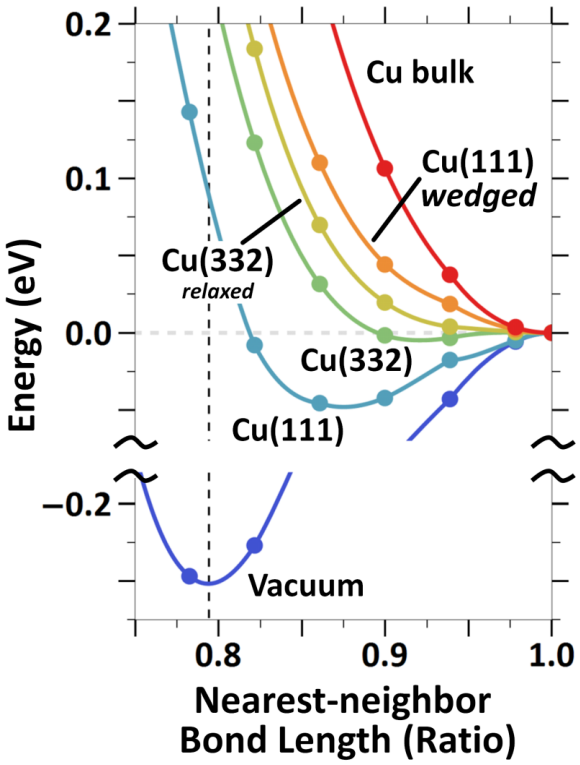

Figure 5.3 Energy phase diagram for a Co wire in different slab configurations. The horizontal axis is the ratio of the short bond length of the Co wire with respect to the non-distorted bond length (2.56Å). The relaxed Cu(332) curve corresponds to the case where the Co wire is positioned at the optimally relaxed position with respect to the Cu(332) substrate. The dashed vertical line denotes the experimentally measured short bond length for a Co wire on vicinal Cu(111).

Figure 5.3. We find that the Co wire weakly dimerizes for case (1), insignificantly for case (2), and not at all for case (3). Hence, under DFT, the degree of dimerization decreases with increasing substrate coordination number. To comprehend the physical role of the coordination number to dimerization, the corresponding cluster fits are plotted in Figure 5.4. As was similarly shown for the case of a Co wire in vacuum, the net magnetic energy term, shown in blue, drives the dimerization, while the non-magnetic term (the elastic term), shown in red, discourages it. Thus, the winner of these two terms dictates whether dimerization is favored under DFT. The plots make it clear that for the case of a substrate supported wire, the magnetic term decreases with increasing coordination number, while the elastic term increases with increasing coordination number; a detailed view of this trend is provided in Figure 5.5. We have also plotted in Figure 5.4 the magnitude of the slope for the magnetic and elastic energy terms as a function of bond length. This type of plot makes it obvious that in order for dimerization to be favored, the slope of the magnetic term needs to be

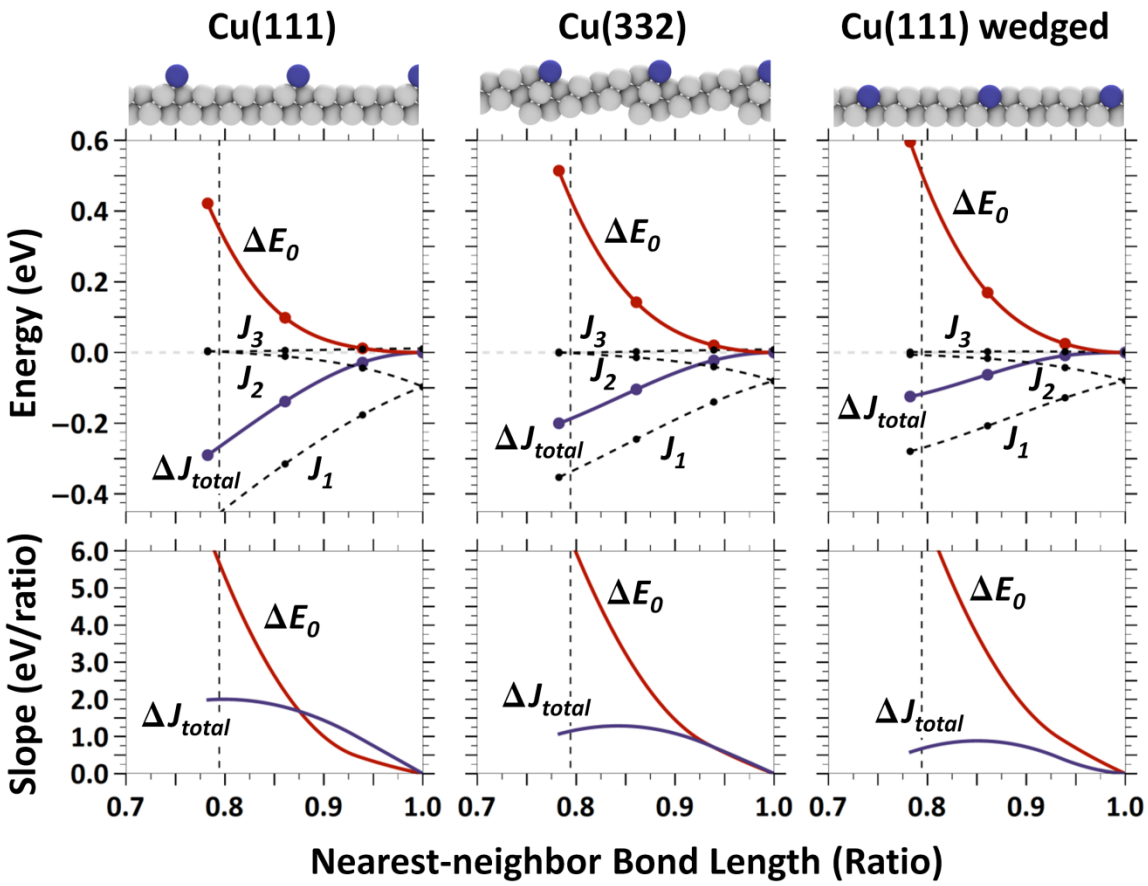

Figure 5.4 Cluster expansion parameter fits for different Co wire slab configurations. The horizontal axis is the ratio of the short bond length of the Co wire with respect to the non-distorted bond length (2.56Å). The bottom row of plots correspond to the slope of the magnetic and non-magnetic energy contributions shown in the above row plots as the blue and red curves, respectively. The dashed vertical line denotes the experimentally measured short bond length for a Co wire on vicinal Cu(111).

larger than that of the non-magnetic term; the bond length corresponding to the intersection of the slope of the magnetic term and the elastic term is the optimal bond length. Hence, for case (1), dimerization is favored because of the initial larger slope of the magnetic term while for case (3), the dimerization is not at all favored since the slope of the elastic term is always larger than that of the magnetic term.

The above given explanation, in which a decrease in the magnetic energy term is cited for the lack of dimerization, is supported by DFT calculations which include

magnetism enhancing techniques. One such technique is the interpolation scheme of Vosko-Wilk-Nusair [83]. In this method, a Padè approximant of a parameterization of the random-phase approximation (RPA) is utilized, and has been shown to enhance the energy of magnetic systems. We indeed have found this to be the case for our Co wire system. By performing the cluster expansion fit for the case 2 system using the Vosko-Wilk-Nusair interpolation scheme, along with allowing for non-spherical corrections to the gradient corrections within the PAW spheres, we find an enhancement of the magnetic moment. This scheme, however, was not effective enough to predict dimerization for the case of a full relaxation of the wire. Note that performing the same GGA calculation with non-spherical corrections but without Vosko-Wilk-Nusair interpolation did not enhance the magnetic term, and hence, did not favor dimerization, while performing the calculation with Vosko-Wilk-Nusair interpolation alone did enhance the magnetic moment, but not as much as when combined with non-spherical corrections.

Having demonstrated that under-prediciton of the magnetic contribution leads to failure of DFT for the Co wire system, a logical step to correct for this is to use DFT+*U*, wherein a user-specified onsite Coulomb repulsion parameter *U* is utilized along with an exchange parameter *J*. DFT+*U* has become a popular extension of DFT that has been shown to enhance the magnetic and orbital moments as well as predict the correct structure and spin phase of transition metal systems [84]. We have investigated the Co wire system using DFT+*U* and have found that it too fails to provide correct qualitative predictions. To demonstrate why DFT+*U* also fails for this system, we first provide the results for the relaxation of a Co wire on Cu(332) substrate, and then analyze in detail the results of

DFT+U for a Co wire in vacuum wherein we show the unfavorable consequences of this single-site local correlation correction method.

We have performed a Co wire relaxation on a 2-layer Cu(332) slab using DFT+U, for the onsite Coulomb repulsion parameter U ranging from $2eV$ to $8eV$ and for a spin exchange parameter J of $1eV$. As noted above, DFT alone predicts a non-dimerized wire that is depressed into the step edge, both perpendicular to as well as parallel to the plane of the step terrace. For DFT+U, however, the Co wire becomes less depressed with increasing U; for $U = 8eV$, the Co wire relaxes to an *undimerized* phase, located ~0.02Å away from the step edge in the plane of the terrace, and situated at almost the same height (only ~0.01Å depression) as the neighboring Cu atoms of the step edge. This is a favorable trend, as it raises the possibility of decreased hybridization with the underlying substrate which, as has been discussed thus far, is inhibiting dimerization. Given this result, one may assume that increasing U further would eventually lead to a Co wire that is dimerized since a large enough U would lead to a negligible hybridization with the substrate. However, this

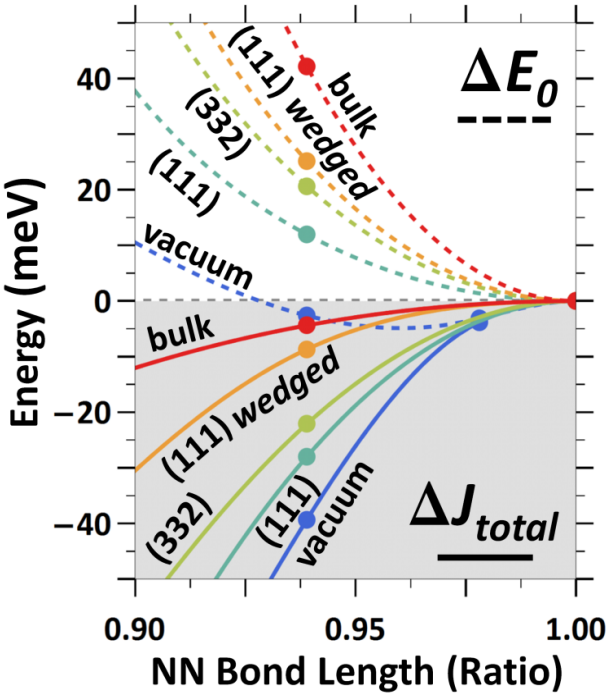

Figure 5.5 An expanded plot of the cluster expansion parameter fits for different Co wire slab configurations, establishing the trend with increasing coordination. The horizontal axis is the ratio of the short bond length of the Co wire with respect to the non-distorted bond length (2.56Å). The solid colored lines correspond to the total magnetic energy contribution; the dashed colored lines denote the non-magnetic energy contribution.

assumption is incorrect, as we will now show. In fact, even if the Co wire was completely separated (both structurally and electronically) from the substrate, it would remain undimerized under DFT+*U*. This is made evidently obvious by the ground state structural prediction for a Co wire *in vacuum*, in which DFT+*U* favors an *undimerized* phase. To understand why dimerization is not favored, we refer to the Kohn-Sham eigenvalue/band diagram for the undimerized Co wire in vacuum case, Figure 5.6, calculated using $U = 4eV$ and $J = 1eV$. In comparison to the corresponding band plot using plain DFT, it is immediately clear that the orbital fillings are quite different, and which agrees with the LDA+*U* bands computed by Wierzbowska et al [85]. Instead of nearly ½-filled d_{xz}, d_{yz} spin-minority orbitals, which preemenintly drive the dimerization as spin-polarized Peierls distortion, these orbitals are completely filled in the DFT+*U* case. Furthermore, the d_{z^2} orbital is rendered completely empty, which previously also assisted in driving the dimerization; instead, the nearly ½-filled *s* orbital is not likely to favor dimerization due to its broad energy bandwidth. Hence, this orbital filling disenfranchises hopping between the d_{xz}/d_{yz} orbitals, a hopping which is essential for dimerization, and also reduces the hopping from these filled orbitals to the now higher energy empty d_{z^2} orbital.

5.3. Conclusions

While DFT is generally *qualitatively* correct for predicting structural parameters, we have shown that DFT computations fail qualitatively to predict the dimerized structural phase for a monatomic Co wire system that is self-assembled on a vicinal Cu(111) substrate. This failure is due to DFT's over-prediction of hybridization of the Co wire with the underlying Cu substrate. We used a cluster expansion to demonstrate that this over-

hybridization leads to weakening of the magnetic coupling along the wire, which is necessary for dimerization, while increasing the stiffness of the wire due to strengthening of the non-magnetic elastic term. One may expect that the single site Coulomb correction method, DFT+U, would correct for this over-hybridization and thus recover the

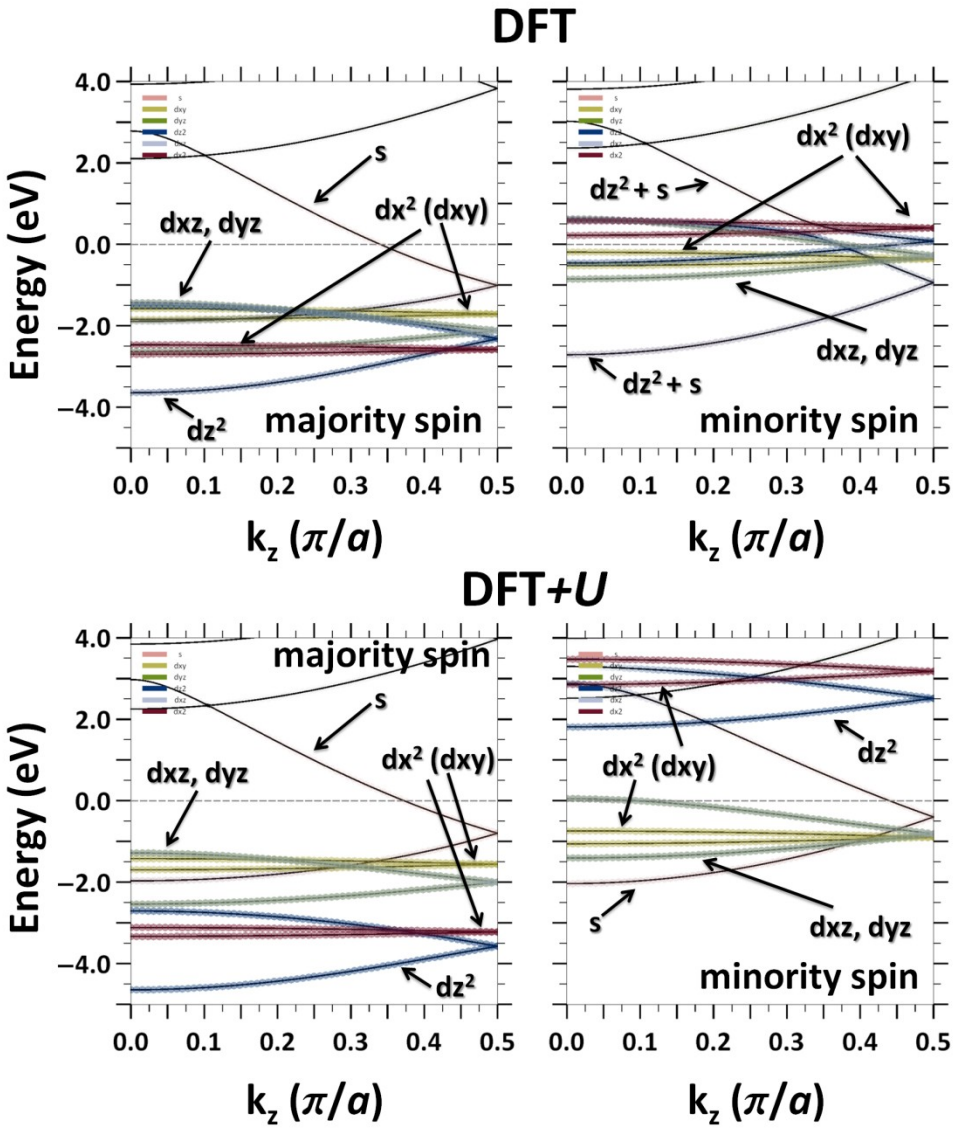

Figure 5.6 Orbital projected Kohn-Sham eigenvalue band diagram for a Co wire in vacuum. The Co atom spacing is $a = 2.56$Å. The top row plot corresponds to the spin polarized GGA DFT calculation while the bottom row corresponds to the DFT+U version with $U = 4eV$ and $J = 1eV$.

dimerization. However, we demonstrate that this too fails due to changes in the orbital filling that are induced by this method, and hence, the Co wire remains un-dimerized. A Co chain on a Cu step should be viewed as a new test case for beyond-DFT total energy methods such as DFT combined with dynamical mean-field theory and its cluster extensions.

5.4. Appendix : finite length monatomic wires

While the calculations in this work have focused on monatomic wires of infinite length, we note that slab supported calculations have been performed for the case of step-substrate supported finite length chains [61]. Pick et al found that for finite length chains, calculated for chains lengths up to 7 atoms, the Co chains did not exhibit a CDW dimerization instability but rather varying amounts of anisotropic strain. We too have performed structural relaxation calculations for finite length chains up to 10 atoms in length, using a 2 layer slab geometry and restricting relaxation to the Co chain atoms, and have obtained similar results as Pick et al. The closest resemblance to a dimerized Co pair was found for the case of a 2-atom Co chain (i.e. a true dimer), which had a bond length contraction that was approximately 60% of the experimentally measured dimerization contraction. For chains longer than two atoms, only the pair of atoms at the end of the chain showed significant collinear contraction; the contraction due to this end effect was approximately 44% of the experimentally measured dimerization contraction.

6. Surface-State Character Transition

Recently widespread interest has developed in understanding the detailed electronic structure of steps and step arrays on low-index vicinal-cut single-crystal surfaces [86]. On bare surfaces, regular step arrays can be formed with relative ease following sputtering and annealing of vicinal-cut metal crystals. In addition, the use of edge-defined growth on vicinal surfaces makes it possible to also form bimetallic one-dimensional systems [18, 31, 56]. These Angstrom-scale features can in turn be used to examine a wide variety of one-dimensional quantum phenomena [87]. In addition, typical step-terrace dimensions are sufficiently small, i.e. ~ 5-30 Å, to allow quantum-confined structures to be formed with binding energies that are much greater than the thermal energy at room temperature. In effect, step arrays and related Angstrom-scale surface patterning enable quantum-structured condensed matter systems to be fabricated *in situ.*

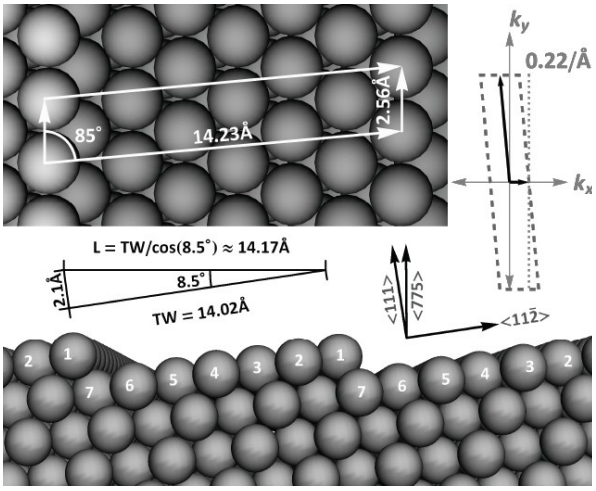

Figure 6.1. Schematic diagram of Cu(775). The 7-row terrace is terminated by (111)-like edges; the steps are denoted as type-B steps, as is the case for all (n,n,n-2) surfaces; in contrast, (n,n,n+2) vicinal cuts are characterized by (100)-like edges and are denoted as type-A stepped surfaces. Due to the odd number of rows per step terrace, the unit cell is not rectangular, as in the case for even number of rows, but a parallelogram. The corresponding surface Brillouin zone is shown in the top right-hand corner, and its boundary in the direction normal to the step-edge is marked with a dotted line along with its wave-vector magnitude.

Because of this interest, a wide variety of studies have been devoted to understanding the fundamental electronic structure of stepped surfaces and how their electronic structure differs from that of low index flat surfaces. A particular focal point of this work has been electronic structure which derives from the well known Cu(111) surface states. Thus recently, extensive occupied photoemission studies on the surface state of a set of vicinal Cu(111) surfaces have been carried out[86, 88] and matched by KKR calculations [89]. In brief, ARPES measurements [90] have shown that two different classes of surface-state modulation exist: terrace-modulation and step-modulation. A terrace-modulated state is a (111) surface state confined by step risers and angle referenced (i.e. having its band minimum aligned) with respect to the terrace normal. A step-modulated state is a step-superlattice modulated state, due to the periodic potential of the steps, angle referenced to the macroscopic surface normal. ARPES measurements have showed that the surface-state class for a particular surface modulation depends strongly on vicinal angle. Thus surface-state modulation is terrace aligned if the vicinal angle is $<5^{o}$ and surface (or cut) aligned if the vicinal angle is $>9^{o}$. The transition for this behavior was attributed in Refs. [86, 91] to the fact that at high vicinal angles the terrace-modulated state overlaps with bulk states (i.e. it becomes a resonance) and hence is less confined by surface features such as step potentials. The ARPES study also showed that Umklapp features occurred only for step-modulated electrons. The intensity of these features was found to vary with photon energy[92], a result attributed to matching of the final bulk electronic wavefunction with the evanescent tail of surface state wavefunction; this interpretation was verified by KKR calculations[89], which also explained the asymmetric appearance of the spectra with respect to the surface normal. Subsequent measurements [88] showed the importance of

considering step-width disorder for interpreting spectra from large-terrace (i.e. <5°) vicinal surfaces.

In this chapter, we focus on using angle-resolved photoemission, in conjunction with *in situ* STM, to determine step-induced surface-state modulation for Cu(775). This vicinal surface is of particular importance since it is close to the transition point between the two different surface-state modulations and thus measurements on this substrate provide insight into the nature of the dominant modulation. These measurements show a variation in Umklapp intensity with photon energy indicating that the predominant reference plane is that of Cu(775), i.e. that the surface is predominately step-modulated. Our measurements also show a weak terrace-modulated state, which we attribute to the presence of terrace widths larger than the ideal terrace width. Finally we discuss the implications of these results to the current understanding of photoemission from surface states on vicinal surfaces.

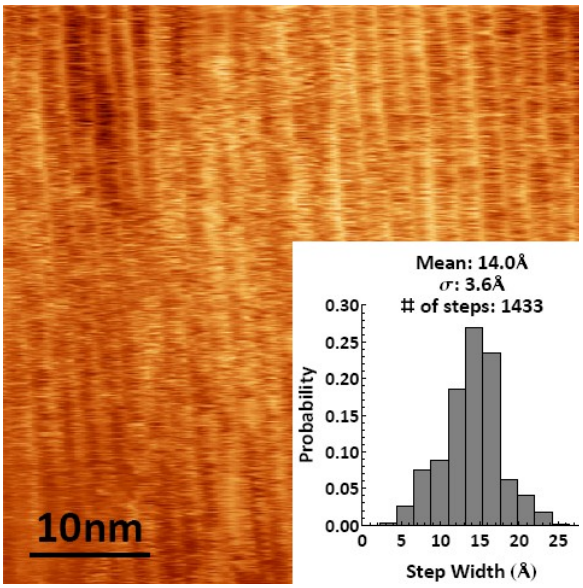

Figure 6.2. (50nm x 50nm) RT STM image of Cu(775). The inset is a step-width distribution of Cu(775).

6.1. Experiment

The crystal surface examined in this paper is Cu(775), namely vicinal Cu(111) cut at 8.5°, which ideally consists of an array of type-B steps [33] with a step width of 6 1/3 atomic rows or approximately 14Å; see Fig. 6.1 for a diagram and relevant crystal

orientation. Sample preparation, STM imaging of the stepped surface, and ARPES measurements were all performed *in situ* under UHV conditions with a base pressure ≤ $1x10^{-10}$ Torr at the multi-instrument APE beamline [93] of the Elettra Synchrotron Facility in Trieste, Italy. This capability is essential for having both STM and photoemission carried out under well quantified conditions. For surface preparation, the electropolished sample was first subjected to repeated sputter and anneal cycles in order to remove bulk contaminants at the surface. These cycles consisted of sputtering at 2KeV at RT, annealing at 650ºC in H_2 at 10^{-6} Torr, and annealing at 650ºC in vacuum. A relatively uniform step array was obtained as shown in the STM image of Fig. 6.2 [56]. Second, the sample was re-cleaned daily using a mild sputter cycle of 1KeV and short annealing at a temperature of 450-475ºC. The sample was illuminated using the low-energy branch of the beamline with a photon energy range of 10-100eV and with p-linearly-polarized light. Room-temperature PE spectra were measured with a VG Scienta SES2002 electron-energy analyzer with an energy resolution of 10meV, an energy width lower than the expected thermal broadening, and with an angular resolution of 0.12^{o}.

6.2. Observations

Prior to and following photoemission measurements, *in situ* STM imaging was made of the surface. An example of this imaging is shown in Fig. 6.2 for one 50nm x 50nm region of the surface. Other regions were also examined *in situ*, as well as investigation of the surface preparation procedure *ex situ* in our laboratories at Columbia University. Figure 6.2 shows a regular step array displaying generally the dimensions expected for this surface, i.e. a terrace width of 14Å and a monolayer step riser; note that very large isolated (111)

terraces were not observed. Because earlier studies have shown the importance of disorder in understanding stepped surface electronic structure, we carried out a statistical analysis of the images using an in-house imaging processing code that takes into account plane correction of a stepped surface, step-height/step-edge recognition, and average step-edge direction. This analysis enabled determination of the step width distribution shown graphically in the inset in Fig. 6.2. As has been observed previously[33, 94], due to the thermally activated step fluctuations and step-interactions, this surface has a distribution of terrace widths, which were characterized by a mean width of 14Å and a width range that extended to ~26Å.

ARPES measurements at several photon energies spanning the range 15eV to 80eV were made on clean Cu(775). The measurements were performed for electrons emitted both perpendicular to and parallel to the step direction. The 1st surface Brillouin zone (SBZ), shown in Fig. 6.1, has boundaries of $\pm\pi/L = \pm 0.22 Å^{-1}$ in the step perpendicular direction; repetitions or Umklapps of this zone exist in the step perpendicular direction with boundaries $\pm(\pi/L = 0.22 Å^{-1}, 3\pi/L = 0.66 Å^{-1})$, $\pm(3\pi/L = 0.66 Å^{-1}, 5\pi/L = 1.10 Å^{-1})$, … , $\pm((2n+1)\pi/L, (2n+3)\pi/L)$. Unless noted otherwise, the $(\pi/L = 0.22 Å^{-1}, 3\pi/L = 0.66 Å^{-1})$ Umklapp zone will be denoted as the 2nd zone and the $(3\pi/L = 0.66 Å^{-1}, 5\pi/L = 1.10\ Å^{-1})$ Umklapp zone will be denoted as the 3rd zone; note that these do not generally correspond to 2nd or 3rd SBZ's; note that the repeating zone scheme is used in the step perpendicular direction. In the case of step-perpendicular PE at low photon energy (i.e. < 46eV), the measurements clearly showed a parabolic dispersion curve whose minimum binding energy was centered at the 1st -2nd zone boundary; see Fig. 6.3. This figure also includes the 2nd derivative of the ARPES data to accentuate the states. At higher photon energy, a replica

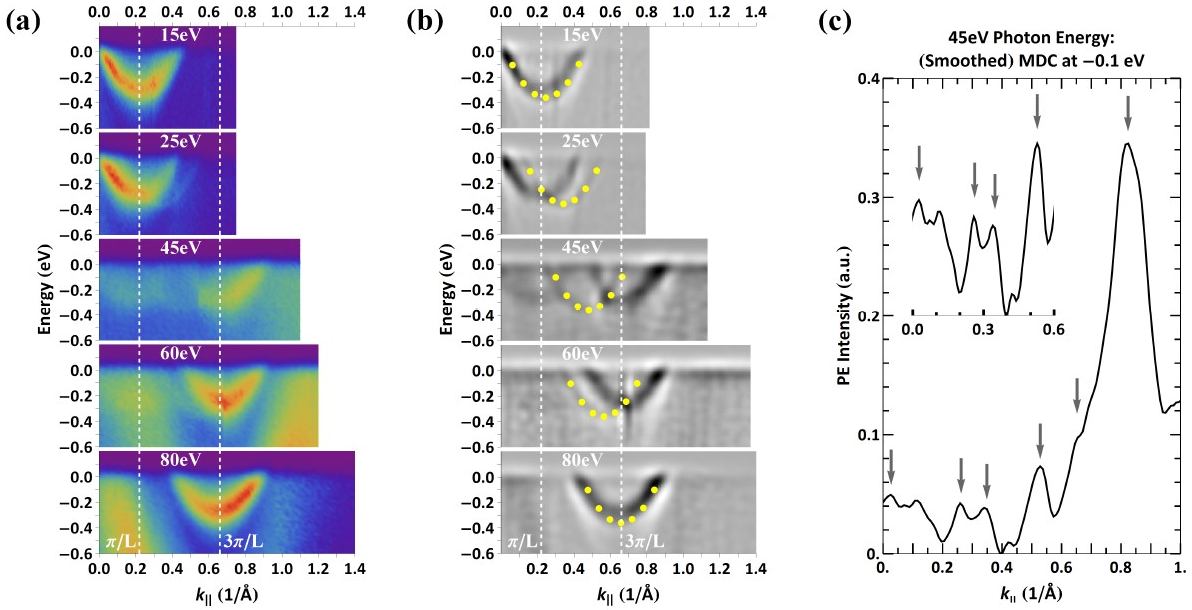

Figure 6.3 (a) RT ARPES of clean Cu(775) in direction perpendicular to steps (i.e. -kx). (b) 2nd derivative of ARPES data in (a). By varying the photon energy, the step-modulated surface state and its umklapp can be observed. As expected, the surface-state band minimum appears at the zone boundaries, as indicated by the white dashed vertical lines. Note that the faint state, indicated by yellow dots in (b), shifts with photon energy. This state is aligned with the step terrace normal, instead of the macroscopic surface normal, and hence is a terrace-modulated state. Apparently, for Cu(775), there are two competing modulations, step vs. terrace, as evidenced by the above ARPES measurements. (c) Example of a (smoothed) momentum distribution curve (MDC) taken at -0.1eV using ARPES data from 45eV photon energy; the marked peaks correspond to the step-modulated surface state, its Umklapp and the terrace-modulated state.

of this feature is observed at a minimum binding energy centered at 3π/L, corresponding to the 2nd -3rd zone boundary. This feature is clearly an Umklapp replica of the surface state. For all photon energies the surface state and its Umklapp replicas were observed in only one half of the macroscopic surface plane; this half corresponds to the left side relative to [775], which includes the [111] direction as shown in Fig 6.1. The absence of a surface state and Umklapp bands observed symmetrically around $k_{||}$ = 0, i.e. bands do not appear for negative $k_{||}$, is consistent with earlier measurements on other vicinal cuts [95] and the

theoretical discussion by Eder, *et al*[89] who attribute this lack of symmetry to interference among the outgoing electrons. In particular, we observe half of the sp-derived surface state in the 1st zone, all of the first Umklapp in the 2nd zone, and half of the second Umklapp in the 3rd zone. To determine the binding energy, effective mass, and the linewidth of this state, photoemission data measured at 25eV is used since this procedure gives the best combination of momentum resolution and minimizes the overlap with an additional faint state, to be discussed below, relative to that at 15eV. The measured binding energy and linewidth is found to be 271 (±3) meV and 228 (±10) meV, respectively. These values agree well with our previous PE results on clean Cu(775)[19] and with the expected trend in linewidth, as reported in an earlier study of stepped surfaces[88]. The effective mass is measured to be ~0.57 m_e; this value is close to our previously measured value of ~0.47m_e[19].

A striking effect, seen in Fig. 6.3, is the variation of the Umklapp intensity with the variation in photon energy. Thus, there is change in surface-state intensity in going from the combined 1st-2nd zone to the 2nd-3rd zone. For photon energies less than ~30eV, the relative surface-state intensity is highest in the 1st-2nd zone. For photon energies greater than ~40eV, the surface-state intensity is highest in the 2nd-3rd zone. Measurements of the variation in the PE intensity for photon energies between 30-40eV were not possible due to the weak photon emission intensity in this region. As mentioned above, the variation between the combined 1st-2nd zone and the combined 2nd-3rd surface zone has been discussed previously with respect to Au and Cu vicinal-cut surfaces. In Fig. 6.3b a 2nd derivative-plot of our data shows more clearly the surface state and its Umklapp. This filtered data reveals that at 45eV both curves cross the Fermi level before crossing with

each other. This observation will be discussed later on in the analysis section.

The ARPES measurements in Fig. 6.3 also reveal a faint state that shifts in $k_{||}$ with photon energy; this feature is highlighted using yellow dots in Fig. 6.3b. Its effective mass is measured to be ~0.5m_e, that is, the same as the usual (111) surface-state value. As this state shifts in $k_{||}$, it is obscured at some photon energies by the stronger Umklapp feature as seen clearly in the data at 15eV and 80eV photon energies. Careful measurements show, however, that the binding energy is higher, ~360 meV, than the binding energy of the step-modulated state, and its linewidth is distinctly narrower, ≤ 120 meV. By examining the angle-space PE equivalent of Fig. 6.3, it is apparent that the band minimum of this state is aligned to the terrace normal. Since $k_{||} = \frac{\sqrt{2m_e E_{kin}}}{\hbar}\sin\theta$, the band minimum, located at 8.5°, will have $k_{||}$ change with photon energy, and hence the reason for the shift in $k_{||}$.

A careful consideration of the above data shows that characteristics of this weak state are those of a terrace-modulated state. First, the state's band minimum is aligned with the terrace normal, i.e. the [111] direction, instead of the macroscopic surface normal or the zone boundaries. Second, its larger binding energy of 360meV, compared to that of the step-modulated state, is that expected for a terrace-modulated state [88]. Third, this state does not show the characteristic Umklapp or bandfolding that is expected of step-modulation. The appearance of a weak terrace-modulated state raises the possibility that perhaps the surface preparation of Cu(775) left a mixed surface phase, that included minority regions of relatively large Cu(111) or macroscopic flat areas. However our STM imaging of the surface, including regions different than in Fig. 6.2 did not show any such regions; instead, as shown, for example, in the sample image of Fig. 6.2, the overall surface

structure was relatively uniform across the sample. As mentioned earlier the finite step distribution seen in STM images is a consequence of the thermal activation at room temperature. The relatively uniform nature of our Cu(775) surface is reflected in the tight PE EDC linewidth; thus, we measure a linewidth of ~230meV, which is close to an expected linewidth of 180meV[88]. Note a measurement of the linewidth was complicated by the presence of the terrace-modulated state, which because of some residual overlap, gives the appearance of a larger linewidth.

The finite step distribution does play an important role in the presence and appearance of the faint step modulated state. The terrace-modulated state is characterized as a localized state on the terrace. It has been observed previously on Cu(665), a vicinal Cu(111) surface with mean terrace width of 25.2Å and a standard deviation derived terrace width range of 16.1Å to 34.3Å [88]. This prior work showed that in the presence of this distribution of terraces, these terraces, which individually support a specific quantum well state with flat energy dispersion, do exhibit an apparent free-electron like energy dispersion. Hence, this distribution changed the expected quantum-well energy dispersion to resemble a free-electron-like dispersion. As shown in Fig 6.2, the step-width distribution of Cu(775) includes terrace widths within the above cited range, albeit with lower probability compared to terrace widths close to the ideal of 14Å. To summarize, spatially on the surface, the predominate step-modulated state exists over an array of terrace-widths close to the ideal of 14Å. These step-modulated surface state supporting step-arrays are, however, interrupted by the larger width terraces in the step distribution, which support localized terrace-modulated states. Hence, the two surface-state modulations do not co-exist on the same step, but belong, respectively, to a step array of almost ideal step-

width, and to a terrace of a larger step width.

The identification of the weak state as a terrace-modulate or localized state is further supported by the following observations. The weak state binding energy and linewidth are closer to that of Cu(665), mentioned above, than they are to flat Cu(111). In our case, the binding energy and linewidth are, respectively, ~360meV and ≤ 120meV; on Cu(665), they are ~350meV and 90meV; in the case of Cu(111), they are ~390meV and ≤ 60meV. As discussed further below, the ratio of the PE intensity of the second state to the combined PE intensity (predominate state plus weak state) is 0.22, suggesting that 22% of the sample area contributes to the second state. However, our STM studies on Cu(775) do not reveal large terraces that take up this percentage of the surface area. Hence, it is unlikely that source of the weak state signal is a few large terraces but rather a distribution of many terraces across the surface with widths large enough to hold a localized state.

In order to quantify better the presence of the weak terrace-modulated state, a measurement was made of the PE intensity ratio of the terrace-modulated to the step-modulated state. This ratio was measured at the band minima of the two states, taken at 25eV photon energy. Analysis at other photon energies was hindered by terrace-modulated-state/stepped-modulated state overlaps and by non-homogenous angle-space intensity mapping. We expect, however, that this ratio to be photon-energy independent, since photoemission intensity is approximately proportional to state population. The results of this measurement showed that the ratio was approximately 0.28 (0.02).

The presence of the terrace-modulated state in the vicinity of the angle for the surface-state-modulation transition, can lend direct experimental insight to the physics, which control this transition. If the terrace-modulated state PE signal is assumed to come

from terrace-widths larger than the mean width, the above intensity ratio can be combined with a width-weighted terrace-width distribution to arrive at a value of the terrace width, at which the surface-state modulation switches. Using this approach, we calculate a value of 17.4Å (0.6) for the minimum terrace width. This value is close to the previously reported [90] transition terrace-width of 17Å. Furthermore, it is in agreement with the exclusively type-B vicinal Cu PE studies [88], in which 16.3Å average-terrace-widths were shown to be step-modulated while 25.2Å average-terrace-widths were shown to be terrace-modulated. This result should be of value in further theoretical studies of this transition point.

6.3. Analysis and Discussion

In our discussion in this section, we first address the variation in surface-state intensity with photon energy. First and most important as stated above, the observation of photon-energy dependence for Umklapp features appearing at two different zone-edge momenta $k_{||} = \pi/L$ and $3\pi/L$ is clear evidence that the (775) surface is step-modulated rather than terrace-modulated. This is an important result since it defines more precisely regions of vicinal-angle space, for which the transition described in Ref. [90] occurs.

The specific photon dependence measured in our experiments can be determined readily via use the free-electron approximation [96] for the final state to determine the perpendicular component of the final-state crystal momentum at a given photon energy. A diagram providing a PE transition-space representation that incorporates the free-electron approximation band is shown in Fig. 6.4. This diagram shows the expected [86, 88] initial step-modulated supperlatice state of ideal Cu(775) in white, and the free-electron final-state band in gray, along with direct transitions for a given photon energy, as denoted by

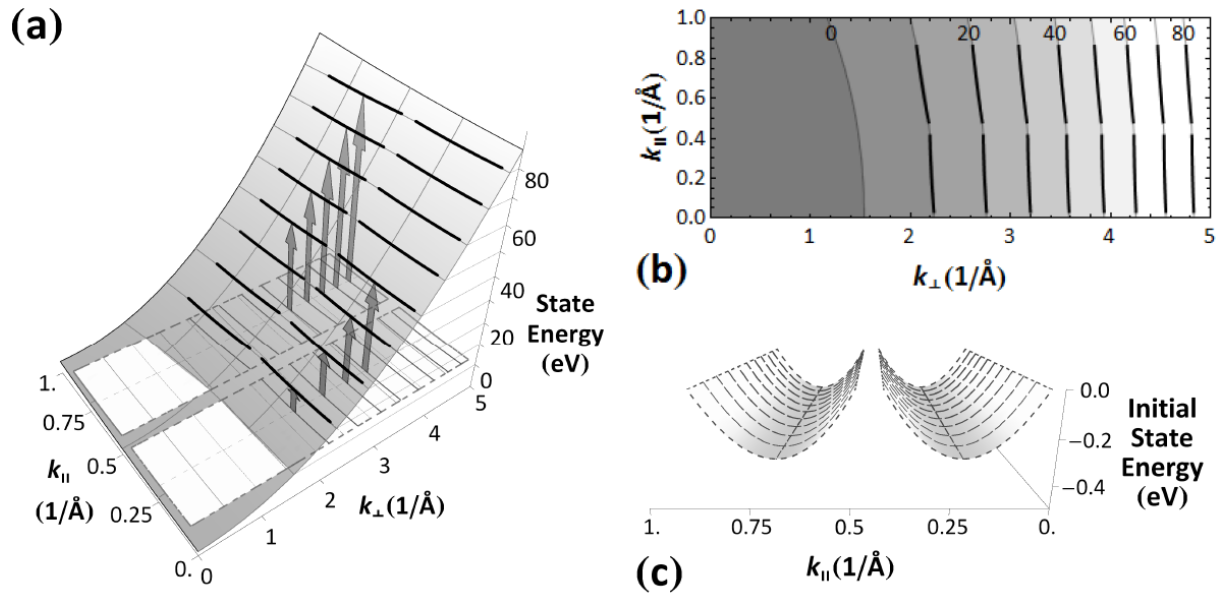

Figure 6.4. (a) Schematic diagram of possible state transitions during angle-resolved photoemission from ideal Cu(775), i.e. perfect step-array of 14.0Å. All energies are referenced to the Fermi level. The initial state band, consisting of the surface state and its Umklapp, i.e. the step-modulated superlattice surface state, is denoted in white, centered at 0.22Å-1 and 0.66Å-1; their dispersion is shown clearly in (c). The final state band, a free-electron band approximation, is denoted in gray, and has a paraboloid shape; a contour plot of this band is shown in (b). Sample transitions for several photon energies are shown in (a) and (b) and some are explicitly marked by arrows in (a). The initial states are marked by thick gray lines on the initial state band in (a) and the final states are marked by thick black lines on the final state band in (a) and (b). Due to the low binding energy of the initial state, it and its corresponding final state appear to follow the lines of constant energy, as shown in (a) and (b).

vertical arrows. It is readily seen in the diagram that a transition from either the surface state or its Umklapp is possible at any photon energy. Hence, the reason for the observed intensity variation with photon energy is not due simply to the absence of an available final state at certain photon energies.

Ortega and his collaborators have provided insight into the origin of this alternating pattern of PE intensity with photon energy for the case of the stepped Au(322)[97] and later Cu(223)[92] by pointing out that it is a necessary consequence of photoemission resonances. These APRES resonances, which were first explained for the case of flat

Cu(111) in Ref.[98], are the result of the periodicity in the evanescent portion of the full wavefunction in the direction normal to the surface. When inserted into Fermi's Golden Rule for the ARPES probability, this z-periodicity of the wavefunction gives rise to resonances for final-state free-electron wavefunctions of the same periodicity in k_{perp} or its higher harmonics. Specifically, these conditions cause the final state k- vector to be (2n+1) π/a_z $k_{[111]}$, where $k_{[111]}$ is the unit k-space vector in the [111] direction. These resonances have been examined in the more recent theoretical study of photoemission on narrow-terrace stepped Cu(111) by Eder, *et al*[89] cited above, which used the screened KKR self-consistent method to investigate surface-state spectral resonances for both flat and stepped Cu(111), i.e. Cu(111), Cu(332) and Cu(221), respectively. For the sake of specificity, these authors focused on photon-energy resonances at the band minimum and showed that a series of resonances exist at the $k_{||}$ discussed earlier by Ortega. For resonances on a *stepped* surface, the same basic physical effects lead to resonances as on a flat surface. However, due to the tilt of the surface with respect to the crystal plane, interference between the out-going electron with its initial state causes the final state that is parallel to the [111] direction, i.e. the local terrace normal instead of the surface normal, to have a finite amplitude. Thus the first resonance in photoelectron signal occurs at n=0 at low photon energies, e.g. ~0eV for Cu(775), which for this vicinal-cut sample corresponds to $k_{||}= \pi/L$ or the 1^{st}-2^{nd} zone boundary. The resonance for n=1occurs at $k_{||}=3\pi/L$, i.e. the 2^{nd}-3^{rd} zone boundary at higher photon energy. The predicted photon energy for n=1, according to Ref. [89], is 69eV, a value which agrees with our experiment results. Note that the above discussion of intensity variation with $k_{||}$ is based on the fact that our signal arises from a superlattice state and thus displays Umklapp replicas. Thus a second question

regarding our results is why is such a superlattice state seen rather than the terrace-confined quantum-well state, which occurs at larger terrace widths.

One appealing explanation for the transition from step- to terrace-modulation that has been advanced is that a reduction of the projected band-gap with increasing vicinal angle causes the terrace-modulated surface state wavefunction to switch to step-modulated [91]. As a result it is important to confirm the presence of any band gap on our surface and to track its change with vicinal-cut angle. Accordingly tight-binding calculations [99] were used to calculate the projected gap with angle. In this calculation, a Slater-Koster tight-bonding interpolation scheme [100] was used to calculate the energy eigenvalues along any crystallographic direction using the eigenvalues calculated at high symmetry points from an APW (Augment-Plane-Wave) calculation; hence given a desired crystallographic direction, the k-space along that direction was adequately sampled to determine the band projection in that direction. To obtain the projection of the bulk bands, we follow the practice of other studies on vicinal surfaces (Au and Cu) of projecting the bands of the 1st Bulk BZ [86, 101, 102]. The result of band projections within the 1st Bulk BZ for three different (111) vicinal cuts, plus that for the flat surface, is displayed in Fig. 6.5. Clearly, the [111] band projected bandgap does not close or disappear for the (775) vicinal cut examined in this paper. Instead, its form remains approximately the same as for the flat (111) surface, though it does shift in $k_{||}$ with increasing angle and, due to the tilt of the surface, is centered at the SBZ edge on the side of $k_{||}$ which holds the [111] direction. For the case of small vicinal cuts (<5º), a terrace-modulated surface state (i.e. a surface state with a (111) reference plane), will fit within the projected bandgap [91]. However, for vicinal angles > 7.5^{o}, bulk-states overlap completely with the projection of the terrace-

modulated surface state [91]. This overlap will cause the terrace-modulated state to become a broad resonance and loose spectral weight [91] and cause it to be unobservable in an EDC of the surface. Further as shown in the figure and discussed earlier in [91] due to the fixed (111) orientation of the terrace, the step-modulated state remains in the projected bandgap for all the vicinal angles show in Fig. 6.5, thus giving a strong PE signal. While this explanation is very helpful in understanding the physics of the terrace/step modulation switch, it apparently does not fully explain why the step-modulated state is not observed for samples with smaller vicinal angles.

An alternate more recently advanced explanation for the switch from step to terrace modulation is based on measurements that suggest that this switch is a result of subtle

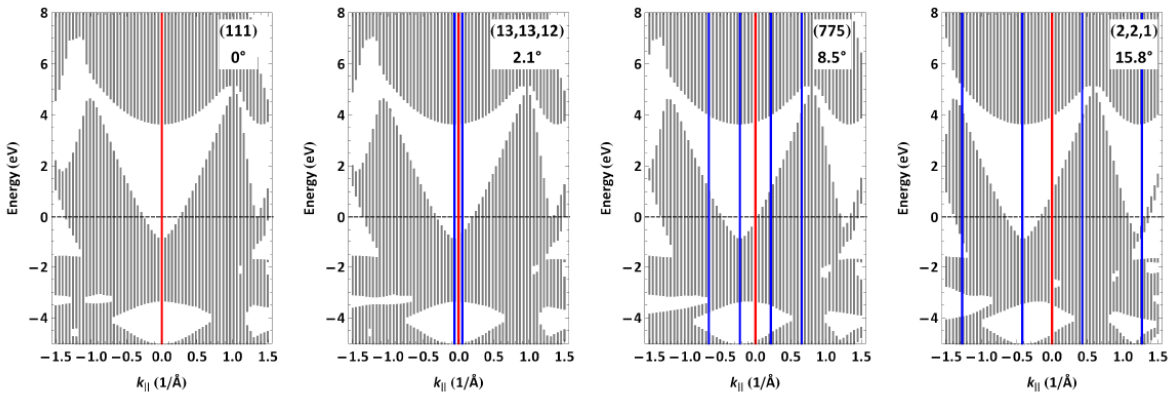

Figure 6.5. Cu Bulk projection of 1st BZ for flat and vicinal Cu(111) surfaces. The *sp* surface state gap is at k||=0 for Cu(111) as expected. Note that the projection is not symmetrical with respect to k||; though the surface BZ of Cu(111) is 6-fold rotationally symmetric, the bulk BZ possesses only 3-fold rotational symmetry along the[111] direction which is reflected in the projection. For these vicinal surfaces, the sp gap shifts in the direction of $\overline{M}'$ (i.e. toward bulk symmetry point X), but does not close or lose noticeable volume with vicinal angle. The vertical red line denotes k||=0 which corresponds to the macroscopic surface normal. The blue vertical lines correspond to ±π/L and ±3π/L. Note that the sp gap minimum is aligned with the first surface BZ boundary,-π/L, as is the case with the step-modulated surface state. Also notice that there is no projected gap for the Umklapp surface state, centered at -3π/L. Furthermore, there is no projected gap for positive values of k||, i.e. k|| ≥ 0.

changes in surface energetics[88]. This explanation rests on PE measurements of the opening of a bandgap in the superlattice state on Cu(443)[103] and concomitant rearrangement in the density of states below the Fermi level. For this surface, the authors of Ref. [103] observed a bandgap at the Fermi level in the step-modulated state, giving a calculated energy gain of ~11meV/unit cell compared to a gapless case. Cu(775) is very close to Cu(443) in terms of terrace width, 14Å vs. 16.2Å respectively, and hence would be expected to have a similar energy gain. Kronig-Penney modeling of the gap[103] showed that this energy gain persists as the terrace width increases until for terraces with width >26Å, the energy gain is replaced by an energy loss[103]. This loss of energy gain is due to the fact that the gap moves deep below the Fermi level. The energy gain of the superlattice or step modulated state in going from large to short terraces with increasing vicinal angle causes the step-modulated state to lie lower in energy and to dominate and thus for the PE signal from this state to be seen. Finally the authors of this work note that it is possible that energy conditions "might not be sufficient to explain the observed cross over" and they note that localization due to step disorder may also play a role in the transition from superlattice states[88]. Following the explanation based on the importance of a gap, we note again that Cu(775) is very close to Cu(443) in terms of terrace width and, in fact, a plot of energy gain versus average terrace size obtained in Ref. [103] shows that for the 14Å terraces of Cu(775) a similar energy gain of 10meV per unit cell is obtained. In the case of Cu(775), however, the gap lies above the Fermi level and thus is not possible to observe in photoemission. Thus our results are not inconsistent with an explanation based on a gap opening, although this explanation could not be confirmed with our experiments.

6.4. Conclusion

Our photon energy-dependent photoemission measurements on narrow-terrace-width vicinal Cu(775) crystal have enabled us to examine the transition region in vicinal-angle space for a change in the surface reference plane from predominately step-modulated to terrace-modulated. Our data also provide a clear example of the variation of the photoelectron signal intensity of the Umklapp features with photon energy, a variation, which supports the assignment of step modulation to the (775) surface. In addition, our measurements show evidence of a faint terrace-modulated state, further emphasizing the proximity of our vicinal cut to the transition angle between terrace-modulation and step-modulation. This observation of a terrace-modulated state allowed us, in combination with STM measurements of the terrace-width distribution, to arrive at a value for the terrace-width at which the surface modulation switches. Our ARUPS identification of the surface-state class on Cu(775) is also consistent with recent discussions of the origin of the switch from step- to terrace-modulation in [88, 91]. Finally, we note the very recent publication of a PE/STM (ex-situ) study of vicinal noble metal step-width distributions and their interplay with the surface state [104].

6.5. Appendix: Fourier analysis of photoemission intensity

The following derivation provides a compact, somewhat more intuitive summary of the theory by Eder, *et al*[89] regarding photoemission from a vicinal surface. Assuming single-particle electron dynamics, we use Fermi's golden rule to obtain the intensity of a photoemission signal:

$$\left\langle \psi_{final} \left| \vec{A} \bullet \vec{P} \right| \psi_{initial} \right\rangle$$

where $\vec{A}$ is the incoming-photon vector potential and $\vec{P}$ is the momentum operator. Since the final state is a free-electron state, $\left|\psi_{final}\right\rangle = \left|e^{-i\vec{k}_{final}\bullet\vec{x}}\right\rangle = \left|k\right\rangle$, and since in our experiment $\vec{A}$ is p-polarized, the photoemission intensity is proportional to:

$$\left\langle k\left|\sum_{x,y,z} P\right|\psi_{initial}\right\rangle = \hbar(k_x + k_y + k_z)\left\langle k\left|\psi_{initial}\right\rangle\right.\left.\right.$$

Hence, the photoemission intensity for a final state electron with k-vector in the x-z plane, $\langle k_x, 0, k_z\rangle$, is proportional to the magnitude of the Fourier transform of the initial wave function $\psi(x,y,z)$ evaluated at $(k_x,0,k_z)\rightarrow(k_x,k_z)$.

The above can be used to predict the photoemission intensity of surface states for vicinal Cu, where k_x and k_z are relabeled as $k_{||}$ and $k_{\perp}$ to denote momentum parallel to and perpendicular to the macroscopic surface, respectively. For example, in the case of Cu(111), the initial state of interest is at the $\overline{\Gamma}$ point, i.e. the state with crystal momentum $(k_x^i = 0, k_y^i = 0)$. To determine the photoemission intensity, we need a map of Fourier transform magnitude map, $\left|\Psi_{initial=\overline{\Gamma}=(k_x^i=0,k_y^i=0)}(k_x,k_z)\right| = \left|\Psi_{initial=\overline{\Gamma}=(k_x^i=0,k_y^i=0)}(k_{||},k_{\perp})\right|$, of the initial state $\psi_{initial=\overline{\Gamma}=(k_x^i=0,k_y^i=0)}(x,y,z)$. Using KKR, Eder, *et al* determined the functional form of the state at $\overline{\Gamma}$ for Cu(111) to be a decaying square wave in the perpendicular direction with period $2a_z$, where a_z is the layer spacing; see Fig. 6.6a for the function and its Fourier transform. As expected of, say, a 1-D square wave, the Fourier expansion along $k_{||} = 0$ gives intensity maxima at odd multiples of k_z at π/a_z; this behavior has been observed in photoemission experiments from Cu(111) at $\overline{\Gamma}$ [92].

For the case of vicinal of Cu, the first initial state of interest is located at the first zone boundary, $(k_x^i = \pi/L, k_y^i = 0)$, where L is the unit cell length (approximately equal to

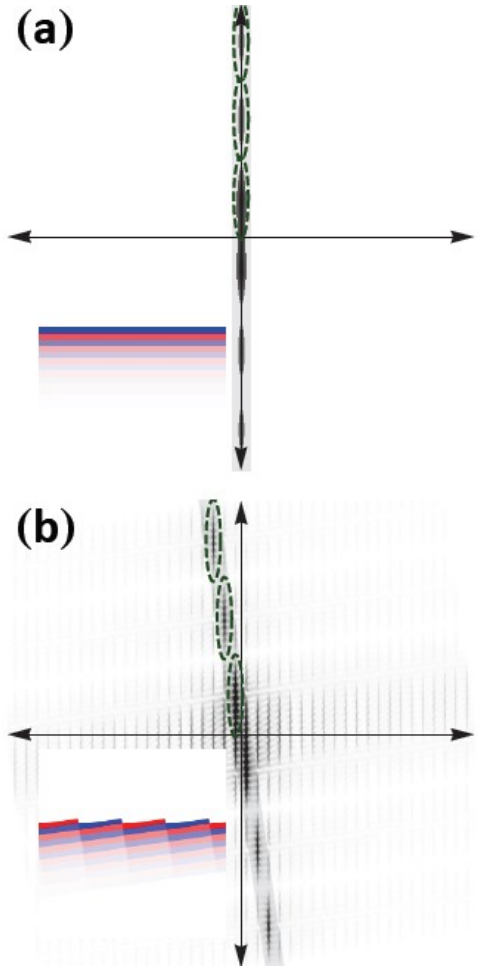

Figure 6.6. Discrete Fourier transform (DFT) of the forms of the wavefunction for different Cu surfaces. (a) DFT for Cu(111) for waveform at $\overline{\Gamma}$. The form of the waveform is shown in the inset; the change in colors from red to blue symbolize the change from positive to negative. The ellipses mark the positions of strong FT intensities or resonances along the $k_{||} = 0$. (b)DFT for Cu(775) for waveform at $(\kappa_x = \pi/L, \kappa_y = 0)$ as well as $(\kappa_x = 3\pi/L, \kappa_y = 0)$. The form of the waveform is shown in the inset; the change in colors from red to blue symbolize the change from positive to negative. The ellipses mark the positions of strong FT intensities along $k_{||} = \pi/L$, $3\pi/L$, and $5\pi/L$. In both (a) and (b), a gray transparent strip is used to enhance the intensities of interest and also denotes the <111> direction.

the terrace width, see Fig. 6.1); in this case the Fourier-transform map, $\left|\Psi_{initial=SBZB=(k_x^i=\pi/L,k_y^i=0)}(k_{||},k_{\perp})\right|$ is required. The computed form of the wave function for this case, based on Eder, *et al,* is shown in Fig. 6.6b along with its corresponding Fourier transform. The form of the wave function is similar to the case of Cu(111) at $\overline{\Gamma}$ except in that it is tilted/rotated by an angle equal to the vicinal angle. The Fourier transform is likewise rotated by the vicinal angle, but otherwise the same. Specifically, note that the intensities remain at the at the same k magnitude, $\sqrt{k_{\perp}^{\ 2}+k_{||}^{\ 2}}=|k|=\pi/a_z$ and its odd multiples. For $|k|=\pi/a_z$, corresponding to the fundamental harmonic of the square wave, the corresponding final-state parallel momentum $k_{||}$ is π/L, using the easily derived relation: $k_{||}=\frac{a_z}{L}|k|$. This is the only resonance with $k_{||}=\pi/L$; use of higher photon energies, and hence higher values of $k_{\perp}$, will not yield any additional photoemission resonances for $k_{||}=\pi/L$.

Looking now at the Fourier intensity map for an initial state located at $(k_x^i=3\pi/L,k_y^i=0)$, i.e. the 2nd-3rd zone boundary, the results are identical to that for the above 1st-2nd zone boundary state. However, the intensities along $k_{||}=3\pi/L$, i.e. $\left|\Psi_{initial=SBZB=(k_x^i=3\pi/L,k_y^i=0)}(k_{||}=3\pi/L,k_{\perp})\right|$ are now of interest and the third harmonic, $|k|=3\pi/a_z$ has a final-state parallel-momentum resonance at $k_{||}=3\pi/L$. This behavior is observed in our experiment as well as in other experiments on vicinal cut noble metal crystals with

surface states exhibiting step-modulation.

7. References

[1] J. Voit, Rep. Prog. Phys. **57**, 977 (1994).

[2] M. Grioni and J. Voit, in *Electron Spectroscopies Applied to Low-Dimensional Structures* (Kluwer, 2000).

[3] V. V. Deshpande, M. Bockrath, L. I. Glazman, and A. Yacoby, Nature **464**, 209 (2010).

[4] P. Segovia, D. Purdie, M. Hengsberger, and Y. Baer, Nature **402**, 504 (1999).

[5] J. R. Ahn, H. W. Yeom, H. S. Yoon, and I.-W. Lyo, Phys. Rev. Lett. **91**, 196403 (2003).

[6] P. C. Snijders and H. H. Weitering, Rev. Mod. Phys. **82**, 307 (2010).

[7] R. Wiesendanger, *Scanning Probe Microscopy and Spectroscopy* (Cambridge University Press, 1994).

[8] E. W. Müller and K. Bahadur, Phys. Rev. **102**, 624 (1956).

[9] C. J. Chen, *Introduction to Scanning Tunneling Microscopy* (Oxford, 2007), 2nd edition.

[10] C. Kittel, *Introduction to Solid State Physics* (Wiley, 1996), 7th edition.

[11] P. Hohenberg and W. Kohn, Phys. Rev. **136**, B864 (1963).

[12] W. Kohn and L. J. Sham, Phys. Rev. **140**, A1133 (1965).

[13] F. J. Himpsel, Adv. Phys. **32**, 1 (1983).

[14] H. Y. Fan, Phy **68**, 43 (1945).

[15] E. O. Kane, Phys. Rev. L **12**, 97 (1964).

[16] S. Hüfner, *Photoelectron Spectroscopy* (Springer, 2003), 3rd edition.

[17] D. Mattis, *The Many-Body Problem* (World Scientific, Singapore, 1993).

[18] P. Gambardella, M. Blanc, L. Bürgi, K. Kuhnke, and K. Kern, Surf. Sci. **449**, 93 (2000).

[19] S. Wang, M. B. Yilmaz, K. R. Knox, N. Zaki, J. I. Dadap, T. Valla, P. D. Johnson, and R. M. Osgood, Phys. Rev. B. **77**, 115448 (2008).

[20] K. Ogawa, K. Nakanishi, and H. Namba, Surf. Sci. **566-568**, 406 (2004).

[21] J. de la Figuera, J. E. Prieto, C. Ocal, and R. Miranda, Surf. Sci. **307-309**, 538 (1994).

[22] J. de la Figuera, M. A. Huertagarnica, J. E. Prieto, C. Ocal, and R. Miranda, Appl. Phys. Lett. **66**, 1006 (1995).

[23] M. Ø. Pedersen, I. A. Bönicke, E. Lægsgaard, I. Stensgaard, A. Ruban, J. K. Norskøv, and F. Besenbacher, Surf. Sci. **387**, 86 (1997).

[24] H. W. Chang, F. T. Yuan, Y. D. Yao, W. Y. Cheng, W. B. Su, C. S. Chang, C. W. Lee, and W. C. Cheng, J. Appl. Phys. **100**, 084304 (2006).

[25] O. Pietzsch, S. Okatov, A. Kubetzka, M. Bode, S. Heinze, A. Lichtenstein, and R. Wiesendanger, Phys. Rev. Lett. **96**, 237203 (2006).

[26] L. Gómez, C. Slutzky, J. Ferrón, J. de la Figuera, J. Camarero, A. L. Vazquez de Parga, J. J. de Miguel, and R. Miranda, Phys. Rev. Lett. **84**, 4397 (2000).

[27] Y. Mo, K. Varga, E. Kaxiras, and Z. Y. Zhang, Phys. Rev. Lett. **94**, 155503 (2005).

[28] J. de la Figuera, J. E. Prieto, C. Ocal, and R. Miranda, Phys. Rev. B. **47**, 13043 (1993).

[29] J. E. Prieto, J. de la Figuera, and R. Miranda, Phys. Rev. B. **62**, 2126 (2000).

[30] S. Speller, S. Degroote, J. Dekoster, G. Langouche, J. E. Ortega, and A. Närmann, Surf. Sci. **405**, L542 (1998).

[31] J. D. Guo, Y. Mo, E. Kaxiras, Z. Y. Zhang, and H. H. Weitering, Phys. Rev. B. **73**, 193405 (2006).

[32] J. Frohn, M. Giesen, M. Poensgen, J. F. Wolf, and H. Ibach, Phys. Rev. Lett. **67**, 3543 (1991).

[33] M. Giesen, Prog. Surf. Sci. **68**, 1 (2001).

[34] E. Lundgren, B. Stanka, G. Leonardelli, M. Schmid, and P. Varga, Phys. Rev. Lett. **82**, 5068 (1999).

[35] E. Lundgren, B. Stanka, M. Schmid, and P. Varga, Phys. Rev. B. **62**, 2843 (2000).

[36] S. Fölsch, P. Hyldgaard, R. Koch, and K. H. Ploog, Phys. Rev. Lett. **92**, 056803 (2004).

[37] F. Nouvertné, U. May, M. Bamming, A. Rampe, U. Korte, G. Güntherodt, R. Pentcheva, and M. Scheffler, Phys. Rev. B. **60**, 14382 (1999).

[38] N. Knorr, M. A. Schneider, L. Diekhöner, P. Wahl, and K. Kern, Phys. Rev. Lett. **88**, 096804 (2002).

[39] J. A. Stroscio and R. J. Celotta, Science **306**, 242 (2004).

[40] H. C. Manoharan, C. P. Lutz, and D. M. Eigler, Nature **403**, 512 (2000).

[41] V. Repain, J. M. Berroir, S. Rousset, and J. Lecoeur, Surf. Sci. **447**, L152 (2000).

[42] M. B. Yilmaz and F. M. Zimmermann, Phys. Rev. E. **71**, 026127 (2005).

[43] M. D. Morse, Chem. Rev. **86**, 1049 (1986).

[44] H. Brune, G. S. Bales, J. Jacobsen, C. Boragno, and K. Kern, Phys. Rev. B. **60**, 5991 (1999).

[45] P. Gambardella, H. Brune, K. Kern, and V. I. Marchenko, Phys. Rev. B. **73**, 245425 (2006).

[46] C. Tao, T. J. Stasevich, T. L. Einstein, and E. D. Williams, Phys. Rev. B. **73**, 125436 (2006).

[47] N. Nilius, T. M. Wallis, and W. Ho, Science **297**, 1853 (2002).

[48] H. Weitering, Nature Phys. **7**, 744 (2011).

[49] C. Blumenstein, J. Schäfer, S. Mietke, S. Meyer, A. Dollinger, M. Lochner, X. Y. Cui, L. Patthey, R. Matzdorf, and R. Claessen, Nature Phys. **7**, 776 (2011).

[50] O. Gurlu, O. A. O. Adam, H. J. W. Zandvliet, and B. Poelsema, Appl. Phys. Lett. **83**, 4610 (2003).

[51] J. Wang, M. Li, and E. I. Altman, Phys. Rev. B **70**, 233312 (2004).

[52] J. N. Crain, A. Kirakosian, K. N. Altmann, C. Bromberger, S. C. Erwin, J. L. McChesney, J.-L. Lin, and F. J. Himpsel, Phys. Rev. Lett. **90**, 176805 (2003).

[53] J. R. Ahn, J. H. Byun, H. Koh, E. Rotenberg, S. D. Kevan, and H. W. Yeom, Phys. Rev. Lett. **93**, 106401 (2004).

[54] K. R. Simov, C. A. Nolph, and P. Reinke, J. Phys. Chem. C **116**, 1670 (2012).

[55] H. J. W. Zandvliet, A. Houselt, and B. Poelsema, J. Phys.: Condens. Matter **21**, 474207 (2009).

[56] N. Zaki, D. Potapenko, P. D. Johnson, and R. M. Osgood, Phys. Rev. B. **80**, 155419 (2009).

[57] See Supplemental Material.

[58] L. Gross, F. Mohn, P. Moll, N. Liljeroth, and G. Meyer, Science **325**, 1110 (2009).

[59] M. V. Rastei, B. Heinrich, L. Limot, P. A. Ignatiev, V. S. Stepanyuk, P. Bruno, and J. P. Bucher, Phys. Rev. Lett. **99**, 246102 (2007).

[60] C. Ataca, S. Cahangirov, E. Durgun, Y.-R. Jang, and S. Ciraci, Phys. Rev. B **77**, 214413 (2008).

[61] Š. Pick, P. A. Ignatiev, A. L. Klavsyuk, W. Hergert, V. S. Stepanyuk, and P. Bruno, J. Phys.: Condens. Matter **19**, 446001 (2007).

[62] Y. Mokrousov, G. Bihlmayer, S. Blügel, and S. Heinze, Phys. Rev. B **75**, 104413 (2007).

[63] W. Chen, T. Jamneala, V. Madhavan, and M. F. Crommie, Phys. Rev. B **60**, R8529 (1999).

[64] P. Wahl, P. Simon, L. Diekhöner, V. S. Stepanyuk, P. Bruno, M. A. Schneider, and K. Kern, Phys. Rev. Lett. **98**, 056601 (2007).

[65] P. Gambardella, A. Dallmeyer, K. Maiti, M. C. Malagoli, W. Eberhardt, K. Kern, and C. Carbone, Nature **416**, 301 (2002).

[66] S. Loth, S. Baumann, C. P. Lutz, D. M. Eigler, and A. J. Heinrich, Science **335**, 196 (2012).

[67] G. D. Mahan, Phys. Rev. Lett. **102**, 016801 (2009).

[68] A. I. Yanson, G. R. Bollinger, H. E. van den Brom, N. Agraït, and J. M. van Ruitenbeek, Nature **395**, 783 (1998).

[69] A. Thiess, Y. Mokrousov, S. Heinze, and S. Blügel, Phys. Rev. Lett. **103**, 217201 (2009).

[70] F. Tavazza, D. T. Smith, L. E. Levine, J. R. Pratt, and A. M. Chaka, Phys. Rev. Lett. **107**, 126802 (2011).

[71] I. Horcas, R. Fernandez, J. M. Gomez-Rodrguez, J. Colchero, J. Gomez-Herrero, and A. M. Baro, Rev. Sci. Inst. **78**, 013705 (2007).

[72] G. Kresse and J. Furthmüller, Phys. Rev. B **54**, 11169 (1996).

[73] G. Kresse and D. Joubert, Phys. Rev. B **59**, 1758 (1999).

[74] J. P. Perdew and Y. Wang, Phys. Rev. B **45**, 13244 (1992).

[75] J. P. Perdew, K. Burke, and M. Ernzerhof, Phys. Rev. Lett. **77**, 3865 (1996).

[76] P. T. Sprunger, L. Petersen, E. W. Plummer, E. Laegsgaard, and F. Besenbacher, Science **275**, 1764 (1997).

[77] C. Weiss, C. Wagner, C. Kleimann, M. Rohlfing, F. S. Tautz, and R. Temirov, Phys. Rev. Lett. **105**, 086103 (2010).

[78] H. J. Lee, W. Ho, and M. Persson, Phys. Rev. Lett. **92**, 186802 (2004).

[79] H. Ibach, *Physics of Surfaces and Interfaces* (Springer-Verlag, 2006).

[80] G. Kotliar, S. Y. Savrasov, K. Haule, V. S. Oudovenko, O. Parcollet, and C. Marianetti, Rev. Mod. Phys. **78**, 865 (2006).

[81] H. Park, A. J. Millis, and C. A. Marianetti, Phys. Rev. Lett. **109**, 156402 (2012).

[82] N. Zaki, C. A. Marianetti, D. P. Acharya, P. Zahl, P. Sutter, J. Okamoto, P. D. Johnson, A. J. Millis, and R. M. Osgood, http://arxiv.org/abs/1208.0612 .

[83] S. H. Vosko, L. Wilk, and M. Nusair, Can. J. Phys. **58**, 1200 (1980).

[84] V. I. Anisimov, F. Aryasetiawan, and A. I. Lichtenstein, J. Phys.: Condens. Matter **9**, 767 (1997).

[85] M. Wierzbowska, A. Delin, and E. Tosatti, Phys. Rev. B **72**, 035439 (2005).

[86] A. Mugarza and J. E. Ortega, J. Phys.: Condens. Matter **15**, S3281 (2003).

[87] T. Giamarchi, *Quantum Physics in One Dimension* (Clarendon Press, Oxford, 2004).

[88] F. Baumberger, M. Hengsberger, M. Muntwiler, M. Shi, J. Krempasky, L. Patthey, J. Osterwalder, and T. Greber, Phys. Rev. Lett. **92**, 196805 (2004).

[89] R. Eder and H. Winter, Phys. Rev. B. **70**, 085413 (2004).

[90] J. E. Ortega, S. Speller, A. R. Bachmann, A. Mascaraque, E. G. Michel, A. Närmann, A. Mugarza, A. Rubio, and F. J. Himpsel, Phys. Rev. Lett. **84**, 6110 (2000).

[91] J. E. Ortega, A. Mugarza, A. Närmann, A. Rubio, S. Speller, A. R. Bachmann, J. Lobo, E. G. Michel, and F. J. Himpsel, Surf. Sci. **482-485**, 764 (2001).

[92] J. Lobo, E. G. Michel, A. R. Bachmann, S. Speller, L. Roca, J. Kuntze, and J. E. Ortega, J. Vac. Sci. Technol. A **21**, 1194 (2003).

[93] G. Panaccione, I. Vobornik, J. Fuji, and et al, Rev. Sci. Inst. **80**, 043105 (2009).

[94] M. Giesen and T. L. Einstein, Surf. Sci. **449**, 191 (2000).

[95] F. Baumberger, T. Greber, and J. Osterwalder, Phys. Rev. B **64**, 195411 (2001).

[96] P. Thiry, D. Chandesris, J. Lecante, C. Guillot, R. Pinchaux, and Y. Pétroff, Phys. Rev. Lett. **43**, 82 (1979).

[97] J. E. Ortega, A. Mugarza, V. Repain, S. Rousset, V. Pérez-Dieste, and A. Mascaraque, Phys. Rev. B **65**, 165413 (2002).

[98] S. G. Louie, P. Thiry, R. Pinchaux, Y. Pétroff, D. Chandesris, and J. Lecante, Phys. Rev. Lett. **44**, 549 (1980).

[99] D. A. Papaconstantopoulos, *Handbook of the Band Structure of the Elemental Solids* (Plenum, New York, 1986).

[100] J. C. Slater and G. F. Koster, Phys. Rev. **94**, 1498 (1954).

[101] P. Heimann, H. Miosga, and H. Neddermeyer, Phys. Rev. Lett. **42**, 801 (1979).

[102] F. Baumberger, T. Greber, and J. Osterwalder, Phys. Rev. B **62**, 15431 (2000).

[103] F. Baumberger, M. Hengsberger, M. Muntwiler, M. Shi, J. Krempasky, L. Patthey, J. Osterwalder, and T. Greber, Phys. Rev. Lett. **92**, 016803 (2004).

[104] J. E. Ortega, M. Corso, Z. M. Abd-el-Fattah, E. A. Goiri, and F. Schiller, Phys. Rev. B **83**, 085411 (2011).